ACOUSTIC CHARACTERIZATION OF FLAME BLOWOUT PHENOMENON

A Dissertation
Presented to
The Academic Faculty

by

Suraj Nair

In Partial Fulfillment
of the Requirements for the Degree
Doctor of Philosophy in
Aerospace Engineering

Georgia Institute of Technology

May 2006

ACOUSTIC CHARACTERIZATION OF FLAME BLOWOUT PHENOMENON

Approved By:

Dr. Tim Lieuwen, Advisor
School of Aerospace Engineering
Georgia Institute of Technology

Dr. Marios C. Soteriou
Combustion Dynamics Group
United Technologies Research Center

Dr. Ben T. Zinn
School of Aerospace Engineering
Georgia Institute of Technology

Dr. Jeff Jagoda
School of Aerospace Engineering
Georgia Institute of Technology

Dr. Jerry Seitzman
School of Aerospace Engineering
Georgia Institute of Technology

Date Approved: 24 January 2006

To my parents

ACKNOWLEDGEMENTS

I would like to express my deepest gratitude to my advisor, Dr. Tim Lieuwen for his invaluable guidance and mentoring throughout this research work. I would also like to thank Dr. B.T. Zinn, Dr. Jerry Seitzman, Dr. Jeff Jagoda and Dr. Marios Soteriou for their many helpful comments and for taking an active part in my thesis committee.

I would like to thank the following in the Aerospace Combustion Lab for their help and discussions: Akbar, Akiva, Andy, Antonio, Arun, Ben, Bobby, Charles, Cliff, Colby, David, Dmitriy, Eugene, Gabe, Harry, Jason, Jayprakash, John, Joshua, Mael, Mohan, Moshe, Muruganandam, Nori, Preetham, Ping, Priya, Qingguo, Rajesh, Randy, Rob, Ryan, Sasha, Santosh S., Santosh H., Scott, Shai, Shashvat, Satish, Tom, Thao, Tudor, Venkat and Yedidia. I would also like to thank my friends: Faisal, Flo, Matthieu, Arnaud, Leon, Etienne, Augustin, Adam, Avik, Pierre, Amine, Rinda, Emily, Yogesh, Rajeev, Kapil, Tunga, Mudakar, Gopi and Satya for making my stay in Atlanta memorable.

I would like to acknowledge the following organizations for the support and funding of this work: National Science Foundation, South Carolina Institute for Energy Studies, GE Aircraft Engines, NASA Ames, Woodward and Department of Energy.

Finally, I would like to thank my family for their love and support, which encouraged me at every step in my life.

TABLE OF CONTENTS

LIST OF FIGURES

SUMMARY

This thesis describes an experimental investigation of blowout and its detection. The objective of this work was to characterize the blowout phenomenon and to develop a sensing methodology which can detect and assess the proximity of a combustor to blowout by monitoring its acoustic signature. The first part of the work examines the blowout phenomenon in a simple, atmospheric premixed piloted burner. As blowout was approached, the flame detached from one side of the burner and showed increased flame tip fluctuations close to blowout. Combustion noise was found to be dominant in the 10-150 Hz frequency regime of the acoustic spectra, which was associated to the amplified flame tip undulations.

The second part of the study focused on swirling combustion systems. Close to blowout, localized extinction/re-ignition events were observed. These events, manifested as bursts in the acoustic signal, increased in frequency and duration as the combustor approached blowout. An increase in 10-100 Hz frequency regime was observed in the combustion noise spectra which appeared to be controlled by the duration of and time interval between events. A variety of spectral, wavelet and thresholding based approaches were used to detect precursors to blowout.

The third part of the study focused on a bluff body burner. It characterized the underlying flame dynamics near blowout in greater detail and related it to the observed acoustic emissions. Vorticity was found to play a significant role in the flame dynamics. The flame passed through two distinct stages prior to blowout. The first was associated

with momentary strain levels that exceed the flame's extinction strain rate, leading to flame "holes". The second was due to large scale alteration of the fluid dynamics in the bluff body wake, leading to violent flapping of the flame front and even larger straining of the flame. This led to low frequency acoustic oscillations of the time scales of the von Karman vortex shedding. This manifested as an abrupt increase in combustion noise spectra at 40-100 Hz very close to blowout. Finally, work was also done to improve the robustness of lean blowout detection by developing integration techniques that combined data from acoustic and optical sensors.

CHAPTER 1

INTRODUCTION

1.1 Motivation

This thesis describes an experimental investigation of blowout and its detection. This problem has grown in prominence as development efforts are focused on reducing NO_x, CO and other pollutant emissions, and improving engine efficiency and reliability. This has resulted in advanced combustor designs that are critically dependent on effective fuel-air mixing and lean operation. However, such combustors have been found to be particularly susceptible to combustion instabilities and flame blowout.

Combustor blowout is a very serious concern in modern, highly loaded land-based combustors and particularly in aircraft engines where the combustion process is ultimately the source of the vehicle's thrust. When coupled with overall engine system dynamics, flame blowout can result in the inability of an engine to recover from a compressor stall event.[1] Rapid relight of the engine is required as its rotational speed decreases to its windmilling value. In addition, relight is difficult in high altitude vehicles where the stability limits are narrowed, which may necessitate their descent to lower altitudes. Blowout can be catastrophic for a tactical fighter aircraft engaged in aerial combat.[2] It is a particular concern in both military and commercial aircrafts during sudden changes in throttle setting. For example, during rapid decelerations, the fuel flow

rate can be reduced very quickly, while the slower air flow transient rate is controlled by the rotational inertia of the compressor.[3]

Blowout is also a major concern in land-based, industrial systems, where the engines are required to operate economically and reliably over long periods with minimal shutdown time.[4] Stringent emissions requirements have motivated these engines to operate premixed and fuel lean,[5] in order to minimize combustion temperatures and, therefore, NO_x. Such lean operation necessarily requires operating in the vicinity of the blowout point. If they occur, blowout events usually require a system shutdown and restart, which increases maintenance costs and reduces engine life and availability.

Currently, blowout is avoided by operating the combustor with a wide margin from the somewhat uncertain stability limit. Precise, real time knowledge of this margin would allow it to be reduced, resulting in lower pollutant emissions and enabling faster engine transients. The ability to sense blowout precursors can therefore provide significant payoffs in engine reliability and operability, in enabling optimal performance over extended time periods as an engine ages, in reducing maintenance costs and increasing engine life. This is the main motivation behind this study.

1.2 Background

In the last two decades, environmental restrictions have been implemented to reduce emissions from power generation and propulsive devices. A primary focus has been to reduce the nitrogen oxides (NOx) emissions. "NOx" refers to the sum of NO (nitric oxide) and NO_2 (nitrogen dioxide), which have long been identified as harmful atmospheric pollutants, contributing to acid rain production, photochemical smog and ozone depletion.[6-7] Burning of fossil fuels in power generation, transportation and

industrial burners has been shown to be a major source of NOx in the world. NOx is primarily produced during combustion by the oxidation of atmospheric nitrogen in the high temperature regions (above 1850 K) of the post-flame gases where there is enough energy to overcome the high activation energy of the formation reactions of NOx. The chemistry that details this NO formation[8] is given by the thermal or extended Zeldovich[9] mechanism:

$$O_2 + N \rightarrow NO + N \qquad (1)$$

$$N_2 + O \rightarrow NO + O \qquad (2)$$

$$N + OH \rightarrow NO + H \qquad (3)$$

Because of the harmful effects of NOx emissions, various government agencies have placed stringent restrictions on the operation of combustors in the industry. These restrictions are enforced through the Clean Air Act Amendments of 1970 (CAAA), which mandates continuous NOx monitoring[7] by federal, state, and/or local enforcement agencies. NOx emissions in early gas turbine combustors in land-based and aircraft engines were extremely high and showed no sign of decreasing until 1970.[6] These conventional gas turbine combustors operated in a diffusion (non-premixed) mode. In this type of flames, the fuel and air burn at stoichiometric ratios. Stoichiometric burning creates the highest combustion temperatures, and since NOx emissions increase exponentially with temperature,[10] diffusion combustors produce high levels of NOx (without water injection). Therefore, the engine manufacturers were compelled by emission regulations to make design changes.

The primary methods used to reduce NOx[11-12] are water injection, rich burn–quick quench–lean burn (RQL) combustion,[13] catalytic combustion, selective catalytic

reduction (SCR) and lean-premixed combustion. Water injection is expensive due to water treatment costs, increased maintenance from accelerated combustor corrosion and higher levels of CO and UHC emissions. RQL combustion was found to be susceptible to soot formation and incomplete mixing between fuel-rich combustion products and air. Catalytic combustion is not a viable option due to the short life of the catalysts at elevated temperatures and requires constant replenishment. SCR employs chemical addition (usually ammonia) in the post-turbine exhaust gas to convert the NOx into less-harmful compounds. A major drawback of SCR is the size and cost of the equipment. A viable option for producing ultra low NOx emissions for gas turbine engines is to operate the combustor in Lean Premixed (LP) or Lean Premixed Pre-vaporized (LPP) mode. The lean pre-mixed approach involves pre-mixing the air and fuel in proportions that make the mixture fuel lean ($\phi<1$), thus lowering the flame temperature and preventing the high energy environment needed for NOx formation. Of the above techniques, the one most widely implemented is lean premixed combustion (often with additional SCR clean up). However, at such low equivalence ratios, the operability range between the flashback and blowout regimes of such premixed combustors are much narrower compared to conventional (diffusion) combustors. Hence, while lean, premixed operation allows for reduction in NOx production, the overall stability of the combustion process is reduced. This is shown in Figure 1, which plots the parametric space over which sustained combustion occurs in combustors, often referred to as the region of "static stability" of the combustion process.

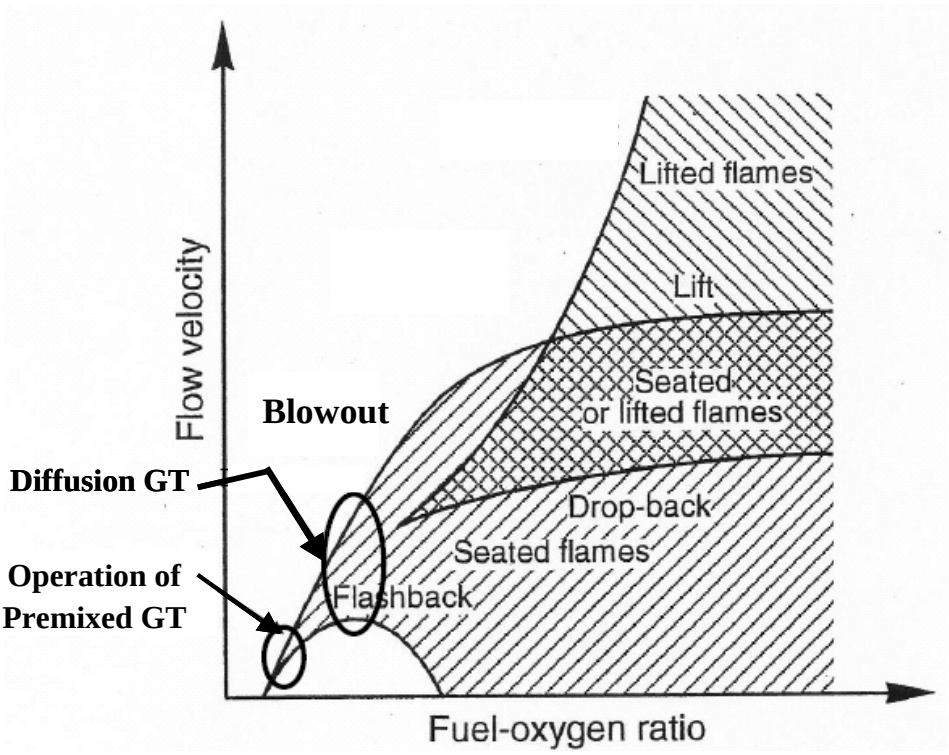

Figure 1: Stability map showing flame regions where sustainable combustion is possible in current (premixed) and conventional (diffusion) gas turbines.[14]

The term "static stability" is used to distinguish blowout from "dynamic stability", which usually refers to self-excited, combustion driven oscillations that involve chemical energy being fed into acoustic oscillations.[15-16] The loss of static stability leads to flashback or blowout. Blowout is especially prominent in lean premixed gas turbine engines because of the narrow stability limits. Under lean conditions, the combustion process is vulnerable to small perturbations in combustor conditions, particularly during load changes, or because of changes in fuel composition[17, 18] air temperature and humidity. At such conditions, the flame stabilization method used is not sufficient to sustain the flame inside the combustor, and the flame blows out. Therefore to prevent blowout, a comprehensive understanding of flame stabilization is required.

Since combustion must be initiated and sustained in highly turbulent streams flowing at speeds many times greater than the normal burning velocity, blowout is always a concern. This problem is surmounted by generating low velocity zones in the combustor where a flame can be stabilized, by imparting a high level of turbulence to the primary air jets for better mixing, and by allowing the hot combustion products to re-circulate and mix with the incoming fuel-air mixture, creating a continuous heat/radical feedback. A significant amount of early work was performed to understand the mechanisms of flame stabilization in high velocity streams.[19-23] These and other studies have reported the dependence of the characteristics of flames stabilized in bluff bodies,[13, 24-25] baffles,[20] swirling flows,[4, 26-30] dumps,[31] recessed ducts,[32] backward facing steps,[33] porous beds[34] and external pilots[22] and their dependence upon flow velocity, turbulence characteristics, flame holder geometry, swirl number, mixture temperature, composition, and pressure. Not surprisingly, because of the significantly different mechanisms by which heat and/or radicals are added to the unburned gases, it has been generally observed that the stabilization mechanisms of these various systems are different. For example, it has been suggested that the stabilization characteristics of bluff body stabilized flames are controlled by the ratio of a chemical time and the time that the unburned gases are in contact with the hot gases in the re-circulation zone.[35] Thus, the fluid mechanic stirring processes in the re-circulation zone play a critical role in these systems.

Most of the research efforts were focused on understanding the stabilization mechanisms and improving them, not on understanding the process of loss of stabilization. When a flame is near blowout, but statically stable, or an operating condition is changed such that the combustor moves from “stable” combustion to

blowout, several studies have observed that the combustion process exhibits enhanced unsteadiness. These observations are the primary basis for the work described in this thesis. For example, Nicholson and Field[36] observed large scale, irregular pulsations of a bluff body stabilized flame as it was blowing off. It should be emphasized that this unsteadiness was not observed "after the fact"; i.e., after the flame had blown off and was convecting out of the combustor. Rather, the flame was still observed behind the bluff body during these pulsations.

More recently, Chao *et al.*[37] have characterized a turbulent non-premixed jet flame during the blowout process. They reported that prior to blowout, the flame base pulsated from attachment to non-attachment at the burner lip. They found that this regime could persist over time intervals from a few pulsation cycles to several seconds. In addition, other work that will be reviewed in the next chapter have observed similar flame unsteadiness close to blowout.

Various theories[14, 24, 38] have been proposed to explain blowout in terms of chemical kinetics, flame stretch, flow convection, diffusion of reactants and instabilities. All these theories relate the thermal balance in the flame between heat release rate and the heat loss rate. The burning velocity, flame thickness and flow dynamics seem to be the most fundamental parameters that govern flame processes close to extinction. The focus of the existing literature on the subject is primarily devoted to predicting the blowout limits of a given system as a function of such parameters as equivalence ratio, air temperature, or pressure. Very little work has been done to characterize the combustion process as it transitions from static stability to blowout. The objective of the present work is to characterize flames under such circumstances, primarily through their acoustic emissions.

This objective is motivated by the desire to develop practical, fast diagnostic techniques that can be used to detect the onset of blowout.

Acoustic emissions provide a useful diagnostic into transient flame holding events because they are proportional to the temporal rate of change of heat release.[39] Furthermore, many ground-based systems are already instrumented with dynamic pressure transducers. As such, implementing the developed precursor detection technique simply requires inserting a software module into the existing monitoring software. Fundamentally, combustion noise is generated by the unsteady expansion of reacting gases. It has been shown in several studies that the acoustic emissions of turbulent flames are dominated by unsteady heat release processes[40-43] (as opposed to flow noise) that excite acoustic waves over a broad range of frequencies (typically between ~10 Hz – 25 kHz). Thus, acoustic measurements can be used to detect either global changes in heat release rate or fluctuations in heat release at certain time scales in a combustor by measuring its acoustic emissions in corresponding frequency bands.[44]

1.3 Overview of Present Work

The overall objective of this work is to characterize blowout phenomenon and develop a sensing methodology that can detect and assess the proximity of a combustor to blowout by monitoring the acoustic signature, thus providing early warning before the actual blowout of the combustor. Detection and prevention of blowout requires understanding of flame stabilization inside the combustor. A number of important physical parameters are expected to influence the flame characteristics in a combustor close to blowout, such as the acoustic field of the experimental setup, heat transfer between the reacting flow and its surroundings or the presence of shear layers and

coherent structures. Hence, it is essential to first understand the dynamics of a simple flame system, and to develop the techniques for experimental study and subsequent data analysis that would later be progressively applied to more complex combustors. With this view in mind, it was decided to first study an atmospheric, piloted, premixed natural gas fueled flame. The flame acoustics of this burner were comprehensively studied in anechoic environments, and the blowout diagnostic techniques developed during this study were later applied to swirl-stabilized, turbulent flames and bluff-body combustors. Next, the complexity of unmixedness generated due to liquid fuel injection was added to the problem. Finally, the effect of high combustor pressure was also studied in an effort to move closer towards simulating full-scale gas turbine conditions.

The outline of this thesis is as follows. The current and following chapter provide the background on blowout and flame stabilization upon which this thesis is founded. Chapter 3 details the different combustor configurations and provides background of various sensing strategies that are employed in the thesis. Chapter 4 presents the experimental results that characterize the near blowout acoustic emissions from a piloted burner and explain the blow-off phenomenology. Chapter 5 extends the analysis to swirling reacting flows and introduces three more burners; an atmospheric premixed swirl burner, a high-pressure swirl rig and a non-premixed swirl cup combustor. Then, Chapter 6 focuses on the bluff body flame and characterizes the underlying flame dynamics near blowout in detail that are ultimately responsible for its acoustic emissions close to blowout. Finally, Chapter 7 presents the conclusions of this research and recommendations for future work.

CHAPTER 2

REVIEW OF FLAME BLOWOUT

This chapter presents a literature review of flame blowout and introduces concepts that will be used in the rest of this investigation. It is divided into four sections. Section 2.1 provides the historical background of investigations in flame blowout. As most of the literature was primarily focused on jet diffusion flames, Section 2.2 reviews the various theories of flame blowout from jet flames. This section also compares the similarity of these blowout mechanisms to premixed flames. Section 2.3 reviews flame stabilization and extinction behind flameholders. Finally, Section 2.4 examines the flame blowout dynamics that were observed in various combustors in the literature.

2.1 Flame Blowout: A Historical Outlook

This section attempts to provide a historical perspective into research on combustor blowout. Documentation of the research on flammability limits extends back nearly a century, and the volume of available literature is quite large. Since the 1880's, work has been done to understand flame stabilization and propagation, in systems from simple Bunsen burners and gas stoves to industrial engines. One of the earliest detailed works on flame blowout was by Lewis and Von Elbe,[45] who attributed blowout to increased velocity gradients at the burner lip. Little emphasis was made on understanding blowout until the surge in interest in flame stabilization in ramjets and afterburners. During the early 1950's,

various researchers[21-24] proposed theories to explain blowout phenomenology from flameholders. These theories were later refined with advances in experimental techniques and computational power. The 1960's saw work in calculating wall quenching effects, flashback and blowout of propagating flames. Until the early 1970's, the problem of lean blowout was regarded as relatively minor. This was to a large extent due to the universal use of pressure-swirl spray atomizers in the industry, which had poor mixing characteristics, but had the advantage of allowing combustion below the flammability limits albeit with low combustion efficiency. In recent years, the trend towards improving fuel/air mixing in order to reduce pollutant emissions has led to narrowing of stability limits and has generated tremendous interest from industry in understanding lean blowout.[46]

2.2 Blowout from jet diffusion flames

To understand the basic mechanism of flame stabilization and blowout at a fundamental level, the problem of a diffusion flame formed by a fuel jet in an oxidizing atmosphere has been studied extensively[47-49] and stands out as a useful model system for studying stabilization in a simple geometry. Three distinct mechanisms have been proposed regarding the blowout of turbulent diffusion flames based on: 1) premixed flame propagation, 2) large scale mixing and 3) flame instability. Early investigators, such as Vanquickenborne et al.[50] (1966) and Kalghatgi[51] (1981), proposed expressions for blowout velocity based on premixed flame considerations, suggesting that blow-out occurs when the local reactant flow velocity exceeds the maximum premixed turbulent burning velocity. These predictions showed qualitative agreement with measurements for most hydrocarbon fuel mixtures. This classical theory is explained in greater detail below.

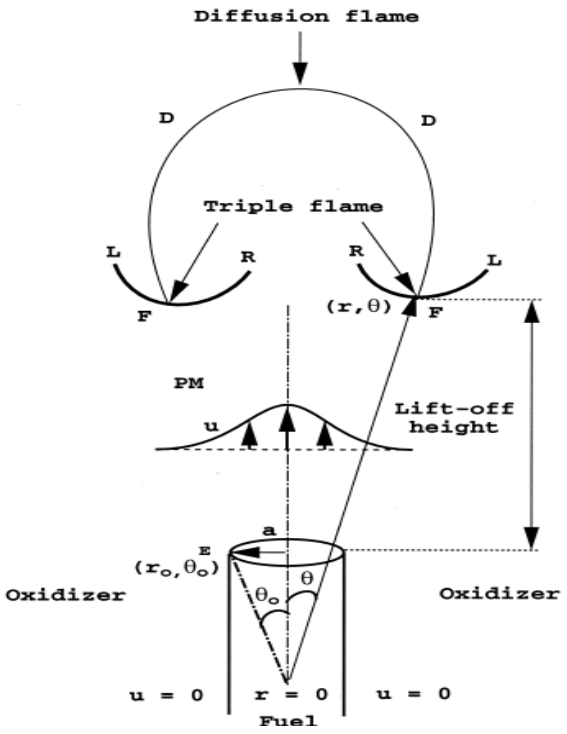

Figure 2: Schematic of the triple flame in a laminar lifted diffusion flame over a round jet (Vervisch et al.[52]).

In a laminar jet diffusion flame, if the mass flow rate exceeds a critical value, the base of the diffusion flame lifts off from the burner tip and remains suspended at a certain distance above the burner. This phenomenon is known as "lift-off" or "blow-off". A further increase in the mass flow rate of the jet causes the lift-off height to increase until the base of the diffusion flame approaches the flame tip at which point the flame blows out. If the flame extinguishes directly from the burner lip without a stable lifted position, the phenomenon is called "blowout". Hysteresis effects are seen, that is, flame lift-off and reattachment do not happen at the same value of the mass flow rate. However, blowout always occurs at a fixed mass flow rate for a given fuel in the burner. Near blowout

conditions, a complex time-dependent behavior is observed where the flame jumps back and forth between the lifted and attached configurations. This kind of flame detachment and re-attachment has also been observed in the present study in premixed flames.

The lifted diffusion flame is stabilized by a triple flame in the far field of the jet. Triple flames, first identified and observed by Phillips,[53] are a characteristic flame structure that appear in partially premixed flames, see Figure 2. The fuel and oxidizer undergo partial premixing in the zone 'PM'. The mixture then burns in two branches, the fuel rich branch, 'FR' and the fuel lean branch 'FL'. Behind these two flame zones the hot streams of unburnt fuel and oxidizer come together and burn as a trailing diffusion flame, 'DF' along the stoichiometric surface. The structure consisting of the three branches FR, FL and DF is collectively known as the triple flame. The triple flame has a characteristic propagation speed determined by the local environment. The flame is stabilized at the point where the flame propagation speed with respect to the fuel/oxidizer matches the flow speed on the stoichiometric line.

Broadwell et al.[54] (1994) suggest an alternate theory for explaining blowout based on Large Scale Mixing. They suggest that flame stabilization results when hot gases, which have been expelled to the edge of the jet by earlier large scale turbulent structures, are re-entrained and ignite non-combusting eddies within the jet. If the mixing time of the re-entrained gases is too short, the gases cool down rapidly and ignition becomes impossible, leading to blowout. Thus, blowout takes place when the reaction time cannot keep pace with the changes in mixing time. More recent experimental laser imaging by Muniz and Mungal[55] (1997) provides support for the role of the large-scale structures in the flame stabilization and extinction processes.

Recently, a flame-front instability model (Chao et al.,[37] 2000; Kim et al.,[56] 1996) has also been proposed to explain blowout, which states that intrinsic flame-front instability causes pulsations and plays a role in leading to the blowout. Chen and Goss[57] (1989) reported that the critical limit for liftoff of jet diffusion flames appeared to be independent of the velocity but more dependent on the strain rate near the stabilization zone. They also observed violent flame base fluctuations close to blowout.

To conclude, although premixed flame concepts can explain most aspects of blowout in diffusion flames, recent works suggest that coherent structures, high strain rates, heat losses and entrainment play an important role in the loss of flame stabilization.

2.3 Blowout from bluff bodies

Bluff bodies are used to stabilize flames in high velocity flows in a variety of propulsion and industrial combustion systems. They are employed for supplementary firing in industrial boilers and heat recovery steam generators, and are also used in ramjet and turbojet afterburner systems (see Figure 3). In addition, they are often used in fundamental studies of turbulent flame characteristics[58] or as computational test cases,[59, 60] and have been targeted as one of three stationary laboratory premixed flame configurations for study by International Workshop on Premixed Flames participants.[61]

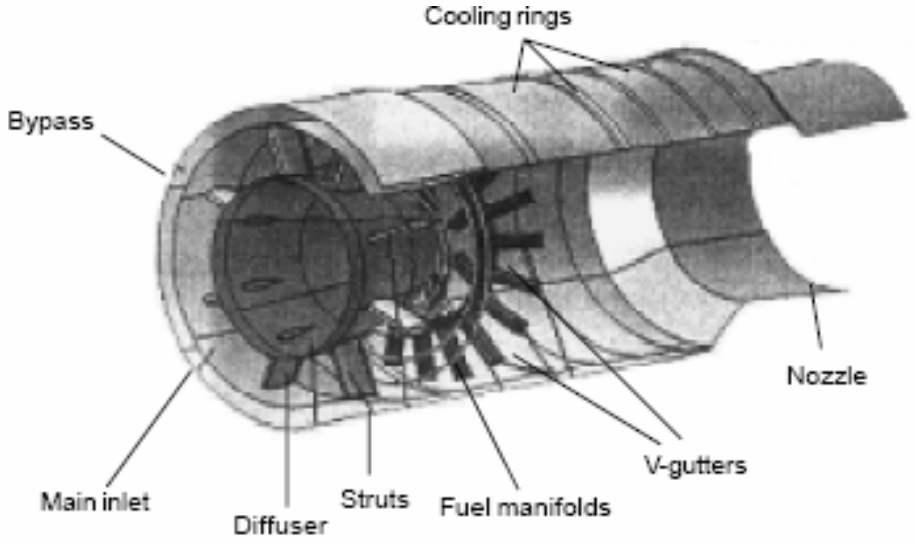

Figure 3: Illustration of a typical afterburner assembly.[62]

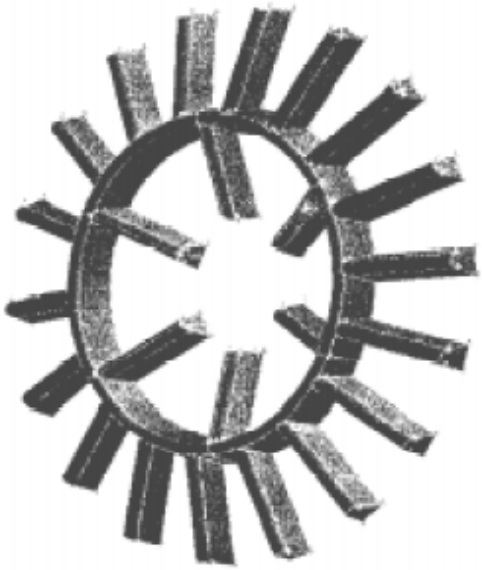

Figure 4: Radial and ring V-gutter flame holder arrangement used in afterburner systems.[62]

The usual bluff bodies used are cylindrical rods, rectangular bars, discs, baffles, cones or "vee" gutters (see Figure 4), which produce in their wake a low velocity re-circulatory flow in which combustion can be initiated and maintained. The propagation of the flame to other regions is rendered possible by the transport of heat and radicals from the boundaries of the re-circulation zone to the adjacent fresh mixture.

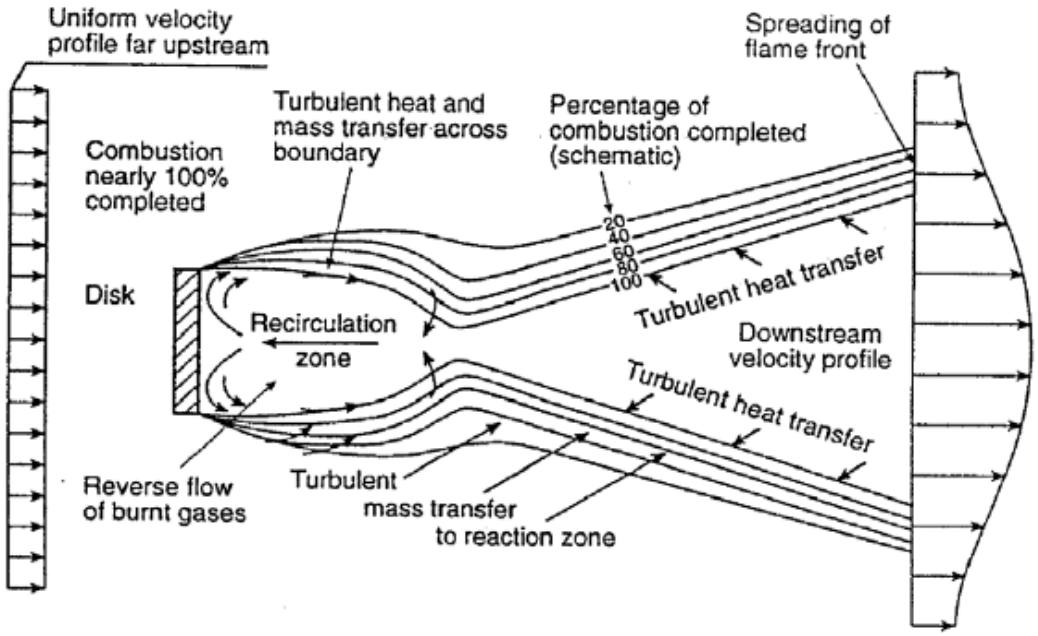

Figure 5: Flame stabilization zone behind a bluff body (Williams,[63] 1966).

Much of our present understanding of the flame stabilization process is due to the pioneering studies carried out in the 1950's by Zukowski,[35] Cheng and Kovitz,[24] Longwell,[20] Shipman[22] and Williams.[23] These studies found that the wake behind the bluff body can be divided into the re-circulation zone and the mixing zone that keeps the re-circulation zone away from the unburned reactants as seen in Figure 5. The mixing

zone, characterized by turbulent shear layers with large temperature gradients and vigorous chemical reaction, is fed by turbulent mixing (of heat and mass) processes with cool combustible gas from the approach stream (based on the mixing model by Williams[63]).

Various theories of flame stabilization have been proposed, which differed in the formulation of blowoff criterion either based upon energy balance (Williams et al.,[21] 1949; Khitrin and Goldenberg,[64] 1955), mass balance (Longwell et al.,[20] 1951; Bovina,[65] 1958; Ballal and Lefebvre,[46] 1979), purely kinetic considerations (Zukoski and Marble,[35] 1956) or on mixing models (Williams and Shipman,[23] 1953; Cheng and Kovitz,[24] 1958). Some of the theories will be briefly explained.

According to Zukoski[35](1956), ignition of the fresh mixture occurs in the shear layer when it is mixed with combustion products from the re-circulation zone. The burning mixture flows downstream through the shear layer and ignites the neighboring mixture kernels. When it reaches the end of the wake, some of the burning mixture continues downstream while the remainder is entrained into the re-circulatory flow, which conveys it back upstream to mix with and ignite the shear layer. The flame remains anchored as long as this feedback process continues. Flame extinction occurs when the fresh mixture does not spend enough time in the shear layer to be ignited by the hot re-circulation zone. Thus, the criterion for blowout is that the ignition delay time be equal to the residence time in the shear layer. For blowout, a "critical ignition delay time" can be defined which is roughly the time of contact between the cool combustible mixture and hot wake:

$$t_{BO.} = D_r / V_{BO} \qquad (4);$$

where D_r is the length of the recirculation zone (which was found to be a function of equivalence ratio) and V_{BO} is the blowout velocity.

Longwell et al.[20](1951) viewed the wake of a bluff body essentially as a homogeneous well stirred reactor and blowout occurred when the time available for chemical reaction became less than the time required to generate sufficient heat to raise the mixture to its ignition temperature. However, perfect homogeneity rarely exists in practical combustors and therefore the mass-transfer WSR model was inadequate in explaining blowout. Cheng and Kovitz[24] (1958) proposed a theory of bluff body flame stabilization based on mixing between the burnt and unburnt gases in the re-circulation zone. The consensus of all these early studies was that flame blowout limits could be well predicted and the blowout phenomenology was influenced by interactions of fluid mechanics and chemistry.

Considering that fluid mechanics plays an important role in flame stabilization, it is important to examine the cold flow field behind a bluff body. Figure 6 illustrates the different flow regimes past a non-reacting flameholder. At very low Re_D, there is no flow separation. As Re_D is increased, there is flow separation and eddies start to form. The eddies grow bigger and become unstable and are shed alternately for Re_D>40. A clockwise rotating eddy or vortex is 'shed' from the top side, followed by an anticlockwise rotating eddy from the bottom side, leading to a staggered array of alternating vortices, also known as the von Karman vortex street. This is a periodic phenomenon[66] that occurs at a well-defined frequency; e.g., for circular bodies at Re_D>400; it occurs at a Strouhal number, St=fD/U=0.21, where D and U denote the diameter and axial flow velocity respectively. Further increase in Re_D leads to transition

and turbulent flow. For the purpose of this study, the combustor flow regime will be in the range $300<Re_D<10^5$, where the vortex street is fully turbulent. The non-reacting flow past a bluff-body is mainly dominated by the vortex shedding phenomenon. This phenomenon is so ubiquitous in flow behind bodies that it can be seen over a large range of length scales ranging from flow around a circular rod measuring about a centimeter, to terrestrial phenomena such as flow past islands, with typical length scales of the order of a few hundred kilometers, as shown in Figure 7.

There is much uncertainty in the literature, however, on the flow field characteristics in the presence of combustion. For example, the topic of whether vortex shedding even occurs at all has been discussed extensively in various experimental and computational studies.[67-69] Hertzberg et al.[25] described velocity measurements in a bluff body wake, and concluded that vortex shedding did not occur in the flow, except for situations near blowout. This conclusion appears to have been based upon the presence or absence of well-defined peaks in the velocity spectra.

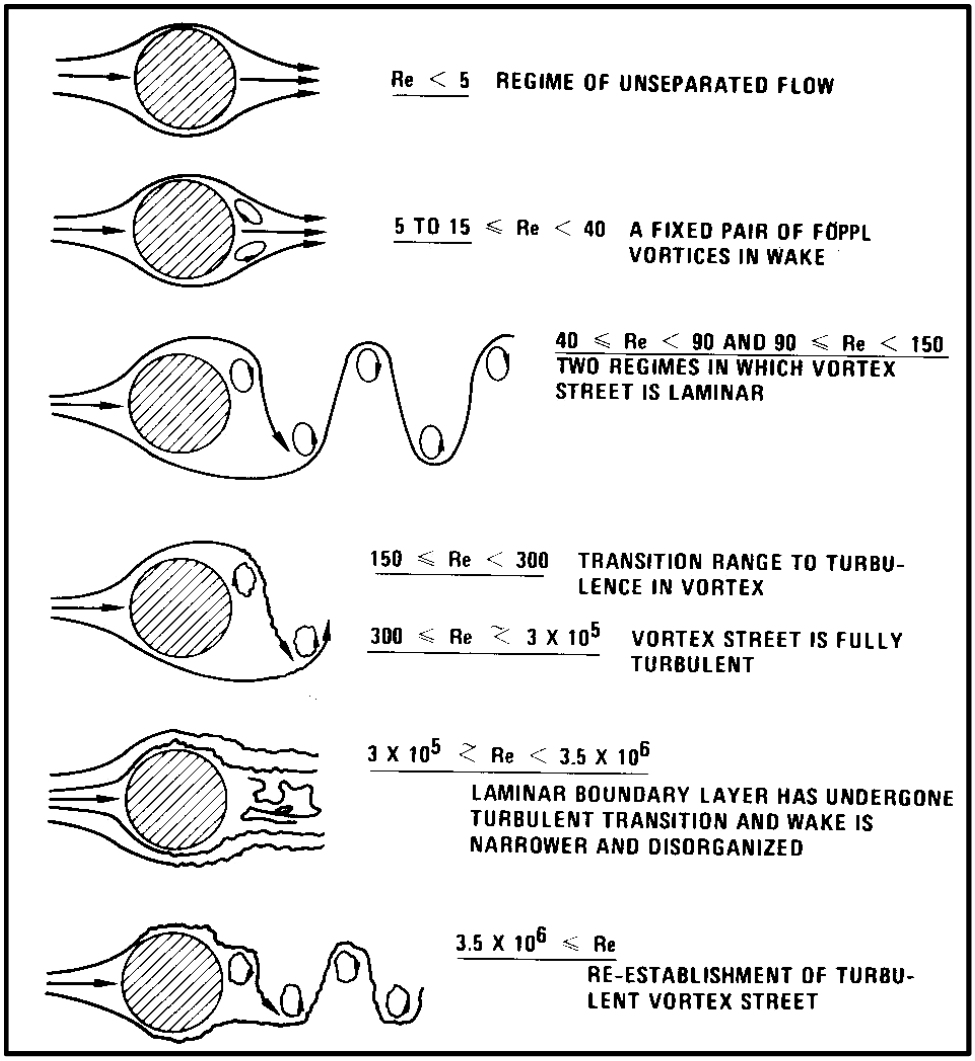

Figure 6: Non-reacting flow[70] behind a cylinder as a function of Reynolds number.

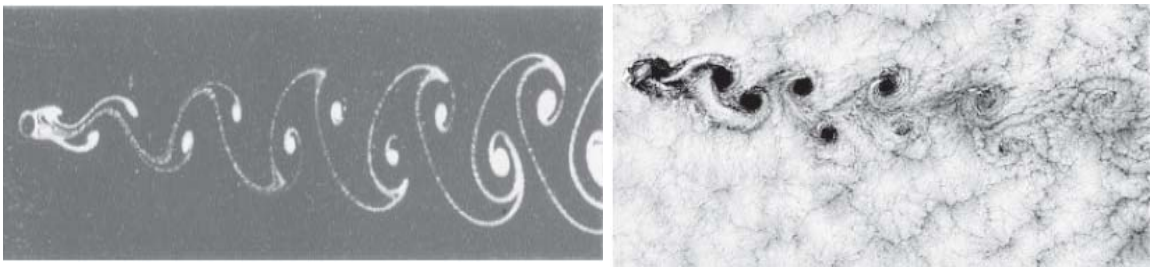

Figure 7: Von Karman vortex shedding observed behind a cylinder (left); NASA satellite picture taken by the satellite Landsat 7 of the clouds around Alexander Selkirk Island in the southern Pacific Ocean[71] (right).

The presence of combustion changes the dynamics of the wake in a manner that leads to a shift from a Von Karman, single frequency dominated, asymmetric solution in the non-reacting case to a far less periodic solution that is not characterized by a well defined shedding frequency. Understanding this shift is important in determining the dynamic processes of a flame close to blowout. The effect of exothermic reactions introduces three significant physical processes upon the flow field beyond that present in the non-reacting flow. These can be understood from the vorticity transport equation:

$$\frac{D\vec{\omega}}{Dt} = \underbrace{(\vec{\omega}.\nabla)\vec{V}}_{\text{Vortex Stretching/ Bending}} - \underbrace{\vec{\omega}\nabla.\vec{V}}_{\text{Gas Expansion}} + \underbrace{\frac{1}{\rho^2}\nabla\rho\times\nabla p}_{\text{Baroclinic Production}} + \underbrace{\nu\nabla^2\vec{\omega}}_{\text{Diffusion}} \quad (5);$$

(I) (II) (III) (IV)

where ω, u, ρ, p, and ν denotes vorticity, gas velocity, density, pressure, and kinematic viscosity. First, the kinematic gas viscosity (term IV above) sharply rises through the flame, due to its large temperature sensitivity. This will tend to enhance the rate of diffusion and damping of vorticity, an effect emphasized by Coats. [69] Second, due to the inclination of the flame with respect to the flow (and, therefore, the pressure gradient), vorticity is generated by the baroclinic mechanism [72] (term III above), due to the misaligned pressure and density gradients. Third, there is generally significant gas expansion behind the flame (term II above). The flow dilatation acts as a vorticity sink, as can be seen by the negative sign of this term in the vorticity transport equation above.

It should be noted that there is competition between baroclinic and bluff body generated vorticity – these two sources are of the opposite sign. The flow near and far from the bluff body is dominated by bluff body and baroclinic generated vorticity, respectively. This was seen in the computational studies by Soteriou et al.[68] This

competition results in complete cancellation, and then sign reversal, of flow vorticity with downstream distance. This point has important implications upon the flame's blowoff dynamics.

Leonard et al.[73] (1991) performed LES (Large Eddy Simulations) to understand blowout of a premixed flame stabilized behind a flat plate in a duct. The LES of the isothermal (cold) flow field captured vortices shed from the corners of the plate at a fixed frequency, which agreed with the literature data discussed above. The reacting flows were also studied using LES and a global one-step combustion model. Combustion caused the flow pattern behind the flameholder to become steady for equivalence ratios close to unity. As the equivalence ratio was reduced to near blowout, the vortex shedding reappeared. This is in agreement with the findings of Hertzberg et al.[25] Further reduction in equivalence ratio resulted in vortical structures pinching off the re-circulating product gases, thus causing blowout of the flame.

Bill and Tarabanis[74] (1986) suggested that a well-stabilized flame suppresses vortex shedding by preventing entrainment from outside the wake perhaps due to increased dissipation and flame generated acceleration. These effects become less pronounced as the equivalence ratio is brought down to blowoff. They also observed increased vortex shedding closer to blowout.

2.4 Flame Dynamics prior to blowout

The primary basis for the work described in this thesis is that a flame, as it approaches blowout from a statically stable operating condition, exhibits enhanced unsteadiness. Often, temporary flame losses and re-ignitions are also seen close to blowout. These result in global and local changes in heat release rates in the combustion

zone, producing corresponding changes in acoustic, chemiluminescence and ion emissions, in addition to the change in flame temperatures. These emissions can be detected by readily available sensors and can be used to characterize the blowout process in a combustor. Numerous researchers have found such unsteady flame dynamics in combustors prior to blowout. This section will briefly review some of them.

Nicholson and Field (1951)[36] was one of the first to observe large scale pulsations in a bluff body flame as it was blowing off. They also reported that the main flame detached and reattached to the flame holder repeatedly before extinguishing completely. Bill and Tarabanis[74] (1986) and Hertzberg, Shepherd and Talbot[25] (1991) found increased vortex shedding from bluff body flames close to blowout. Hertzberg et al.[25] claimed that blowout was a result of increased ignition times, longer re-circulation zones and local extinction resulting from high instantaneous strain rates.

Roquemore et al. (1991)[75] observed longitudinal oscillations in a non-premixed, gas turbine combustor simulator just prior to blowout. They found the flame to lift off from the base of the combustor as equivalence was reduced to near blowout values. This was one of the earliest flame dynamics observed in a realistic engine. Santavicca et al.[76] (1999) conducted a parametric study to investigate combustion stability in a coaxial, premixed bluff-body-stabilized dump combustor. Using CH* chemiluminescence images, they were able to capture repeated detaching and reattaching of the flame from the centerbody close to blowout. De Zilwa et al.[77] (2000) similarly investigated flame dynamics close to blowout in dump stabilized combustors with and without swirl. They noticed very low frequency (around 3-12 Hz) oscillations as the blowout was approached. Chao et al.[37] (2000) used acoustic excitation to stabilize a jet flame beyond its stability limit and then

suddenly turned off the excitation to understand the blowout process by itself. They found that the flame base pulsated from attachment to non-attachment at the burner lip prior to blowout. They found that this regime could persist over time intervals from a few pulsation cycles to several seconds. They suggest that high strain rates, much higher than the extinction strain rates, encountered by the flame base should be a prominent factor in the blowout process. This will be explained in a greater detail in Chapter 6.

Hedman et al.[78] (2002) investigated blowout in a swirl-dump stabilized combustor using OH PLIF. They observed intense flame oscillations and temporary loss of flame near the lean blowout limit. Similar behavior is seen in this study and is explained in Chapter5. CFD studies by Norton[79] (2003) in micro-burners also observe periodic oscillations near extinction, caused due to high heat loss and the presence of large transverse and axial velocity gradients. More recently, Chen et al.[80] (2004) found pulsating flame modes in their study of laminar non-premixed flames near heat loss and blowout limits. They investigated the effect of Lewis number (Le) on the pulsating instability of near-blowout C_3H_8, CH_4 and H_2 flames. Their results show that large values of Le are necessary for pulsating instability to occur in near blowout flames.

CHAPTER 3

INSTRUMENTATION AND DATA ANALYSIS

This chapter describes the various experimental facilities, instrumentation, sensing methodologies and data analysis schemes that were employed in this study. The first section explains the experimental set-ups, the operating conditions and salient features of the different combustors employed in this investigation. The second section primarily deals with the sensors used in this study. The last section describes the procedures for acquisition, processing and data analysis.

3.1 Experimental Systems

This study employed burners with the three fundamentally different flame holding mechanisms: pilot flame, swirl and bluff body. Most of the studies employed premixed combustion systems, but limited data were also obtained in a non-premixed swirl combustor.

3.1.1 Piloted Burner

A schematic of the piloted, natural gas fueled, 50 KW burner used in this study is shown in Figure 8. The burner tube is 110 mm long and was sized to ensure fully developed pipe flow at its exit. The main burner consists of a 23mm stainless steel tube

and is surrounded by a circumferential array of 24mm x 1.6mm diameter pilot holes. The fuel and air flow rates into the main and pilot burner were controlled separately. The pilot flame anchors the main flame at high flow velocities. The flow control and monitoring system have a resolution of approximately 0.01 in equivalence ratio (ϕ). All measurements were made at atmospheric conditions.

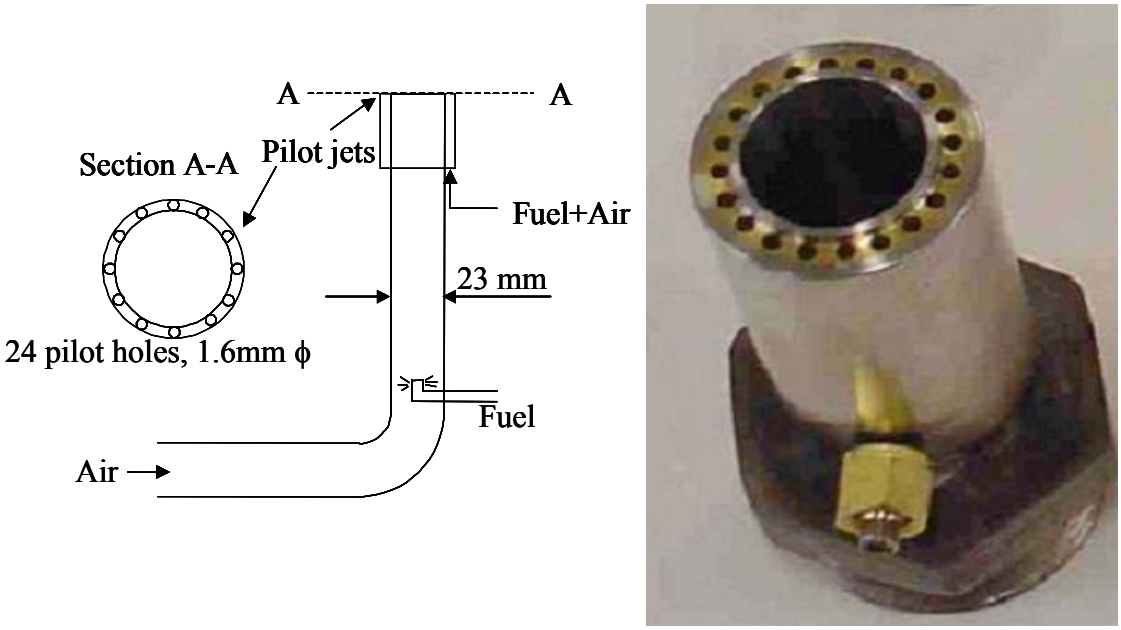

Figure 8: Schematic and photograph of the 50 KW ring-piloted burner.

3.1.2 Premixed Atmospheric Swirl Combustor

A schematic of the 100 KW, swirl-stabilized combustor is shown in Figure 9. A premixed methane-air mixture passes through swirl vanes housed in a 23 mm i.d. tube. The exit of the jet has a swirler with vane angle of 30^o, which is equivalent to a swirl number[30] (calculated as equal to 2/3 tan (30^o)) of approximately 0.39. The flow expands

into a cylindrical 70 mm diameter and 127 mm long combustion chamber. The combustor walls are made of quartz to facilitate flame visualization and chemiluminescence measurements. The flow control and monitoring system have a resolution of approximately 0.003 in equivalence ratio (ϕ). All measurements were made at atmospheric conditions. The wall temperature was measured with a thermocouple.

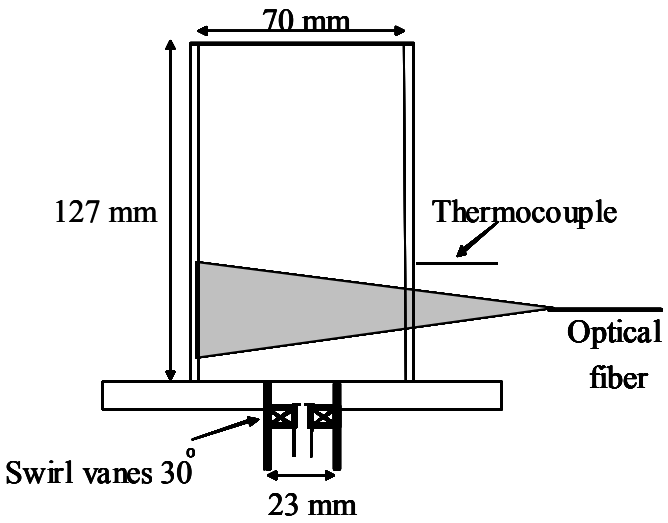

Figure 9: Schematic of the 100KW swirl combustor.

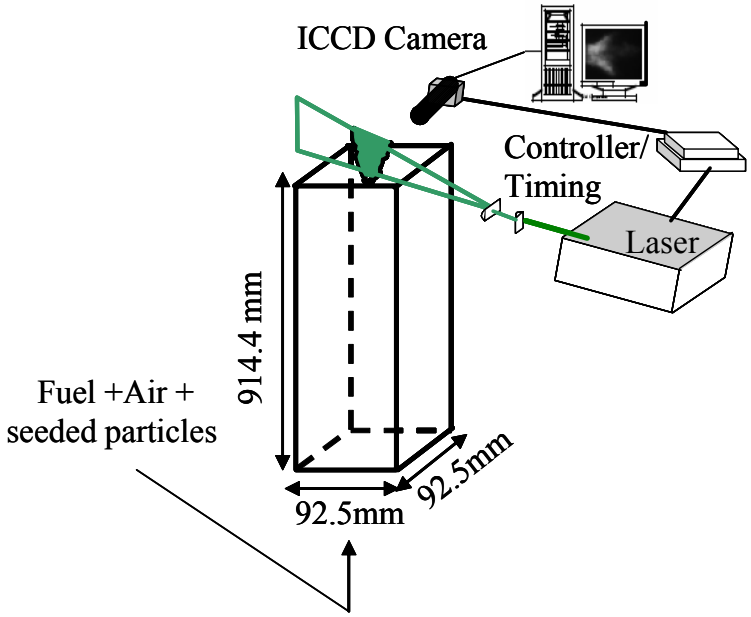

Figure 10: Schematic of the bluff body burner setup.

3.1.3 Bluff body burner

Experiments were carried out with a 9.5 mm cylindrical bluff body, mounted at the immediate exit of a square section channel (95.25 mm x 95.25 mm x 914.4 mm) to stabilize the flame, shown in Figure 10. The fuel (natural gas) and air are mixed in a plenum chamber. It then passes through a flashback arrestor, a series of settling screens and flow straighteners and finally exhausts into the ambient environment at the burner exit. The flow control and monitoring system have a resolution of approximately 0.04 in equivalence ratio. All measurements were made at atmospheric conditions.

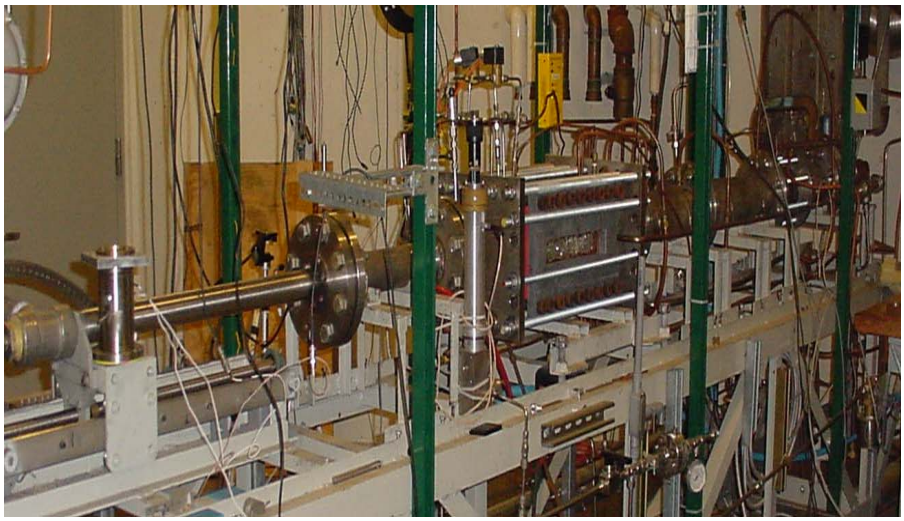

Figure 11: Photograph of lean, premixed combustor facility.

3.1.4 High pressure swirl combustor

Measurements were obtained in a lean, premixed gas turbine combustor simulator, shown in Figure 11. High-pressure 720 and 1000 psig natural gas and preheated air are supplied from building facilities. The air and fuel flow rates are measured with a critical orifice and mass flow controllers respectively. The uncertainty in the flow rate measurements is 2% of full scale. In order to ensure that acoustic oscillations do not affect the fuel/air mixing processes, the fuel and air are mixed upstream of a second choke point. Thus, the equivalence ratio of the reactive mixture entering the flame is constant. The temperature of the reactants was measured with a thermocouple located just upstream of the swirler.

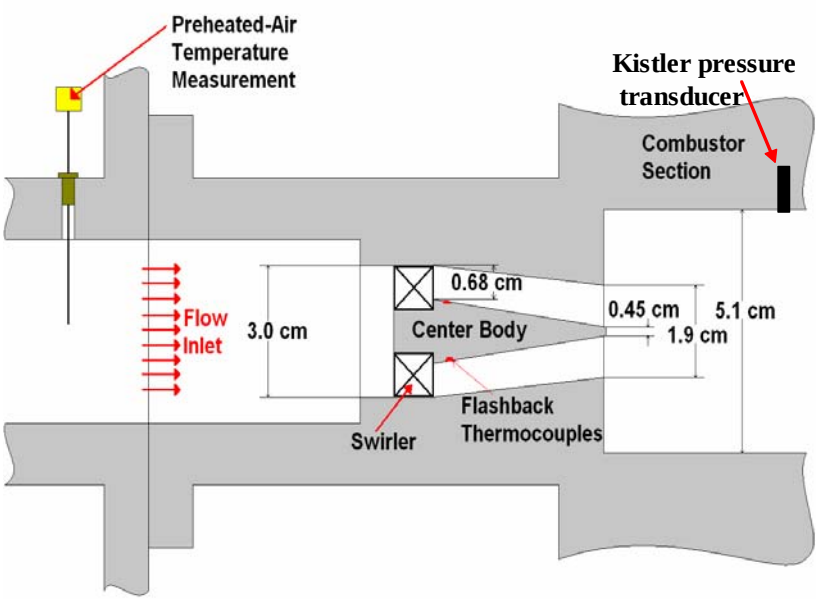

Figure 12: Cross section of inlet section of the high pressure combustor.

The fuel-air mixture enters the circular 4.75 cm diameter, 60 cm long inlet section and then passes through a single 12 vane, 35^{o} swirler, prior to entering the 5x5 cm square combustor, see. The square part of the combustor is 51 cm long and is optically accessible. It then transitions into a circular 7.6 cm diameter, 195 cm long exhaust section. The exhaust sections are water-cooled[i]. The flow leaves the setup through an exhaust nozzle with an adjustable bypass valve.

3.1.5 Non-premixed Swirl Combustor

Experiments were performed on an atmospheric pressure, single swirl cup CFM-56 injector, illustrated in Figure 13, which is a part of a commercial flight engine used on a variety of Boeing and Airbus platforms. Only the front end of the combustor was retained. The remainder of the combustor was built around this hardware to facilitate

[i] Note that the combustor top and bottom walls are water-cooled and side-walls are air-cooled.

diagnostics. The test-section sidewalls are made of quartz glass. The top and bottom walls consist of thermal-barrier coated (TBC) metal plates that were machined out in an arc to simulate the annular shape of the actual hardware. In the same way, the windows are set in at angles, so that the resulting chamber mimics a single nozzle in an annular combustor.

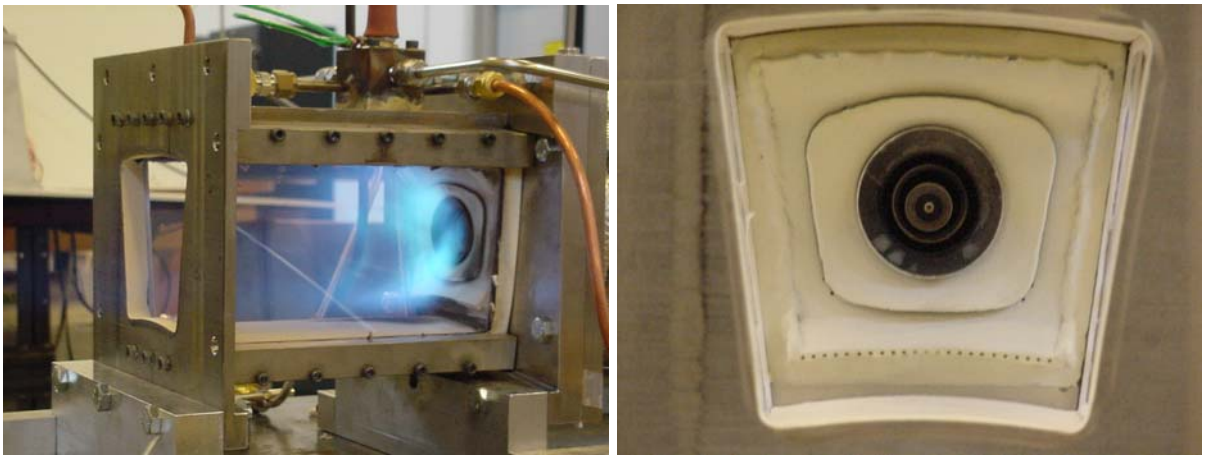

Figure 13: Photograph (side-view and front-view) of the swirl cup combustor.

Non-vitiated, preheated air is supplied to the swirl cup from plenum chamber. Air enters the combustor through counter-rotating swirlers, while the fuel is injected through a centrally located fuel nozzle. This is followed by a small annular passage leading to the test section. Because the fuel flow rates are substantially lower than in the actual engine (about $1/30^{th}$ at full power), the standard fuel nozzle was replaced with a pressure-swirl atomizer. Aviation grade, Jet A fuel, essentially a kerosene-based fuel with additional corrosive inhibitors, was used for all tests.

3.2 Instrumentation

3.2.1 Acoustic and Pressure Measurements

Acoustic oscillations were measured with calibrated, Brüel & Kjaer type 4191, 13mm and type 4939, 6.5mm condenser microphones that have a flat frequency response up to 40 kHz and 100 kHz respectively. These sensors had a sensitivity of 13mV/Pa and 4mV/Pa respectively. These microphones employ a stainless steel diaphragm and a protective grid, but are inoperable beyond temperatures of 450K. High temperatures up to 2000K and highly corrosive exhaust gases disallow the flush mounting of standard microphones to combustor walls. Therefore, the microphones were typically located in the acoustic far field, ~60 cm from the combustor exit at ~0^o to 30^o from the flow axis of the combustors.

Pressure oscillations inside the high-pressure combustor rig were measured with piezoelectric Model 211B5 Kistler pressure transducers and were flush mounted and water-cooled, as shown in Figure 12. These sensors employ quartz crystals and use the phenomenon of piezoelectricity — the tendency of some materials to produce a voltage when subjected to pressure — to convert sound vibrations into an electrical signal. These have a wide frequency response up to 50 kHz but have lower sensitivity (0.007mV/Pa) than the condenser microphones. These are more rugged sensors with higher shock resistance. The signal and DC excitation power to the sensor is provided through a power supply/coupler.

Cable noise is minimized by using sheathed cables. The sensors were calibrated at 200 Hz with a Model 4228 Brüel & Kjaer microphone calibrator.

3.2.2 Chemiluminescence Measurements

The imaging region for the chemiluminescence collection optics setup in the atmospheric swirl combustor is indicated in Figure 9. The optical collection setup employs a 365μm diameter fused silica optical fiber. The fiber has an acceptance cone half angle of about 12^{o}. The collected radiation is passed through an interference filter, centered at 309 nm, (full-width-half-maximum, FWHM of 10 nm) which corresponds to the OH $A^2\Sigma$-$X^2\Pi$ electronic transition. Fused silica was a preferred material for the fiber-optic cable because this material ensured high transmission (more than 98 %) of incident ultraviolet light (around 309 nm). The collected OH emission is detected by a miniature, metal package PMT (Hamamatsu H5784-04), which converts the incident light flux into a linearly proportional current. This PMT has a built-in amplifier (bandwidth of 20 kHz) to convert the current to voltage and operates from a 12V DC source. In addition, a neutral density (ND) filter with optical density of 1.0 was used to reduce the intensity of light collected and prevent saturation of the chemiluminescence signal.

Chemiluminescence is the radiation from electronically excited molecules, which emit light when they relax to lower energy states. Since the intensity of emission is proportional to the chemical production rate of the particular molecule, the chemiluminescence intensity can be related to chemical reaction rates. [81] Chemiluminescence has been used in previous works[82-86] as a measure of reaction rate and heat release rate. Chemiluminescence is appropriate for monitoring the flame stability and blowout since it can provide information on the presence and strength of the combustion process in a specific region of the combustor. The primary chemiluminescing species of interest in a hydrocarbon flame are electronically excited OH (around 309nm),

CH (around 430 nm) and C_2 (around 519 nm) radicals and the CO_2 molecule (broadband visible). In lean hydrocarbon flames, OH tends to be the strong emitter, followed by CH with little C_2 emission.[87-89] In this study, only OH* chemiluminescence was measured.

3.2.3 Velocity Measurements

Dantec 55P11 constant-temperature anemometer (CTA), 1-D hot wire probes were used to measure the cold flow velocities of the pilot jets in the piloted burner. The Dantec hot wire probes have a frequency response of up to 100 kHz. Their operating temperatures are limited to 330K and they are, therefore, not suitable for measurements in the flame.

Particle Image Velocimetry (PIV), a quantitative flow visualization technique, was used to determine the instantaneous whole-field fluid velocities[90] in selected cases. These velocities were obtained by recording and processing multiply-exposed particle image pattern of small traces suspended in the fluid. The air entering the bluff body burner was seeded with 2-3 μm aluminum oxide particles, which were illuminated using a laser light sheet produced from the second harmonic output (532 nm) of a dual-head, pulsed Nd:YAG laser. Each laser head is capable of providing 150 mJ/pulse at the rate of 10 Hz. The beam was converted into a thin sheet with two cylindrical lenses. The sheet passes through the midpoint of the flameholder. The illuminated particles in the combustor were imaged using a 12-bit MicroMAX Interline CCD camera (Roper-Scientific, 1300×1030 pixels) equipped with a 50 mm Nikkor lens (f 1/1.8). The laser arrangement used in the PIV measurements is also shown in the schematic in Figure 10.

The particle displacements are obtained by dividing the PIV image (1030 x 1300 pixels) into smaller interrogation windows (usually ranging from 16 × 16 to 64 × 64

pixels), for which a single velocity vector is computed for each window. The displacement is determined by computing the spatial cross-correlation function for the corresponding windows in each image of the pair. For this study, the interrogation window size was 32 × 32 pixels, with a 50% overlap, which resulted in 31 × 39 vectors across the field. The delay between the laser pulses, 100 μs, was chosen such that 25% of the seeded particles remained in the interrogation window between two consecutive PIV images. An error analysis of the PIV imaging experiments is presented in Appendix A.

3.2.4 Flame Imaging

A high-speed intensified CCD camera (Kodak Ektapro 239×192 full frame resolution) was used with a UV Nikkor camera lens to image flames stabilized in the piloted and swirl burners. Images were typically captured with an intensifier gating time of 200 μs at 1000 frames/second. The camera, which is sensitive to radiation in the UV and visible, was operated without any spectral filtering.

The temporal dynamics of the bluff body stabilized flame sheet were visualized by laser sheet scattering from olive oil (3-5 μm) seeded into the inlet air mixture. The oil droplets were generated using a Laskin nozzle design, with the nozzle immersed in the oil. The light sheet originates from an 8W Coherent Innova 90C continuous Argon-Ion laser of wavelength 514.3 nm. A cylindrical lens was used to provide a 4mm thick light sheet that passes through the flame at the bluff body midpoint. At each operating condition, 8000 images were obtained without any spectral filtering at 1000 frames/second with an exposure time of 100 μs. The field of view is 89mm x 89mm, imaged at a resolution of 512 pixels horizontally and vertically. The images were captured by a high-speed intensified camera (Videoscope International, Ultracam3). The

GEN III image intensifier in the camera has a response from 200 to 700 nm with a gate duration as short as 50 ns. The images, once captured, were then analyzed by tracking the high gradient contours that mark the flame edge. Raw laser sheet flame images (for example, see Figure 14(a)) are first smoothed with a median filter to suppress noise and then corrected for laser intensity variations, see Figure 14(b). The flame intensity gradients are then calculated at every point in the image as shown in Figure 14(c). Only gradients over a certain threshold are accepted and the resulting contour is taken as the flame location, as shown in Figure 14(d) and Figure 14(e). The extracted flame edge were overlaid with the raw image and found to very closely conform to the visually deduced flame shape. The choice of the threshold level was 30% of the maximum value of the flame intensity gradient for a stable flame.

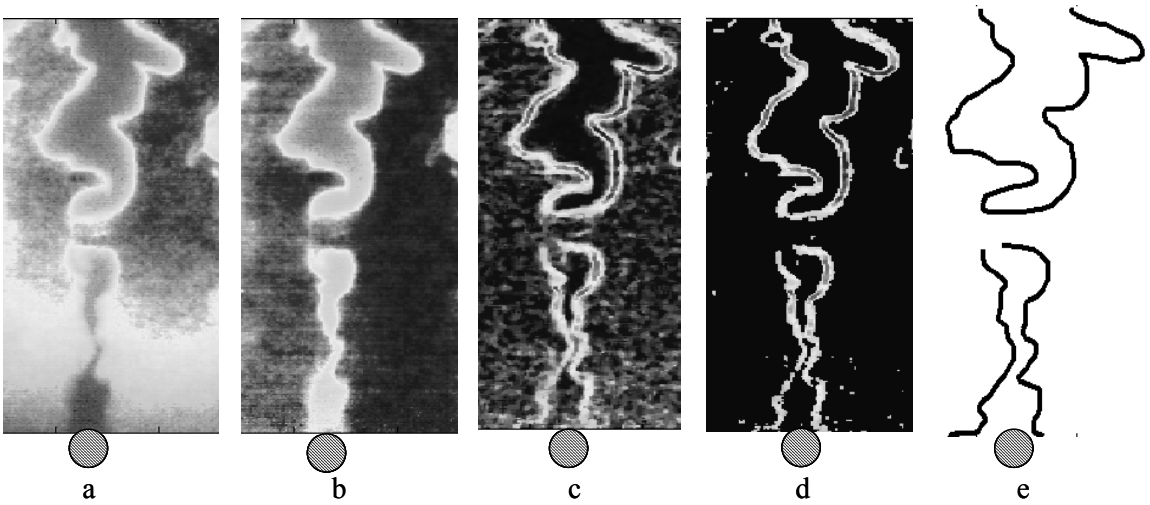

Figure 14: Flame edge tracking: a) Raw image, b) Corrected image, c) Flame intensity gradients, d) Flame image after thresholding and e) Flame edge. Flow direction is from bottom to top.

A suitable way of selecting a threshold level is by examining the probability density function (PDF) of the intensity gradients of a stable flame, as shown in Figure 15. The figure also shows the extracted image (left) of a stable bluff body flame after thresholding at a value of 0.01. This choice of threshold level was then used to capture the flame edge for a flame close to blowout, in which case it is harder to demarcate the presence of flame holes seen in Figure 14(e). An example of extracted images of a flame (shown in Figure 14) close to blowout is shown in Figure 16 for three different choices of thresholding levels of 0.015, 0.012 and 0.01.

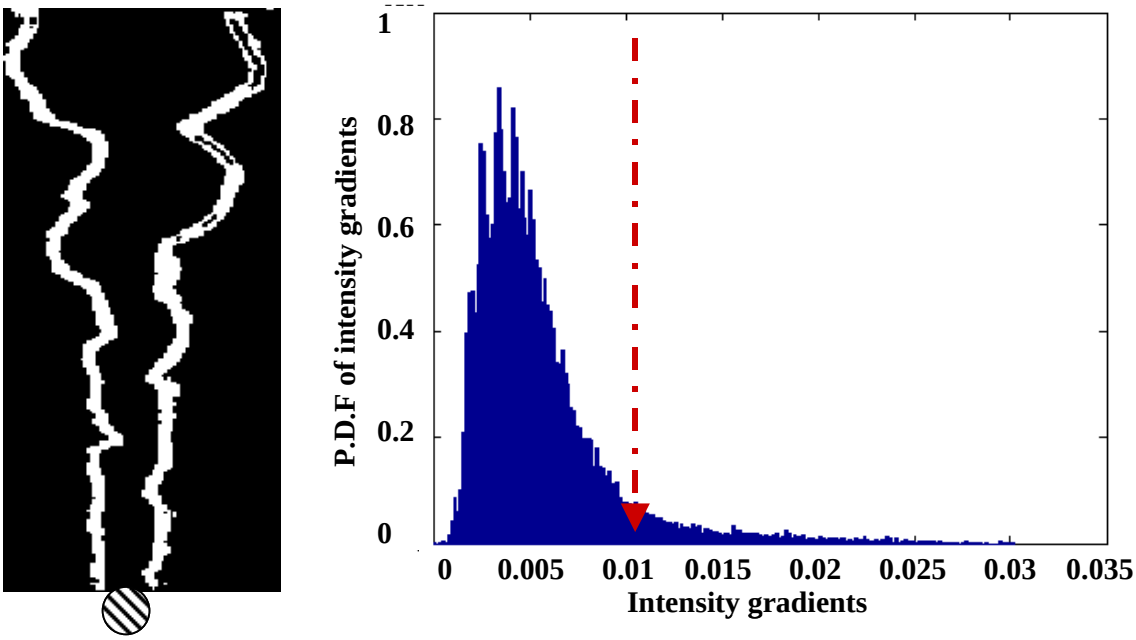

Figure 15: Probability density distribution of flame intensity gradients of the flame shown to the left.

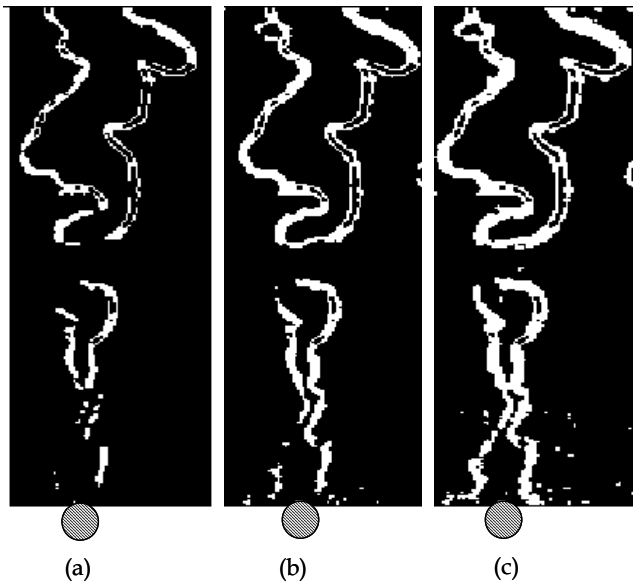

Figure 16: Extracted images of a bluff body flame close to blowout after thresholding at values of a) 0.015, (b) 0.012 and (c) 0.01.

In addition, the PIV images were used to capture the flame edge. The flame edge was extracted from the instantaneous PIV images by demarcating the regions of high and low seeded flow, as shown in Figure 17. Once the regions were demarcated, the boundary of the flame was tracked using the Matlab code "*bwtraceboundary*" and then spline fit. Because of the lower sampling rate relative to the above described imaging studies, they could not be used to visualize the temporal dynamics of the flame, for example through an extinction event, but were quite useful for providing qualitative snapshots of the flow field.

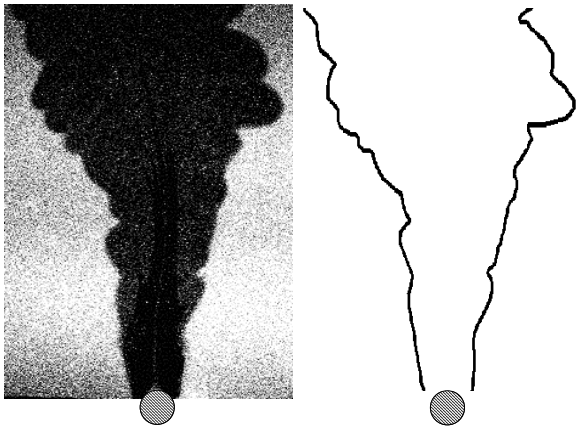

Figure 17: PIV snapshot of a stable flame (left) and the extracted flame edge (right). Flow direction is from bottom to top.

3.3 Data Acquisition and Processing

3.3.1 Data Acquisition

The signal output from the sensors was low pass filtered by a Krohn-Hite Model 3362 digital Butterworth filters and then fed into a 12 bit National Instruments A/D board. The low pass filter frequency and sampling frequency varied with combustor and will be provided in the respective sections. Typical sample sizes were of the order of 2^{16} data points to facilitate ensemble averaging and minimize bias error. LABVIEW, a graphical programming language by National Instruments, was used for data acquisition. A program written in LABVIEW processed the data collected on the A/D data acquisition board, and displayed and stored all the relevant information. All the electronics were grounded to minimize electrical noise. Sheathed BNC cables were also used to minimize cable noise.

The temperatures from the thermocouples and the flow rates from the flow rate meters and pressure gauges were manually read.

3.3.2 Signal Analysis Strategies

Developing data analysis schemes with maximum sensitivity, speed and robustness requires a thorough understanding of the flame characteristics prior to blowout. The high-speed flame images obtained and analyzed in conjunction with simultaneous acoustic data were used to aid the development of such schemes. These analyses revealed that as the flame approached blowout, the average spectral characteristics of its acoustic emissions changed, particularly in the case of the piloted burner which are explained in Chapter 4. In addition, increases in number and duration of time-localized bursts ("events") in the signal were often observed in the swirl and bluff body burners, which will be seen in Chapter 5 and Chapter 6. Based upon these observations, three basic signal-processing methods were used for extracting blowoff precursors: conventional spectral or wavelet-based time-frequency analysis, statistical analysis and threshold-crossing analysis. Conventional power spectra were estimated by dividing the raw data record into ensembles (typically 32). Power spectral densities (PSD) were obtained for each ensemble and then averaged. The primary limitation of this approach is its insensitivity to time-localized events. This shortcoming can be circumvented to some extent (within the limitations of the time-frequency uncertainty principle[91]) with time-frequency data analysis using the wavelet transform. The wavelet transform is defined as:

$$f_{\psi}(t) = \int_{t'} W((t' - t)/\psi)p(t)dt' \qquad (6);$$

where p(t) is the raw time series data, ψ is a scaling parameter, and W(t) is the wavelet basis function. For example, the "Mexican Hat" wavelet is given by:

$$W_1(t) = \frac{2}{\sqrt{3}}\pi^{-1/4}(1-t^2)e^{-t^2/2} \quad (7);$$

The wavelet operation is a generalization of a moving Fourier transform, which can be recovered by replacing the kernel W(t) by the complex exponential, e^{-it}. In this case, the parameter ψ is the inverse of the frequency, $\psi = 1/f$. In general, note that this convolution operation depends upon two parameters: translation, t, and dilatation, ψ. Its basic operation is to determine how much the pressure in some localized interval around time, t, "looks like" the wavelet basis function W(t) at the scale, ψ. Thus, it can be used for detection of features with certain prescribed characteristics and time scales. This is useful for cases where we know *a priori* the temporal characteristics of the blowout precursor. By defining a wavelet with these characteristics, the wavelet operation can be used to extract such precursors from noisy data.

Statistical approaches were also used to detect changes in acoustic signal statistics. Calculating higher order moments is useful as they are sensitive to intermittent events in the signal. The n^{th} statistical moment is defined as:

$$\frac{1}{T}\int_{t=0}^{T}(p(t)-\bar{p})^n\,dt \quad (8);$$

where p and $\bar{p}$ are the instantaneous and average pressures, respectively. Finally, straightforward thresholding or maximum/mean ratio analysis was used to detect time-localized events in the signal, such as large bursts during extinction or re-ignition. The basic idea behind this approach is to count the number of times the instantaneous signal level crosses a threshold value, usually defined as some multiple of the signal's mean or

R.M.S. Because the acoustic signal is a spatially integrated measure of the unsteady heat release over the entire flame, very pronounced changes in the heat release in a localized region of the flame may not be very evident in the overall signal. As such, we found thresholding techniques to be most useful when performed after pre-processing of the acoustic data, such as with a wavelet filter or moving average statistical moment.

Consider the following issues and tradeoffs associated with three key performance metrics of a blowout detection scheme:

1. *Time response* is a critical feature if it is to be used in systems where blowout is to be avoided during fast transients. For example, a time response of less than one second is required in a high performance military engine, which must remain stable during very rapid throttle increases or decreases. A key tradeoff exists between fast time response and robustness, as false alarms can be minimized and confidence in blowout proximity can be maximized by increasing the amount of data considered in estimating blowoff proximity.

2. *Sensitivity*: Consider the dependence of some quantitative blowout indicator, I_v (e.g., number of signal threshold crossings) upon a parameter that affects the flame stability, P_{FS} (e.g. equivalence ratio, pilot level, mean pressure), see Figure 18. First, it is critical that the ratio of I_v near blowout to when the flame is well stabilized should be very large relative to inherent noise or uncertainty, i.e., $I_{v,\,blowout}/I_{v,\,\text{“safe”}} >> 1$. Second, the indicator value should have a one-to-one correspondence with blowout proximity; i.e., it should increase monotonically as blowout is approached. All five curves shown in Figure 18 satisfy this requirement. The third issue related to sensitivity is the functional dependence of I_v upon P_{FS}. Referring to Figure 18, it seems preferable that the curves have a change in gradient, dI_v/dP_{FS} near blowout, such as is manifested in curves 3, 4,

and 5. In contrast, the dependence of I_v upon P_{FS} in curve 1 is not ideal as I_v achieves significant nonzero values even when the system is still very "safe" and dI_v/dP_{FS} has a constant value that is independent of P_{FS}. Fourth, the optimal P_{FS} value where the dI_v/dP_{FS} change occurs is important. Preferably, it should not be overly conservative and occur in regions that are still quite safe, e.g., curve 2. However, it should not also occur too close to the point of blowoff, such as curve 5.

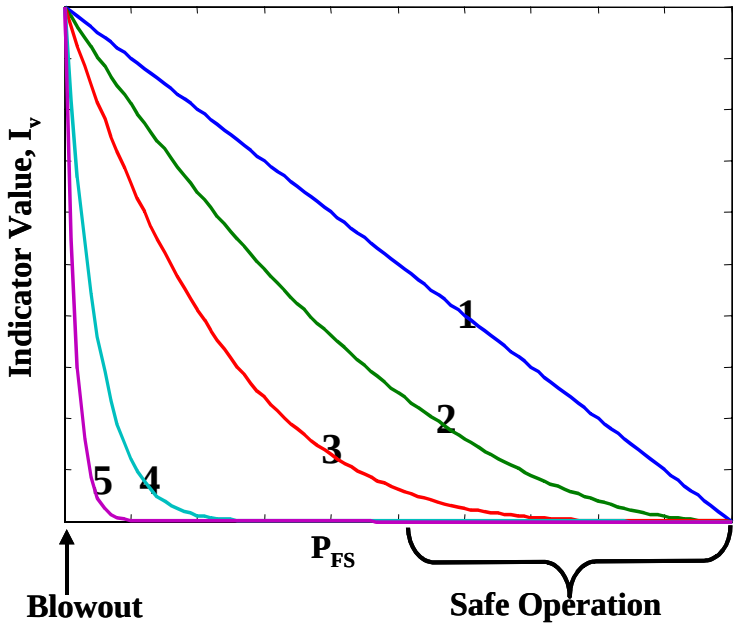

Figure 18: Dependence of a quantitative blowout indicator, I_V, upon a parameter affecting flame stability, P_{FS}.

As we will show later, the shape of the. I_v vs. P_{FS} curve can be manipulated to some extent through suitable changes in signal processing parameters, such as threshold levels. There is often a tradeoff in these first and fourth requirements as signal processing parameters that result in larger $I_{v,\text{ blowout}}/I_{v,\text{ "safe"}}$ values generally result in P_{FS} vs. I_v curves

resembling curves 1 or 2. In contrast, the more ideal curves 3 or 4 often have substantially lower $I_{v,blowout}/I_{v,\text{“safe”}}$ values.

3. Robustness: As mentioned above, the signal analysis approach must also be robust to inherent levels of noise and uncertainty. Obviously, robustness of a particular approach is enhanced by having a large number of ensembles of data in order to average out noise. In addition, I_v values at a fixed P_{FS} must be relatively insensitive to small deviations in signal processing parameters (e.g. threshold level) and system aging

CHAPTER 4

PILOTED BURNER STUDIES

This chapter presents experimental results that characterize the acoustic emissions from a piloted burner under lean blowout conditions. Specifically, Section 4.1 deals with blowoff phenomenology of the piloted flame and Section 4.2 looks at the various techniques developed to detect characteristics of acoustic emissions close to blowout.

Piloting is one of the most commonly used methods for flame stabilization. Because of the simplicity and the lack of a large number of dependent parameters, it makes it an ideal burner for fundamental laboratory studies.

4.1 Flame blowoff phenomenology

A schematic of the 50 KW piloted burner used in this study is shown in Figure 8 (Section 3.1). Measurements from this combustor were taken at atmospheric conditions in an anechoic chamber to ensure a high signal/noise ratio. Acoustic oscillations were measured with calibrated, Bruel and Kjaer type 4191, 13mm condenser microphones. The microphones were located ~61 cm from the combustor exit at ~30^{o} from the flow axis. Their output was low pass filtered at 1 kHz. A total of 65,536 (i.e., 2^{16} points) data points were obtained at a sampling frequency of 2 kHz.

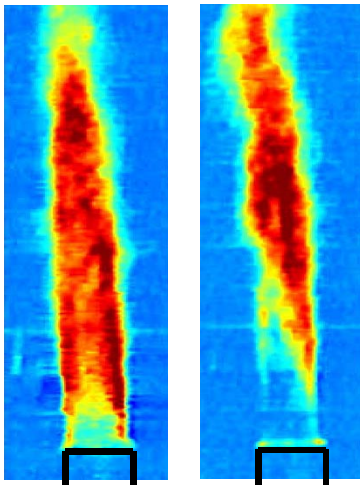

Figure 19: High speed camera images of stable flame (left) and flame close to blowout (right) corresponding to 4% and 0.8% of fuel in pilot, respectively, at an equivalence ratio, $\phi = 0.88$, u = 16 m/s for the piloted burner.

High-speed images are presented in conjunction with simultaneous acoustic data to motivate the data-analysis schemes described in the next section. For the piloted burner, data were obtained under several operating conditions where both the main and pilot fuel and air flow rates were varied. The velocity in the main flow was maintained at high values (> 15 m/s) so that the flame could only be stabilized with the pilots on (without the pilot, the main flame can only be anchored for velocities below ~1 m/s). The flame's proximity to blowout was controlled via the flow rate of fuel to the pilot, which was operated fuel rich. The overall equivalence ratio was varied between 0.6 and 1.1. The Reynolds number in the combustor varied from 15,000 to 30,000. Representative data shown here were acquired at an equivalence ratio of $\phi = 0.88$, average cold flow velocity of u = 16m/s, and piloting fuel fraction ranging from 5% to <1% of the total fuel flow. Figure 19 shows images of the flame when it is stable (4% pilot) and near blowout (0.8% pilot). As blowout is approached, the flame no longer symmetrically attaches around the edge of the burner. Instead, it periodically detaches from one side of the burner, remains

anchored by several pilot holes, and then reverts back to its symmetric stabilization. This phenomenon of detachment and reattachment increases in frequency and duration as the blowout point is approached. Very near the blowout point (figures on the right), the flame anchors only on a few pilot holes and does not exhibit this unsteady detachment/reattachment behavior. When the flame is not uniformly attached, the tip region flaps radially back and forth more violently than when it is well stabilized. This is likely the reason for its enhanced low frequency emissions near blowout, as shown in Figure 20. This figure plots typical time dependencies of the combustion noise measured from the piloted burner as it approaches blowout.

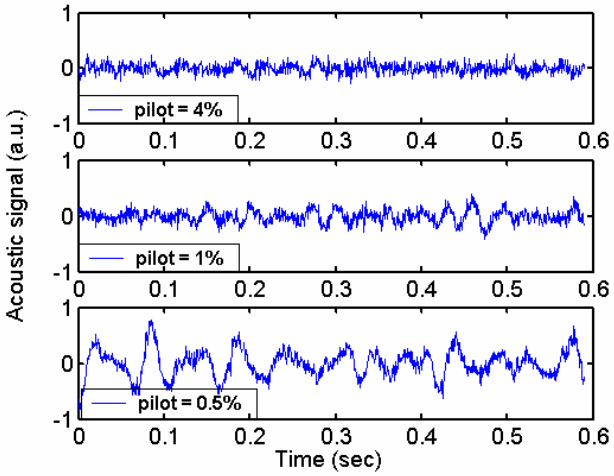

Figure 20: Acoustic signatures from a piloted burner for piloting percentages of 4.0, 1.0 and 0.5 % at $\phi = 0.88$.

These results are in agreement with the findings of Rajaram and Lieuwen,[92] who suggest that the flame tip plays an important role in the low frequency acoustic emissions of a burner similar to the one used in this study. Similarly, Katsuki et al.[41] also found that

the flame tip has the maximum heat release fluctuation and hence, is the maximum combustion noise contributor. The above two referred works concluded on the fact that the presence of a flame tip was necessary for low frequency combustion noise and that it was the point of maximum heat release. Since our findings show increased flame tip fluctuations and corresponding increase in low frequency acoustics as the burner is brought closer to blowout, we can conclude that flame tip unsteadiness was predominantly responsible for the low frequency combustion noise.

The preferential anchoring location of the flame near blowout is due to non-uniformities in the pilot flow velocity, see "pilot design 1" curve in Figure 21. As indicated in the figure, the circumferential velocity non-uniformity is about 40%. The last point where the flame anchors before blowoff coincides with the point of lowest velocity. The same behavior was observed in a second burner designed specifically to have a more uniform pilot flow, see the curve labeled "pilot design 2" in Figure 21.

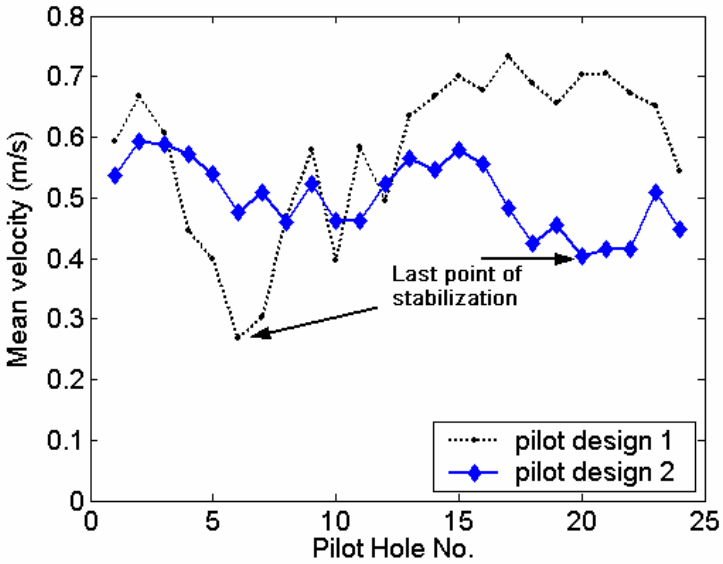

Figure 21: Cold jet velocity measurements at the pilot-hole centerlines for two piloted burner designs.

4.2 Acoustic Signal Analysis

Fourier analysis of the acoustic data from the piloted burner was performed to illustrate the change in signal characteristics at different frequencies. Figure 22 (left) depicts the acoustic spectra from the piloted burner at three different piloting levels, ranging from a condition where there is sufficient pilot fuel so that the flame is well stabilized (5%), to a point very near blowout (0.6%) at a fixed equivalence ratio, ϕ = 0.88. As indicated in the figure, there is a marked increase in the 10-150 Hz frequency regime under these near blowout conditions. Note also the strong peak that appears in the vicinity of 15 Hz under near blowout conditions. Data taken at several flow velocities and burner diameters also exhibited a similar peak at 15 Hz. A similar peak is faintly seen in the cold flow noise spectra and is apparently amplified in the reacting case. These data indicate that the proximity of the combustor to blowout can be monitored via acoustic power in the low frequency bands. The right half of Figure 22 plots the dependence of the acoustic power in the 10-100 Hz and 10-20 Hz frequency range, normalized by the total power in the acoustic signal, upon piloting level. The plot is scaled by the minima for comparison with other burners. The figure shows that the power in the 10-100 Hz spectral band increases by a factor of 8 as blowout is approached. Note that higher sensitivity can be achieved by examining a similar ratio, but using a narrower bandwidth (10-20 Hz).

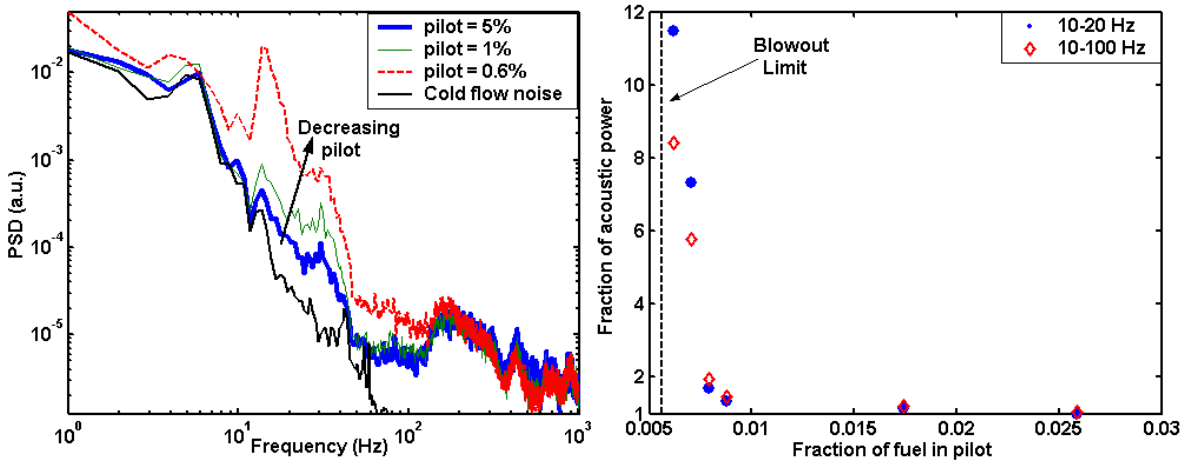

Figure 22: Acoustic spectra of cold flow noise and combustion noise from the piloted burner for piloting percentages of 5.0, 1.0 and 0.6% at ϕ= 0.88 (left); and the dependence of the normalized acoustic power (scaled by the minima) in the 10-100 Hz and 10-20 Hz frequency bands upon piloting level (right).

To conclude, it was found that the flame detached from one side of the burner and showed increased flame tip fluctuations close to blowout. Measurements in two different burners found that that the last point where the flame anchors before blowout coincides with the point of lowest velocity. Combustion noise was found to be dominant in the low frequency regime of the acoustic spectra, which was associated to the amplified flame tip undulations. The next chapter deals with similar experiments on a premixed swirl combustor and includes details of the wavelet, statistical and thresholding approaches in depth.

CHAPTER 5

SWIRL BURNER STUDIES

This chapter presents experimental results that characterize the acoustic emissions from premixed swirl combustors under conditions near lean blowout. The chapter is divided into three sections. The first section focuses on a fundamental, atmospheric swirl-dump combustor. The blowoff phenomenology of the atmospheric swirl stabilized flame is discussed and the results of a variety of acoustic signal processing approaches are described. The analysis is applied to a high-pressure combustor rig in the second section and to a non-premixed aircraft combustor simulator in the final section.

5.1 Atmospheric Swirl Combustor

5.1.1 Blowoff Phenomenology

A schematic of the 100 KW swirl burner used in this study is shown in Figure 9 (Section 3.1.2). Simultaneous chemiluminescence (see field of view in Figure 9) and acoustic measurements were obtained from the swirl combustor. Though some chemiluminescence results will be presented, this work will mainly focus on acoustic sensing. Acoustic oscillations were measured with Bruel and Kjaer type 4191, 13mm condenser microphones that were located ~61 cm from the combustor exit at ~30^{o} from the flow axis. Their output was low pass filtered at 1 kHz. A total of 65,536 (i.e., 2^{16} points) data points were obtained at a sampling frequency of 2 kHz.

The proximity to blowout was controlled by the equivalence ratio, which was adjusted via the overall fuel flow rate while keeping the overall airflow fixed. The data presented here correspond to a bulk average velocity of 6.6 m/s at the combustor exit under cold, atmospheric conditions. The overall equivalence ratio was varied between 0.7 and 1.1. The blowout equivalence ratio for this combustor is just below 0.74 for the flow conditions used. Figure 23 plots a time-averaged image of a stable flame at an equivalence ratio normalized by its value at blowout, ϕ/ϕ_{LBO} of 1.07 (extreme left image) and a sequence of images of a flame close to blowout, ϕ/ϕ_{LBO} of 1.03 (figures on the right), separated by 16 ms. The dark regions in these inverted grayscale images represent regions of high flame intensity (i.e. chemiluminescence over all visible wavelengths), while the white implies low intensity regions in the combustor. The boundary of the combustor is marked by the dark line on the border of the images. The inlet and the flow direction are also indicated. In the $\phi/\phi_{LBO} = 1.07$ case, there is always a well-defined combustion region. The average flame, in general, appears to be stabilized just downstream of the inlet. Near blowout, the flame appears to be detached from the inlet and has reduced intensity due to decreased heat release at lower equivalence ratios. Then, the flame begins to disappear from the field of view and at some point, there is an almost complete loss of flame. Then, the radiation signal re-appears, suggesting that the unburned fuel entering the combustor during the previous period is being consumed. Re-ignition may be due to presence of hot products in the combustor or the contact of the unburned gases with the hot quartz wall, also observed in prior work.[93] This process then repeats itself (not shown in figure). The occurrence and duration of these extinction and re-ignition events were observed (from the movie images) to increase as the flame

approaches lean blowout, as discussed later. As the number of these events increase in time, the combustor temperature drops due to heat losses and the overall flame appears to become significantly weaker. Finally at an equivalence ratio of around 0.74, the flame blows out.

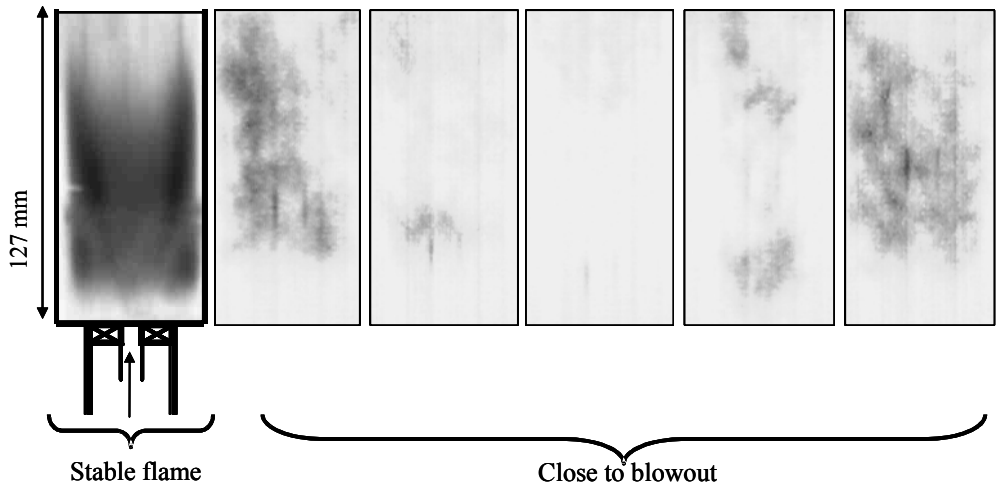

Figure 23: High speed camera images of an average stable flame (extreme left) at a $\phi/\phi_{LBO} = 1.07$, and of flames, separated by 16 ms, close to blowout (right) at $\phi/\phi_{LBO} = 1.03$, u = 6.6 m/s for the swirl burner.

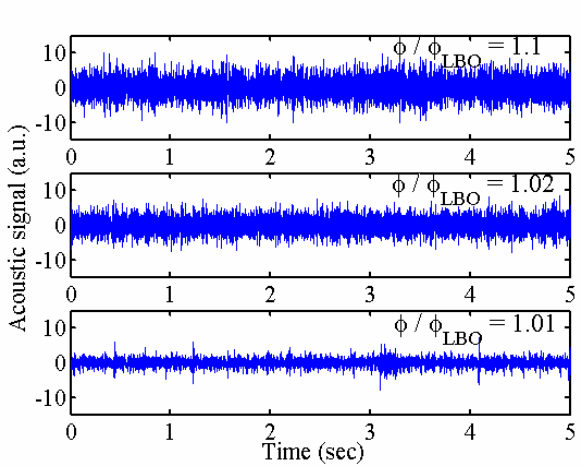

Figure 24: Acoustic signal from the swirl burner for $\phi/\phi_{LBO} = 1.1$, 1.02 and 1.01.

Figure 24 plots typical measured time dependencies of the acoustic pressure at several normalized equivalence ratios, ϕ/ϕ_{LBO} = 1.1, 1.02 and 1.01. Note the reduction in RMS pressure levels with lowered equivalence ratio. This is due to the reduced heat release rates[39] at the lower fuel flow rates. Near blowout, short time duration, high amplitude bursts are observed. Comparison of these time series with corresponding OH^* chemiluminescence signatures (see Figure 26) and high speed video images indicate that these bursts often coincide with the occurrence of the flame loss and re-ignition events described above. Next, we look at various approaches to quantify the proximity of the combustor to blowout.

5.1.2 Spectral Approaches

The combustion noise spectra of the swirl burner at two different normalized equivalence ratios, ϕ/ϕ_{LBO} = 1.1 and 1.01 are plotted in the left half of Figure 25. The ϕ/ϕ_{LBO} = 1.01 curve is normalized to have the same total acoustic power as the ϕ/ϕ_{LBO} = 1.1 case. Note that the cold flow noise spectra is un-normalized and can be compared only to the acoustic spectra for the ϕ/ϕ_{LBO} = 1.1 case. These curves are normalized in order to correct for the change in the total fuel flow rates. The higher heat release rates in the ϕ/ϕ_{LBO} = 1.1 case resulted in higher total sound power emissions. Note that in the piloted burner case, the equivalence ratio and the total fuel flow rates changed minimally (<3%). As indicated in the figure, there is a marked increase in power in the 10-100 Hz spectral regime under these near flameout conditions. The low frequency increase is likely related to the two time scales associated with the precursor events observed in the acoustic signal in Figure 24 and Figure 26. The first time scale, observed to be around 10-15 ms (~100 Hz), corresponds to the duration of the re-ignition event, when there is a

sudden increase in pressure amplitude. The second time scale is the time between such events, which is typically around 100-200 ms (~5-10 Hz). Figure 25 (right) plots the dependence of the acoustic power in the 10-100 Hz and 10-30 Hz frequency ranges normalized by the total power in the acoustic signal against normalized equivalence ratios. The power in these spectral bands increases by a factor of nearly 60 near blowout.

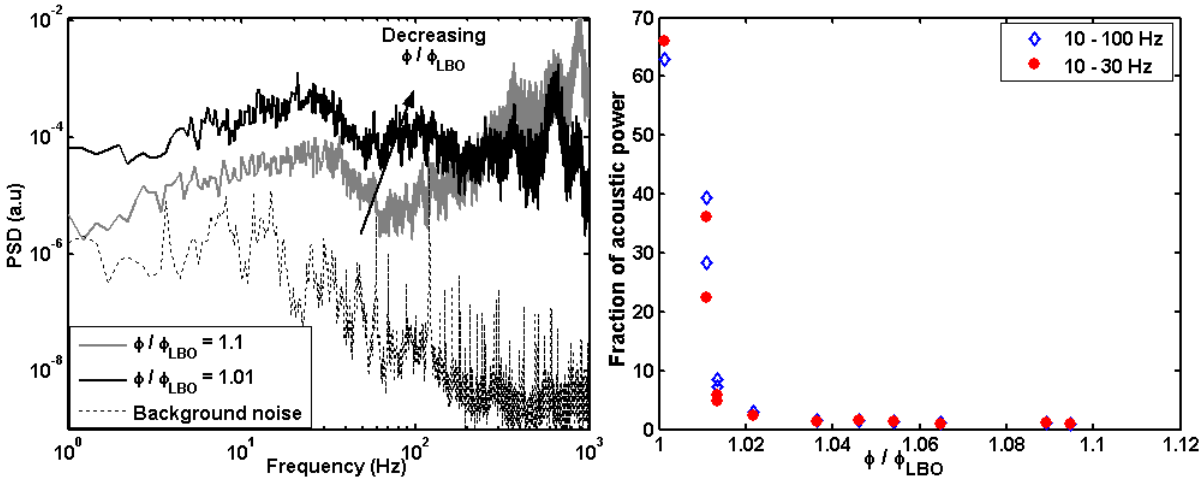

Figure 25: Acoustic spectra from the swirl burner for $\phi/\phi_{LBO} = 1.1$ and 1.01 (left); and the dependence of the normalized acoustic power (scaled by the minima) in the 10-100 Hz and 10-30 Hz frequency bands upon ϕ/ϕ_{LBO} (right).

5.1.2 Time-frequency /Wavelet Approaches

The primary limitation of the spectral approach is its insensitivity to time-localized (non-periodic) events. This shortcoming can be circumvented to some extent (within the limitations of the time-frequency uncertainty principle[91]) with time-frequency data analysis using the wavelet transform, as described in Section 3.3.2.

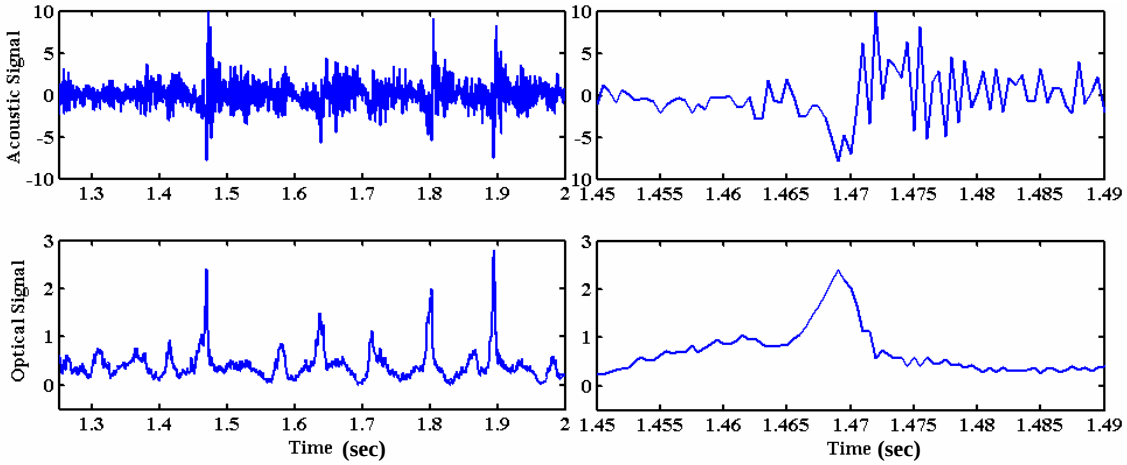

Figure 26: Acoustic and OH* chemiluminescence time series data from the swirl burner for $\phi/\phi_{LBO} = 1.02$, 2.5 second time segment (left); and detail of the blowout precursor in the acoustic and optical signal (right).

Wavelets were found to be most useful for the swirl burners where time localized events in the signal (which do not have a large impact on the average spectra) become more pronounced. In contrast, straightforward Fourier analysis is sufficient for the piloted burner (as shown in Figure 22 (right) in Section 4.2) where the overall "average" characteristics of the signal change and the time-localized events are less evident.

In order to increase sensitivity, "customized" wavelets were generated that resembled the actual acoustic events close to blowout. The temporal characteristics of these events were determined from simultaneous analysis of OH* chemiluminescence and the acoustic signal. Figure 26 shows a plot of acoustic and optical data at an equivalence ratio close to blowout. A detail of these data is also shown in the right half of Figure 26. The large dips in the optical signal coincide with local temporary flame loss, while the sharp peaks coincide with re-ignition events. A coincident feature is also evident in the acoustic

signal, which resembles the derivative of the OH^* signal, as expected[39]. A rough estimate of the number and duration of acoustic precursor events can be made from Figure 26.

A customized wavelet having a waveform shape similar to the acoustic signature during the precursor event in Figure 26 was generated with a functional dependence given by

$$W_2(t) = -\frac{d}{dt}(e^{-t^2/2}) \qquad (9)$$

Figure 27 (left) plots the computed $W_2(t)$ wavelet coefficients at a scale ψ = 1/10 sec. In contrast to the overall signal variance, see Figure 24, the wavelet-filtered variance actually increases as the combustor approaches blowout. In addition, large amplitude bursts in the signal ("events") are increasingly obvious. Figure 27 (right) plots the variance of the calculated $W_2(t)$ wavelet coefficients at scales, ψ = 1/10 and 1/125 seconds respectively. The figure shows that the power in the scale or "frequency" band increases by a factor of 60 and 40 respectively near blowout conditions. Note the similarity of these values to those obtained from the power spectrum (shown in Figure 25). The variations are lesser for other scale choices.

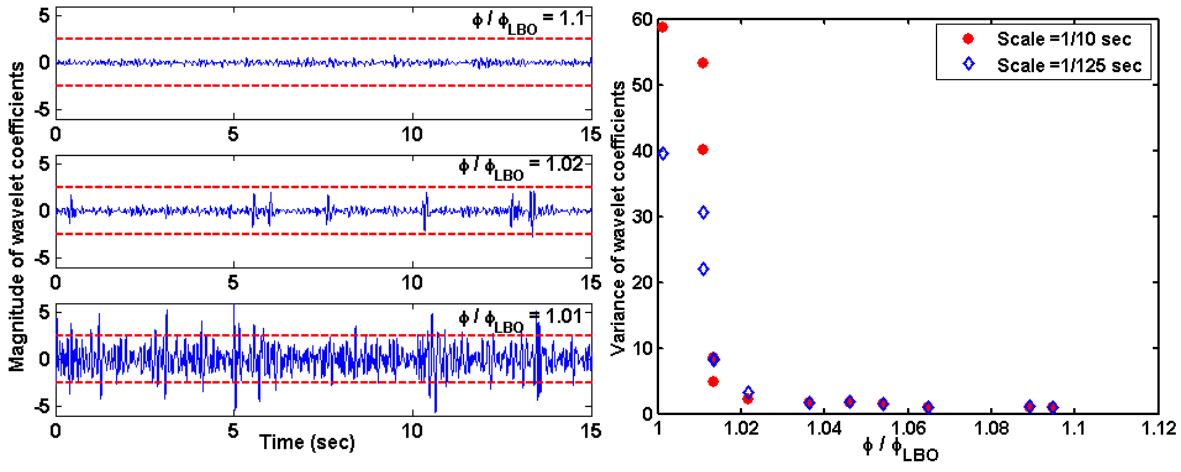

Figure 27: Time dependence of acoustic $W_2(t)$ wavelet coefficients at $\psi = 1/10$ seconds for $\phi/\phi_{LBO} = 1.1$, 1.02 and 1.01 (left); and the dependence of $W_2(t)$ wavelet coefficient variance at $\psi = 1/10$ and 1/125 seconds upon ϕ/ϕ_{LBO} for the swirl burner (right).

Another important point to note is that other wavelet base functions give comparable results; i.e., the sensitivity of the wavelet coefficient variance upon basis function is minimal for a given ψ. This can be understood by noting that the wavelet filtering operation is equivalent to streaming the data through a pass-band filter. A straightforward application of Parseval's theorem shows that the variance of the filtered data will be quite similar for a variety of different wavelets whose Fourier transforms have similar center frequencies and bandwidths. What then is the advantage of identifying a "customized" wavelet? As suggested in the next section, the key advantage lies in the ability of the customized wavelet to accentuate the amplitude of time-localized events whose shape resembles that of the wavelet. As such, the choice of wavelet impacts the statistics of the filtered signal outliers (time-localized events) whose presence we are interested in detecting. *Therefore, the key advantage in customized wavelets lie in using them in conjunction with a discrete event detection algorithm, such as level crossing approaches (discussed in the next subsection), as opposed to a time-integrated detection algorithm, such as a variance calculation.*

5.1.3 Statistical Approaches

The 3rd and higher order statistical moments, M_n, of the acoustic signal were chosen for analysis because of their sensitivity to outlying or intermittent events. Particular focus was given to M_4, the kurtosis of the acoustic data, which increases slightly (~30%) for the swirl burner as it is brought to blowout. This low sensitivity is due to the fact that M_4

averages over the entire data record. As shown in the next subsection, a short time-window moving average kurtosis estimate coupled with a thresholding technique is substantially more sensitive. In contrast, for the piloted burner described in Chapter 4, where only the overall "average" acoustics change, the statistical approaches are not very advantageous.

5.1.4 Thresholding/Level Crossing Approaches

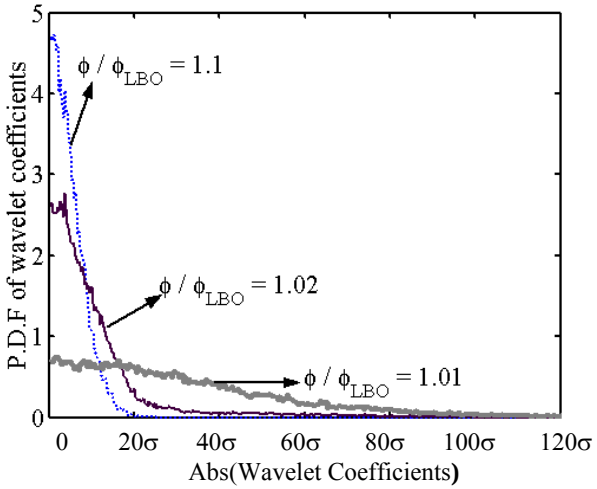

Figure 28: Wavelet transform PDF (using $W_2(t)$) from the swirl burner at a ψ = 1/10s for ϕ/ϕ_{LBO} = 1.1, 1.02 and 1.01.

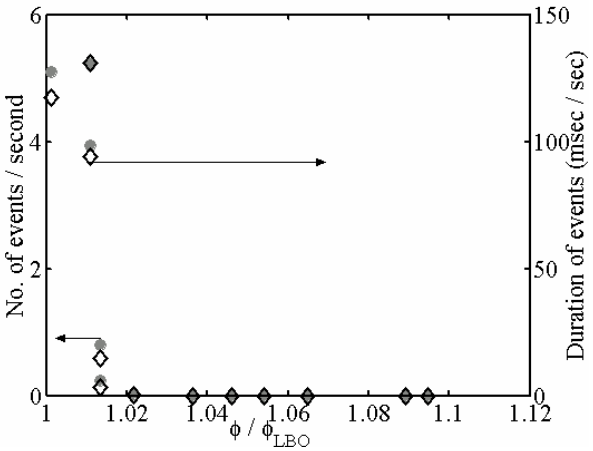

Figure 29: Dependence of the number (●) and duration (◊) of events upon ϕ/ϕ_{LBO} in the swirl burner.

Thresholding the data provides a convenient way of converting a data stream into a quantitative blowout indicator; e.g. a blowout avoidance logic can be invoked when the data exceed a threshold level. A convenient way of choosing a threshold level is by examining the probability density function (PDF), as shown in Figure 28, for the $W_2(t)$ wavelet coefficients for ϕ/ϕ_{LBO} = 1.1, 1.02 and 1.01. The increased presence of high amplitude outliers close to blowout results in the long tail in the PDF.

The figure indicates that the signal from the stable flames rarely exceeds ~30σ, where σ^2 denotes the variance of the $W_2(t)$ coefficients for the stable combustion case, ϕ/ϕ_{LBO} = 1.1. Figure 29 plots the dependence of 60σ level crossing frequency (number of crossings/second) and duration (time the signal exceeds the threshold/total time) upon ϕ/ϕ_{LBO}. This threshold level is shown by the dashed lines in Figure 27 (left). The number and duration of events rises from identically zero to about 5 events/second and 150 ms/second respectively just before blowout, as seen in Figure 29. The effect of threshold level is shown in Figure 30, which plots the dependence of the number of

events upon ϕ/ϕ_{LBO} at threshold levels of 12σ, 22σ and 60σ. Note the two influences of the threshold level: number of events detected and the ϕ/ϕ_{LBO} value where events are first detected. At lower threshold levels, more events are detected. Furthermore, events are detected at higher ϕ/ϕ_{LBO} values. This point was alluded to in Section 3.3.2 in the discussion of Figure 18. The tradeoffs in choosing an optimal threshold level are further illustrated in Figure 31. The left and right y-axes plot the maximum number of events observed before blowout (a measure of sensitivity), and the normalized ϕ value where an event is first observed, respectively. As might be anticipated, higher sensitivity results in more alarms at ϕ values where the flame is still reasonably stable.

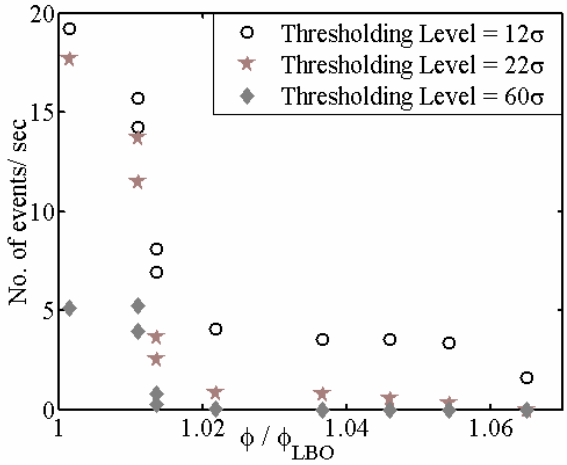

Figure 30: Dependence of the number of events upon ϕ/ϕ_{LBO} for three thresholding levels in the swirl burner, where σ^2 = the variance of coefficients for the stable combustion case, $\phi/\phi_{LBO} = 1.1$.

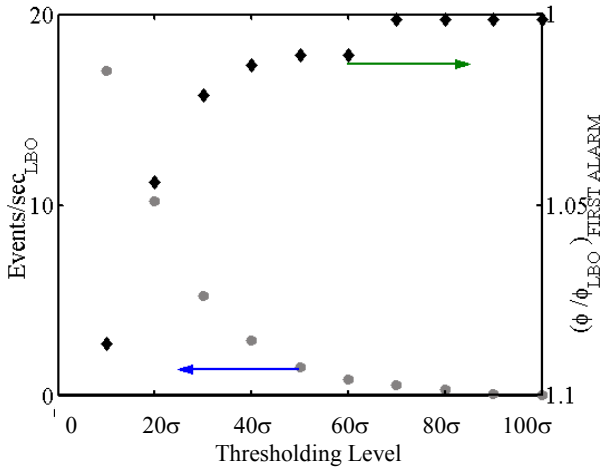

Figure 31: Variation in the number of events near blowout (●) and the ϕ value where an event is first observed (♦) upon thresholding level in the swirl burner.

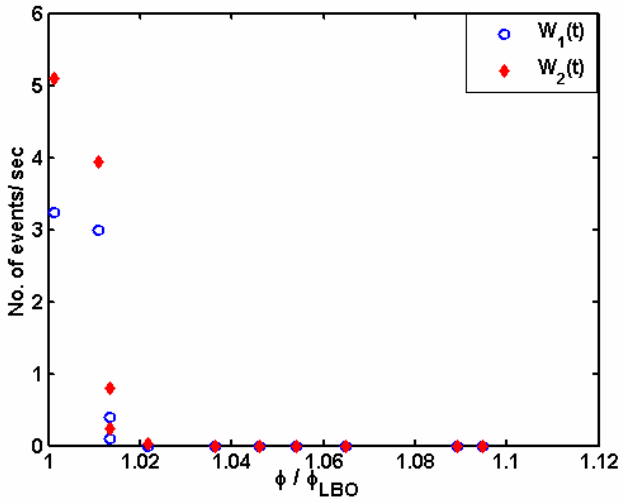

Figure 32: Dependence of the number of events upon ϕ/ϕ_{LBO} for two wavelets, W_1 (Mexican Hat wavelet) and W_2 (customized wavelet), in the swirl burner.

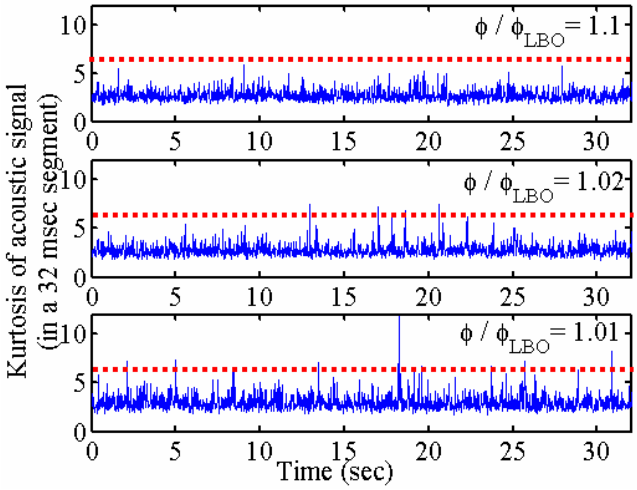

Figure 33: Time variation of 32 ms moving average kurtosis estimate from the swirl burner for $\phi/\phi_{LBO} = 1.1$, 1.02 and 1.01.

As discussed above, the choice of the wavelet basis function has little influence upon the variance of the filtered signal but a larger impact upon the level crossing frequency. The event count of the customized wavelet, $W_2(t)$, was found to be greater than that of the Mexican Hat wavelet, $W_1(t)$, as shown in Figure 32. This indicates that the sensitivity of the thresholding approach at a given scale may be enhanced by a judicious choice of wavelet.

Thresholding is also useful in conjunction with moving average calculations of statistical moments of acoustic signal. The temporal dependence of a 32 ms moving average estimate of the kurtosis of the acoustic data from the swirl burner is plotted in Figure 33 at $\phi/\phi_{LBO} = 1.1$, 1.02 and 1.01. The increased presence of large spikes in the kurtosis estimate is observed as blowout is approached. By applying similar thresholding techniques to these data, comparable results to those shown in Figure 30 were observed here as well.

5.1.5 Chemiluminescence data analysis

Limited analysis of the chemiluminescence data obtained from the swirl burner is also presented for comparison. This will help to understand the acoustic-optical integration techniques described in Appendix B. Figure 34 plots typical measured time dependencies of the OH^* chemiluminescence at normalized equivalence ratios, ϕ/ϕ_{LBO}=1.1, 1.02 and 1.01. The average intensity decreased with equivalence ratio as expected, due to reduced heat release. More importantly, as the combustor is operated closer to its blowout limit, the OH* chemiluminescence occasionally drops to a "near" zero value, indicating the occurrence of the short duration, extinction events. A detailed plot near blowout is also shown in Figure 26.

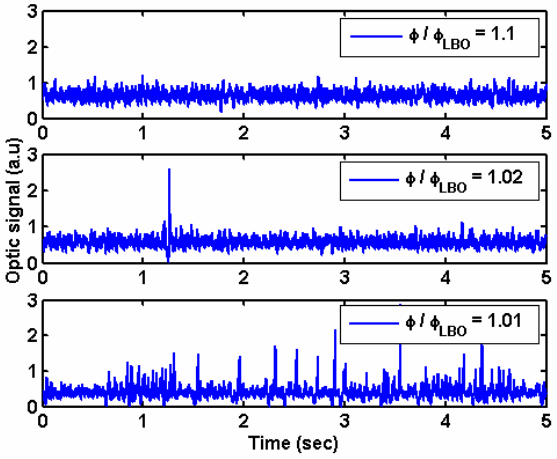

Figure 34: OH^* chemiluminescence signal from the burner for ϕ/ϕ_{LBO} = 1.1, 1.02 and 1.01.

The optical precursors can be easily identified using a simple thresholding method of the raw signal without any prior filtering, where an event is acknowledged when the

signal drops below a threshold level. This choice is based on the premise that the precursor signature is initiated by a local extinction event that temporarily lowers the chemiluminescence. Thus the low threshold approach provides the earliest detection of the event. The threshold value was taken to be a fraction of the time-localized mean OH* signal rather than a fixed value. This removes the dependence of the overall signal on power setting variations, and long-term changes in the fiber (e.g., coating) or detector. Probability distributions similar to that shown in Figure 28 can be used to find an optimal choice of thresholding level.

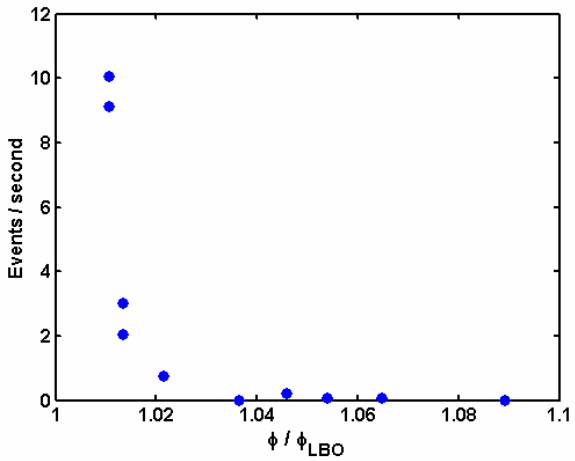

Figure 35: Dependence of the number of chemiluminescence based events upon ϕ/ϕ_{LBO}.

Figure 35 plots the number of chemiluminescence based events versus ϕ/ϕ_{LBO} for a threshold level of 0.25μ, where the local mean signal at a given time, μ, is based on the signal averaged over the previous 0.5 seconds. The number of events rises from zero to about 10 events/second just before blowout. Thus either acoustic or optical based

approach could be used as a blowout proximity measure or a combination of the two parameters could also be incorporated into a control algorithm for more robustness in detecting blowout. More on acoustic-optical data integration can be found in Appendix B.

To conclude, bursts were found in the acoustic signal from an atmospheric premixed swirl burner, which apparently coincide with short, often spatially localized extinction/re-ignition events in the high speed video images and chemiluminescence measurements. These events increase in frequency and duration as the combustor approaches blowout. The enhanced low frequency regime appears to be controlled by the time interval between events and the duration of the events. The next section deals with similar experiments and analysis on a premixed high-pressure swirl combustor.

5.2 High-Pressure Premixed Swirl Combustor Rig

This section deals with similar experimental work conducted in a lean, premixed, high pressure gas turbine combustor simulator. The experimental facility is explained in Section 3.1.4. Tests were performed at a mean pressure of 1.7 atmospheres and mean equivalence ratios ranging from 0.5 to 0.8. Inlet temperatures were kept constant at 470K. Pressure oscillations were measured with a pressure transducer mounted 5.1 cm downstream of the conical flame holder, as shown in Figure 12. A total of 65,536 data points were obtained for each operating condition at a sampling frequency of 4 kHz after being low pass filtered at 2 kHz.

The blowout phenomenology for this combustor is very similar to the atmospheric combustor. The combustor's proximity to blowout was controlled by the equivalence ratio, which was adjusted via the overall air flow rate while keeping the overall fuel flow fixed, and was varied between 0.5 and 0.9. The blow-off equivalence ratio for this

combustor was just below 0.54 for the flow conditions used. A well-defined combustion region is present for the stable flame. Close to blowout, localized extinction and re-ignition events spanning several milliseconds occur semi-randomly in time (with no periodicity). As the lean blowout limit is approached, the frequency and duration of these events increase. These events were very similar to those found in the case of the atmospheric swirl combustor.

Figure 36 plots acoustic pressure time series at two normalized equivalence ratios, ϕ/ϕ_{LBO}=1.12 and 1.03. The RMS pressure levels show a slight increase with decreasing equivalence ratio. The overall heat release is unchanged as the fuel flow rate is fixed while the background jet noise increases due to rise in air jet velocity as the air flow rates are increased to bring the combustor to blowout. Near blowout, short time duration, high amplitude bursts are observed. These bursts coincide with the occurrence of the flame loss and re-ignition events described above.

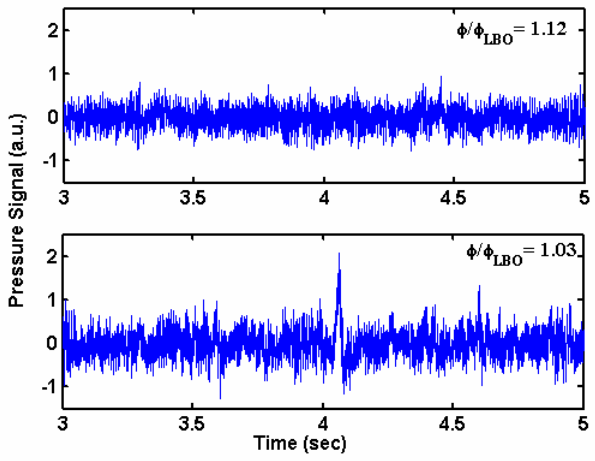

Figure 36: Pressure signal from the high-pressure swirl combustor rig for ϕ/ϕ_{LBO} = 1.12 and 1.03.

Figure 37 plots the combustion noise spectra at two different normalized equivalence ratios, ϕ/ϕ_{LBO} = 1.12 and 1.03. There is a marked increase in power below 100 Hz spectral regime under these near blowout conditions. This low frequency increase appears also to be controlled by the time interval between events (~0.5 s) and the duration of the events (~10ms).

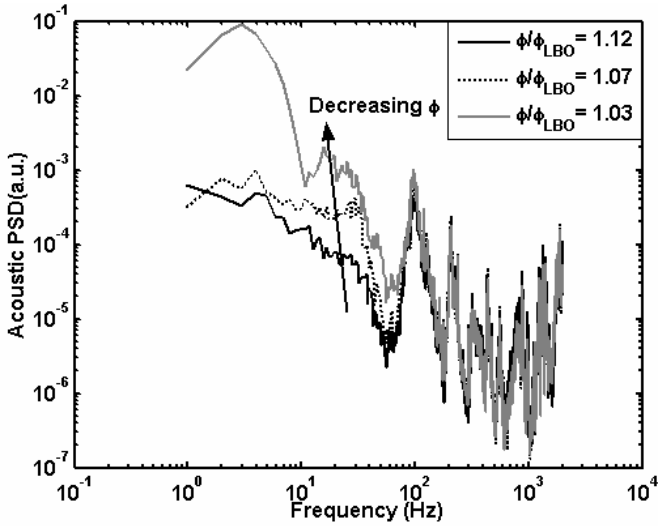

Figure 37: Acoustic spectra of combustion noise from the high-pressure swirl combustor rig for ϕ/ϕ_{LBO} = 1.12, 1.07 and 1.03.

Figure 38 plots the computed $W_2(t)$ wavelet coefficients at a scale of 15 Hz for different normalized equivalence ratios, ϕ/ϕ_{LBO} = 1.12 and 1.03. As the combustor approaches blowout, large amplitude bursts in the signal ("events") are increasingly obvious. Similar probability density functions of the wavelet coefficients as shown in Figure 28 were developed, which indicated that the signal from the stable flames rarely exceeds ~2σ. The dashed lines in Figure 38 correspond to a threshold of 2σ , where σ^2 is the variance of the $W_2(t)$ coefficients for the stable combustion case, ϕ/ϕ_{LBO} = 1.12. As

expected, Figure 39 shows an increase in the number and duration of events from zero for the stable case to 1.5 and 20 respectively close to blowout. These are much smaller than that of the atmospheric swirl combustor.

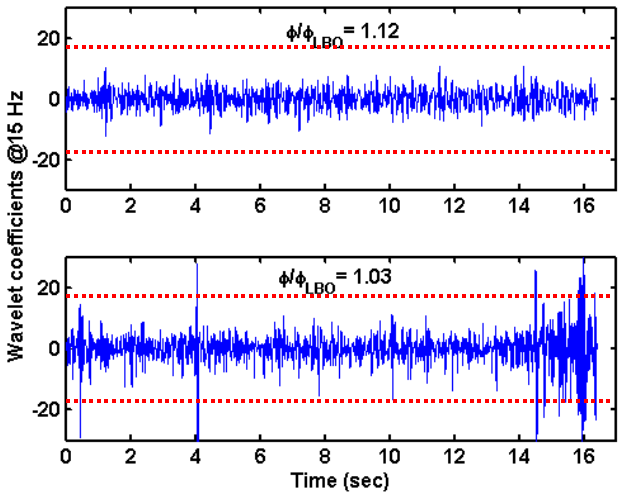

Figure 38: Time dependence of acoustic $W_2(t)$ wavelet coefficients at ψ = 1/15 seconds for ϕ/ϕ_{LBO} = 1.12 and 1.03 from the high-pressure swirl combustor rig.

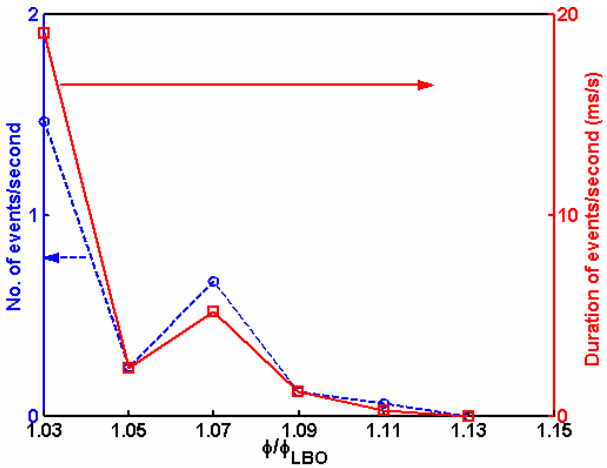

Figure 39: Dependence of the number (○) and duration (□) of acoustic based events upon ϕ/ϕ_{LBO} in the high-pressure swirl combustor rig.

5.3 Non-premixed Swirl Combustor

This section deals with experimental work conducted in a lean, non-premixed aircraft combustor simulator. The experimental facility is explained in Section 3.1.5. Acoustic oscillations were measured with calibrated, Brüel & Kjaer type 4939 condenser microphones that were placed 0.8m away from the combustor exit. A total of 80,000 data points were obtained for each operating condition at a sampling frequency of 4 kHz after being low pass filtered at 2 kHz. The combustor's proximity to blow-off was controlled by the equivalence ratio, which was adjusted via the overall fuel flow rate while keeping the overall airflow fixed. The overall equivalence ratio (i.e., calculated using all the air coming through the front end) was varied between 0.3 and 0.9. The blow-off equivalence ratio for this combustor was just below 0.35 for the flow conditions used.

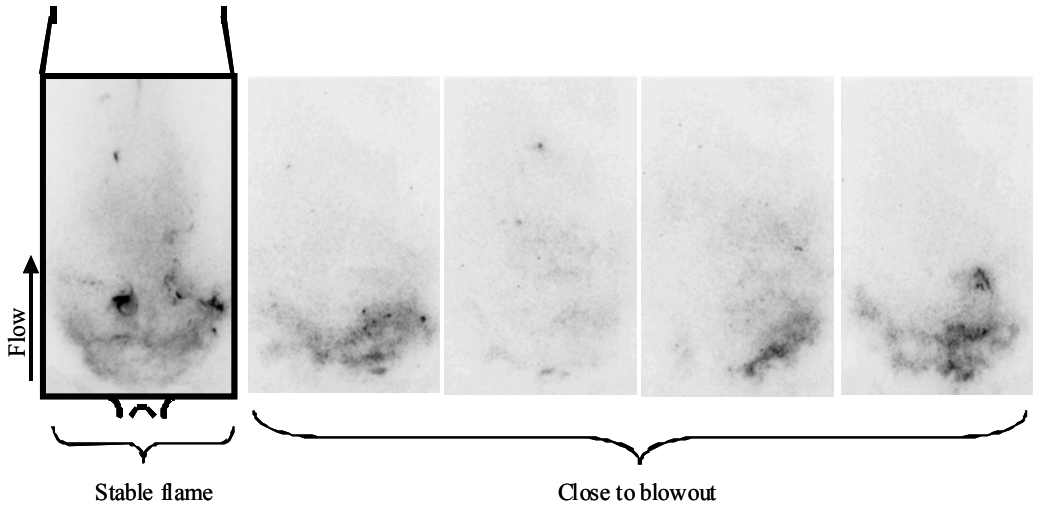

Figure 40: High-speed camera images of a stable flame (extreme left) at a $\phi/\phi_{LBO} = 1.4$, and of flames close to blowout (right) at a $\phi/\phi_{LBO} = 1.01$ taken at a 1 ms interval.

Figure 40 plots a sequence of images (turned counter clockwise) for a stable flame at an equivalence ratio normalized by its value at blowout, ϕ/ϕ_{LBO} of 1.4 (extreme left) and for flames close to blowout, ϕ/ϕ_{LBO} of 1.01. The dark regions in these inverted grayscale images represent regions of high flame intensity. There is always an intense and well-defined combustion region for the stable flames. Close to blowout, a near flame loss event is occasionally seen. In the latter case, the combustor initially has a weaker combustion zone due to reduced heat release. Then, the flame begins to disappear from the field of view, and then re-appears. This process is observed to repeat itself semi-randomnly. These extinction and re-ignition events span a period of several milliseconds, and occur randomly in time (with no fixed frequency) prior to blowout. As the lean blowout limit is approached, the number and duration of these events increase. This phenomenology has also been observed in the case of the atmospheric, premixed swirl combustor and the high pressure swirl rig, and therefore may be universal.

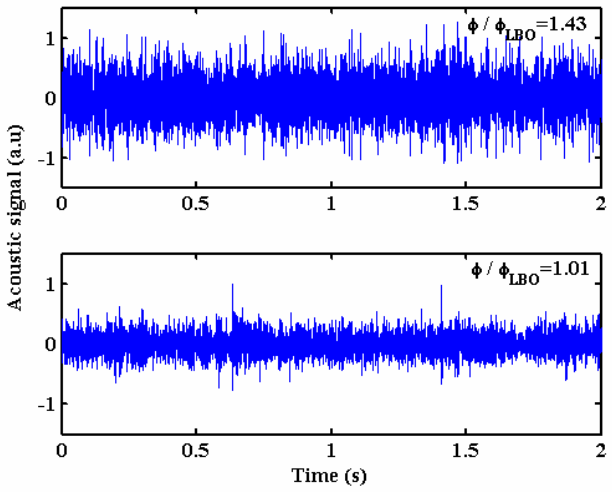

Figure 41: Acoustic signal from the burner for ϕ/ϕ_{LBO} = 1.43 (stable case) and 1.01 (close to blowout).

Figure 41 plots typical measured time dependencies of the acoustic pressure at ϕ/ϕ_{LBO}=1.43 and 1.01. Note the reduction in RMS pressure levels with equivalence ratio, due to the reduced heat release at the lower fuel flow rates. Near blowout, short time duration, high amplitude bursts are observed. These bursts coincide with the occurrence of the flame loss and re-ignition events observed in the simultaneously acquired high-speed video images.

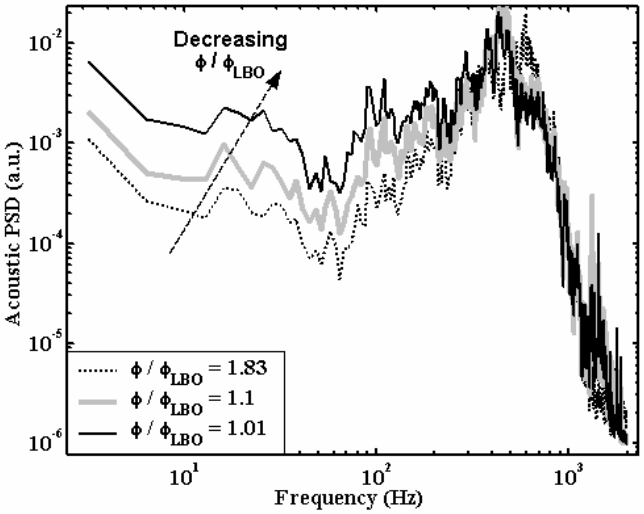

Figure 42: Normalized acoustic spectra of the combustor for ϕ/ϕ_{LBO}= 1.83, 1.1 and 1.01.

The combustion noise spectra at three different normalized equivalence ratios, ϕ/ϕ_{LBO} = 1.83, 1.1 and 1.01 are plotted in Figure 42. Each curve has been normalized to have the same total acoustic power in order to correct for the different fuel flow rates. As indicated in Figure 42, there is an increase in power below 200 Hz spectral regime under these near flameout conditions. This low frequency increase appears to be controlled by the time interval between events (~0.5 s) and the duration of the events (~5-10ms) observed in the

acoustic signal. The acoustic power below 100 Hz frequency range normalized by the total power in the acoustic increases by a factor of nearly 6 as blowout is approached, similar to Figure 25 (right).

Figure 43 plots the computed $W_2(t)$ wavelet coefficients at a scale of 18.5 Hz for different normalized equivalence ratios, $\phi/\phi_{LBO} = 1.8$ and 1.01. In contrast to the signal R.M.S., see Figure 41, the wavelet filtered R.M.S actually increases as the combustor approaches blowout. In addition, large amplitude bursts in the signal ("events") are increasingly obvious. Similar probability density functions of the wavelet coefficients as shown in Figure 28 were developed, which indicated that the signal from the stable flames rarely exceeds ~1.02σ. The dashed lines in Figure 43 correspond to a threshold of 1.02σ (σ^2 is the variance of the $W_2(t)$ coefficients for the stable combustion case, $\phi/\phi_{LBO} = 1.8$).

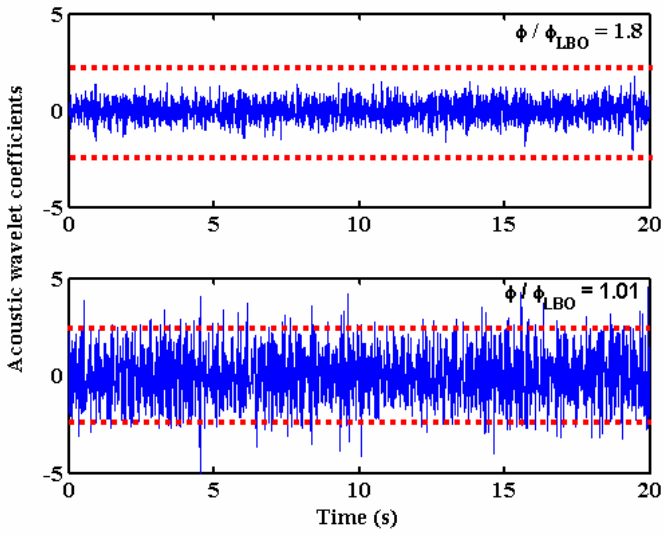

Figure 43: Time dependence of computed $W_2(t)$ wavelet coefficients of acoustic signal at a scale of 18.5 Hz for $\phi/\phi_{LBO} = 1.8$ and 1.01.

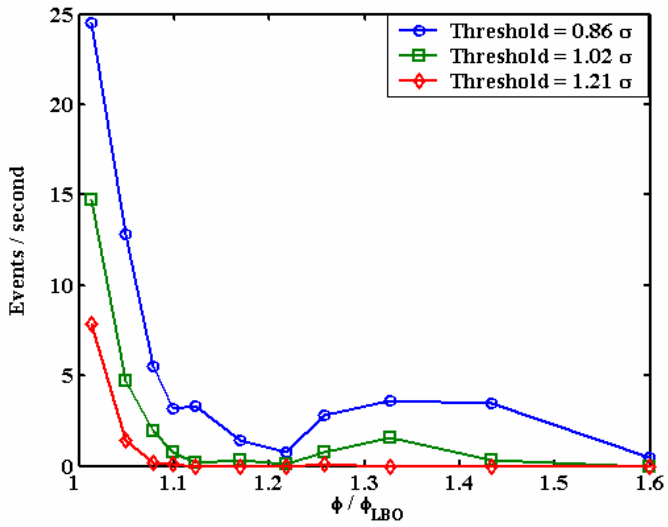

Figure 44: Dependence of the number of acoustic events upon ϕ/ϕ_{LBO} for three thresholding levels of 0.86σ, 1.02σ and 1.21σ.

As expected, the number and duration of events increased as the non-premixed combustor was brought to blowout. The effect of the threshold level on the blowout proximity measure is shown in Figure 44. With increasing threshold level, there are fewer events detected and no events are detected until the system is very close to blowout. In contrast, at low threshold levels, the number and duration of the alarms close to blowout is much higher, however, events are detected at equivalence ratios much farther from blowout. The tradeoffs seen for the case of the atmospheric burner in Figure 31 were also seen in the non-premixed burner.

The threshold levels chosen for the thresholding based approaches are significantly different for the three burners described in this chapter. This may be due to the different sensors used, operating pressures or combustor geometry which can affect the acoustic

measurements significantly. However, it must be noted that the piezoelectric transducer was successfully used to detect precursors to blowout in the high pressure combustor even though it had extremely low sensitivity. This has huge industrial applications in engine health monitoring as it can be incorporated into already existing combustion hardware like fuel injectors or igniters.

To conclude, three different swirl combustors were studied and the blowout characteristics were found to be very similar. The combustors were brought to blowout by decreasing the overall fuel flow rate, while keeping the airflow fixed. The overall acoustic power decreased as blowout was approached due to the reduced heat release, unlike the case of the piloted burner, where the equivalence ratio was fixed and blowout was attained by reducing the pilot fuel flow rate. Bursts were found in the acoustic signal of the three swirl burners, which coincided with extinction/re-ignition events seen in the high speed video images. These events increased in number and duration close to blowout. The enhanced low frequency acoustics appeared to be controlled by the time interval between events and the duration of the events. A variety of spectral, wavelet and thresholding based approaches were developed to detect precursors to blowout.

CHAPTER 6

BLUFF BODY BURNER STUDIES

This chapter presents experimental results from a premixed bluff body burner under lean blowout conditions. This chapter characterizes the underlying flame dynamics near blowout in greater detail and relates it to the observed acoustic emissions. In this chapter, we focus on what is actually happening to the flame close to blowout. It was decided to focus this detailed analysis on the bluff body burner, because changes in the flame dynamics can be easily visualized by 2-D imaging techniques. It is divided into three sections. The first section characterizes the flame front dynamics as blowout is approached and focuses on the role of vorticity and flame stretch. The second section deals with the flame front statistics, which aid in understanding the observed acoustic measurements described in the third section.

6.1 Flame dynamics

Experiments were performed using the bluff body burner shown in Figure 10 (Section 3.1.3). Measurements from this combustor were taken at atmospheric conditions at a bulk average velocity of 1.2 m/s (centerline velocity of 1.8 m/s) at the burner exit, which correspond to a Reynolds number, Re_D=640. Once the bluff body flame is ignited and stabilized, its proximity to blowout was controlled by decreasing the overall fuel flow

rate while keeping the air flow rate fixed. The equivalence ratio was varied from 0.8 to its blowout value at 0.59.

The importance of fluid mechanics, especially flow vorticity, in flame stabilization has been discussed in Section 2.3. This section presents the vorticity dynamics of the flow (obtained from PIV) in conjunction with high-speed laser sheet images of the bluff body flame, which will help to better understand the acoustic observations described in the last section.

6.1.1 Role of vorticity

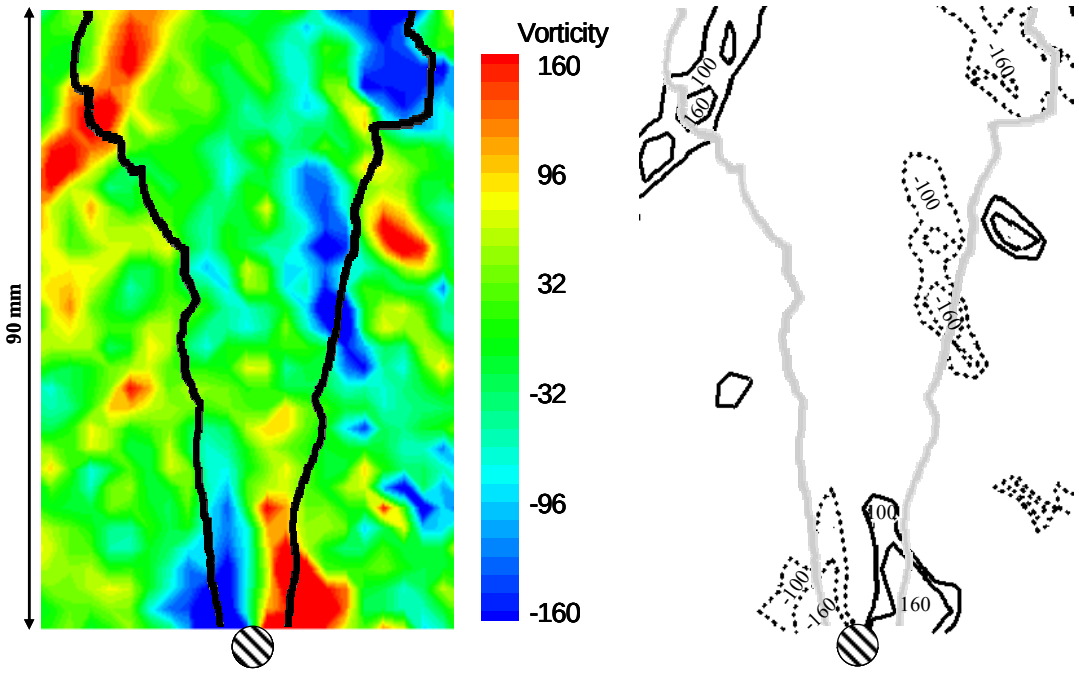

Figure 45: Instantaneous vorticity contour along with color map (left) and flame front edge (black solid line); and (right) vorticity contour (solid line-positive vorticity, dashed line-negative vorticity) along with flame front edge (gray solid line) of a stable flame at ϕ=0.72 (Flow direction is from bottom to top).

A typical image of the flame and 2-D vorticity field for a well-stabilized flame is shown in Figure 45 (left), with red and blue isoplots indicating positive and negative

vorticity respectively. Note the roughly symmetric flame wrinkles spaced at irregular intervals that convect downstream. Note also that the vorticity field does not exhibit the spatially periodic distribution of alternately signed vorticity, evidenced in non-reacting flows (see Figure 7). The bluff body wall generated vorticity is concentrated near the base and decreases in magnitude with downstream distance. Its magnitude decreases due to the flame generated baroclinic vorticity, of the opposite sign, which progressively weakens the wall-generated vorticity until it is completely gone. This point is quite evident from the colored isoplots shown in Figure 45 (left), shown in Figure 45 (right). Other representative cases are shown in Appendix C.

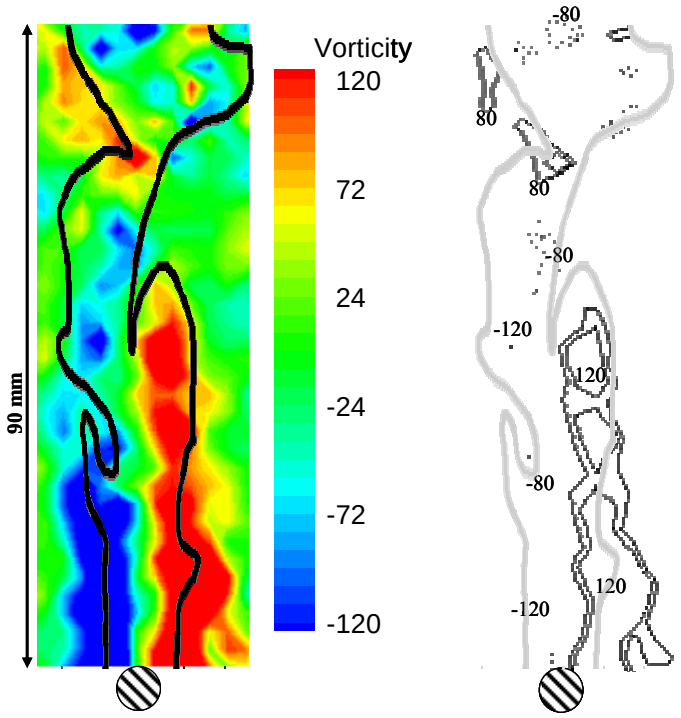

Figure 46: Instantaneous vorticity contour along with color map (left) and flame front edge (black solid line); and (right) vorticity contour (solid line-positive vorticity, dashed line-negative vorticity) along with flame front edge (gray solid line) of a flame close to blowout at ϕ=0.63 (Flow direction is from bottom to top).

Similar vorticity plots of a case close to blowout are shown in Figure 46. The bluff body wall generated vorticity in this case is also concentrated near the base and decreases in magnitude with downstream distance. However, smaller broken pockets of high vorticity can be found downstream in the instantaneous images. It is quite evident that the flame generated baroclinic vorticity of the opposite sign has a much smaller effect in the far field of the bluff body compared to the case of the stable flame. As the equivalence ratio decreases, the magnitude of the flame generated vorticity source term decreases, due to the decreasing density jump across the flame. This necessarily means that the flame near the bluff body experiences a higher magnitude vorticity field that persists farther downstream, due to the bluff body generated shear.

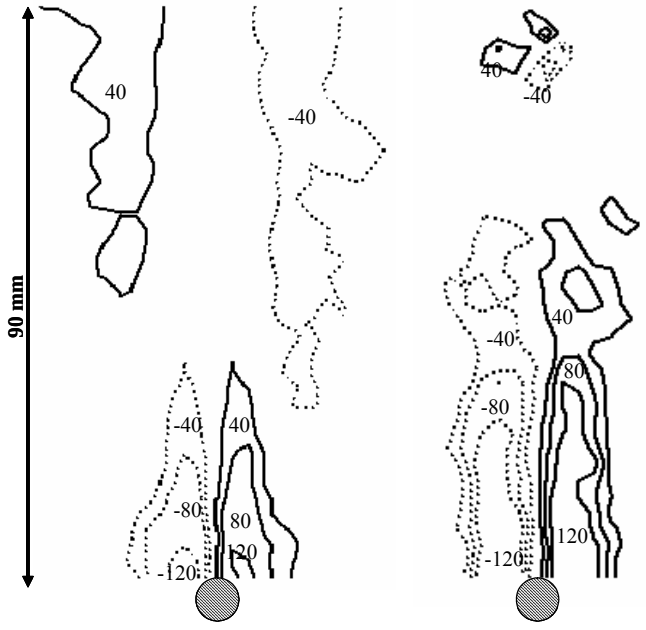

Figure 47: Average vorticity contour (solid line-positive vorticity, dashed line-negative vorticity) of a stable flame (left) at ϕ=0.72, and of a flame close to blowout at ϕ=0.63 (Flow direction is from bottom to top).

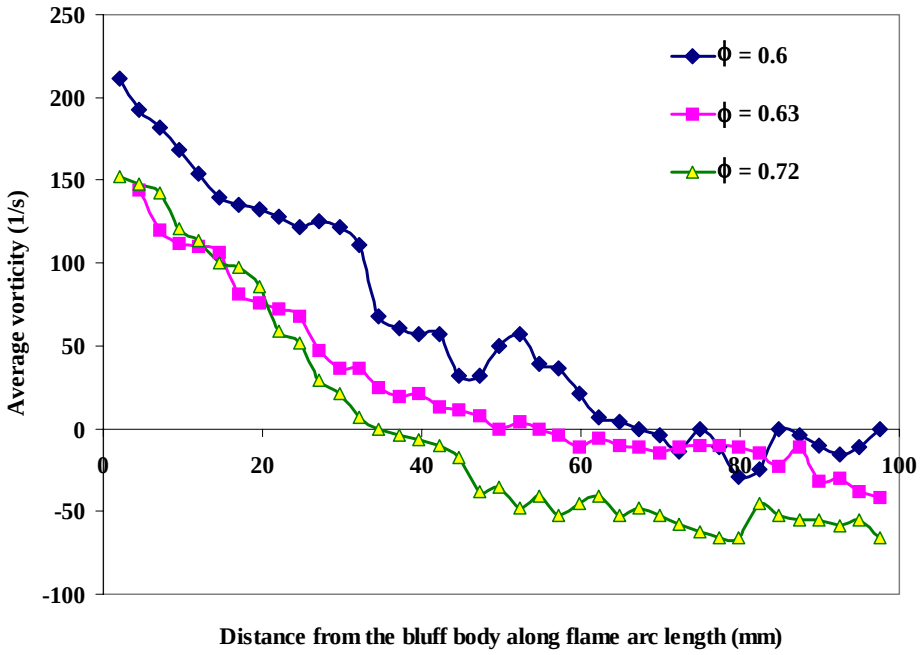

Figure 48: Dependence of average vorticity as a function of distance from the bluff body along the flame arc length for ϕ=0.72, 0.63 and 0.6.

The average vorticity field of a stable flame and a flame close to blowout is shown in Figure 47. These average plots have been obtained over 100 and 20 images for the case of a stable flame and a flame close to blowout respectively. Note that the wall generated vorticity effects have progressed further downstream as blowout is approached, as expected from abovementioned arguments. Note also the clear switch in sign of the average vorticity field with axial location, with a direction corresponding to that of the flame generated vorticity, for the stable flame case. There is hardly any significant average vorticity in the far field of the flameholder close to blowout compared to the stable case. This could be due to the cancellation of the relatively smaller magnitudes of flame and wall generated vorticity components at the flameholder far field. These features are clearly seen in Figure 48, which plots the average vorticity as a function of

distance from the bluff body along the flame arc length for ϕ= 0.72, 0.63 and 0.6. The average vorticity decreases with increasing axial distance for all cases and at some point, switches sign from positive (bluff body generated vorticity) to negative (flame generated vorticity). As the equivalence ratio is reduced, the effects of average bluff body generated vorticity have progressed further downstream. The average flame generated vorticity is nearly negligible very close to blowout.

6.1.2 Flame stretch effects

The flame near the bluff body has been shown to experience higher vorticity magnitudes as the equivalence ratio decreases. As such, the flame sees a higher fluid mechanic stretch.[94] Furthermore, the flame is also more vulnerable to stretch, as its extinction stretch rate decreases with equivalence ratio.[95, 96] This section quantifies the flame stretch as blowout is approached. As will be shown, localized flame extinction by flame stretch plays a key in its near blowout characteristics.

The 2-D flame stretch rate was quantified using the relations:

$$\kappa = \kappa_s + \kappa_c$$
$$\kappa_s = -n_x \times n_y \times \left(\frac{\partial u}{\partial y} + \frac{\partial v}{\partial x}\right) + (1 - n_x{}^2) \times \frac{\partial u}{\partial x} + (1 - n_y{}^2) \times \frac{\partial v}{\partial y} \quad (10);$$
$$\kappa_c = S_L / R_c$$

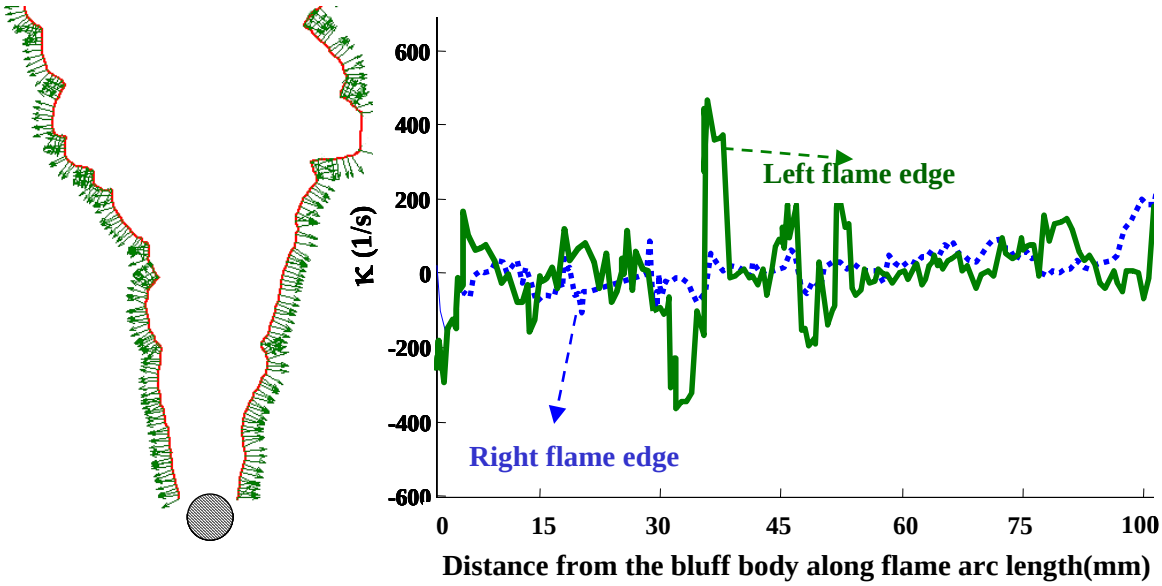

Figure 49: Extracted flame edge (left) along with flame normals (pointing towards the unburnt mixture); and variation of the measured flame stretch rate upon the distance from the bluff body at ϕ=0.7.

The flame speed, S_L, was obtained from Andrews et al.[97] The flame edge was extracted and spline fit from the instantaneous PIV images by demarcating the regions of high and low seeded flow, as explained in Section 3.2.4. The flame normals and curvatures are then computed at every location and used in conjunction with the measured flow field to determine the component of κ in the 2-D field of view. An example of this methodology is shown in Figure 49 for a stable flame, ϕ=0.7. As shown in the figure, the flame normals are pointing from the burnt to unburnt region. The velocity gradients in the x and y direction are calculated using the Matlab command "*gradient*". The variation of the measured stretch rates on distance from bluff body for this example is also shown in Figure 49 (right) for the left and right flame edges.

Although the third, unresolved dimension will cause the actual strain rate to be larger than that calculated here, it is probably not significant, as the flow field is strongly two-

dimensional. However, very close to blowout, the flame does have some three-dimensional features, as can be seen by the cross stream visualization in Figure 50, obtained by rotating the laser sheet by 90 degrees. The images were obtained at equivalence ratios of 0.7, 0.63 and 0.6. These top-view images of the flame suggest that the flame front curls up at either ends of the bluff body very close to blowout. However, on an average, the flow and flame field, especially at the bluff body centerline, are strongly two-dimensional.

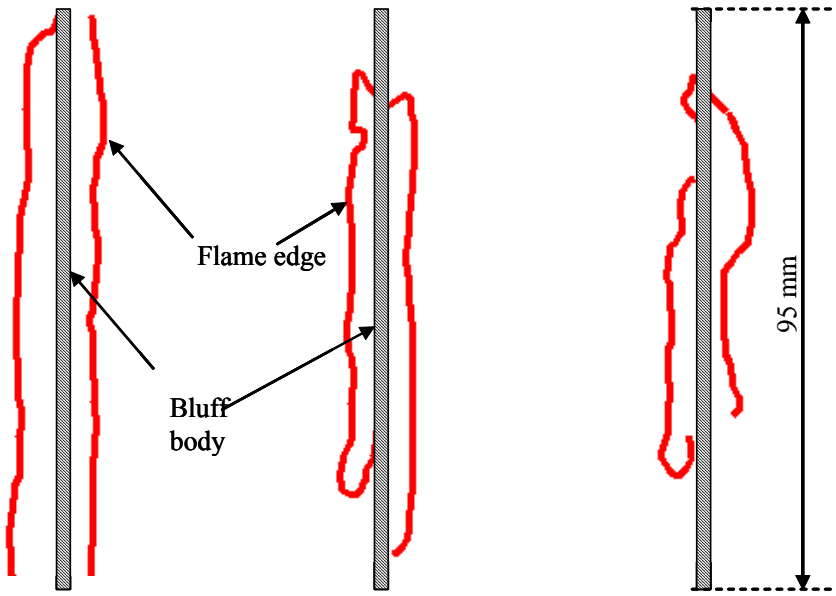

Figure 50: Span wise variation of the flame front corrugation for ϕ/ϕ_{LBO}=0.7 (left), 0.63 (center) and 0.6 (right). Flow direction is normal to the plane of the paper, towards the reader.

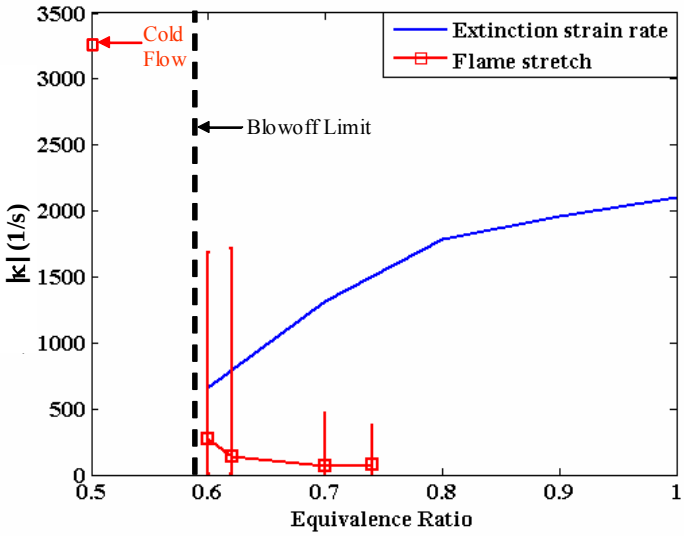

Figure 51: Dependence of flame stretch rate (measured) and extinction stretch rate (calculated) upon equivalence ratio. Bars denote fluctuations in the flame stretch rates observed from twenty images.

The dependence of the extinction strain rates and actual strain rates experienced by the flame upon equivalence ratio are plotted in Figure 51. The strain rate statistics quoted in this figure were obtained from twenty images using data obtained from a rectangular flow region located between two and four bluff body diameters downstream. The extinction stretch rate was estimated using the OPPDIF program in CHEMKIN, using GRI 3.0 and assuming a methane/air flame at 298 K and 101.3 kPa reactants. The opposing trends of the stretch rates that the flame sees, and those that it is capable of withstanding before extinction, is clear. The vertical bars in the stretch rates do not signify uncertainty in the measurement, but rather the range in instantaneous values that the flame sees (over the twenty images that were analyzed). Note the increasing magnitude of strain rate fluctuations with decreases in equivalence ratio, a point that will be discussed further below.

For comparison, the stretch rate for the cold flow case is also plotted; note the substantially larger value of mean stretch rate, almost six times larger, in the absence of combustion. Clearly, this value should only be interpreted for its comparative purposes, as there is no flame in this case. This value was estimated from cold flow velocity measurements at a spatial location coinciding with the average flame location. This comparison clearly shows the suppressed levels of vorticity in the reacting case due to gas expansion and baroclinic vorticity production.

Below some equivalence ratio, Figure 51 shows that the local, instantaneous stretch rate exceeds the extinction stretch rate for certain instants of time, although not always. This is apparently the reason for the appearance of local points of extinction, "holes", in the flame which are observed to first occur below an equivalence ratio of ϕ=0.65; see Figure 52. This sequence of consecutive images, spaced 10 ms apart, show the initiation of the hole, its convection downstream and impact upon the flame topology, and the re-closing of the flame hole by re-ignition. This phenomenon necessarily introduces some degree of unsteadiness in the flame – both in its position and in its total heat release. The unsteadiness in flame position is examined in detail in Section 6.2. The change in total heat release is studied by monitoring the sound generated by the flame under such conditions and will be further explained in Section 6.3.

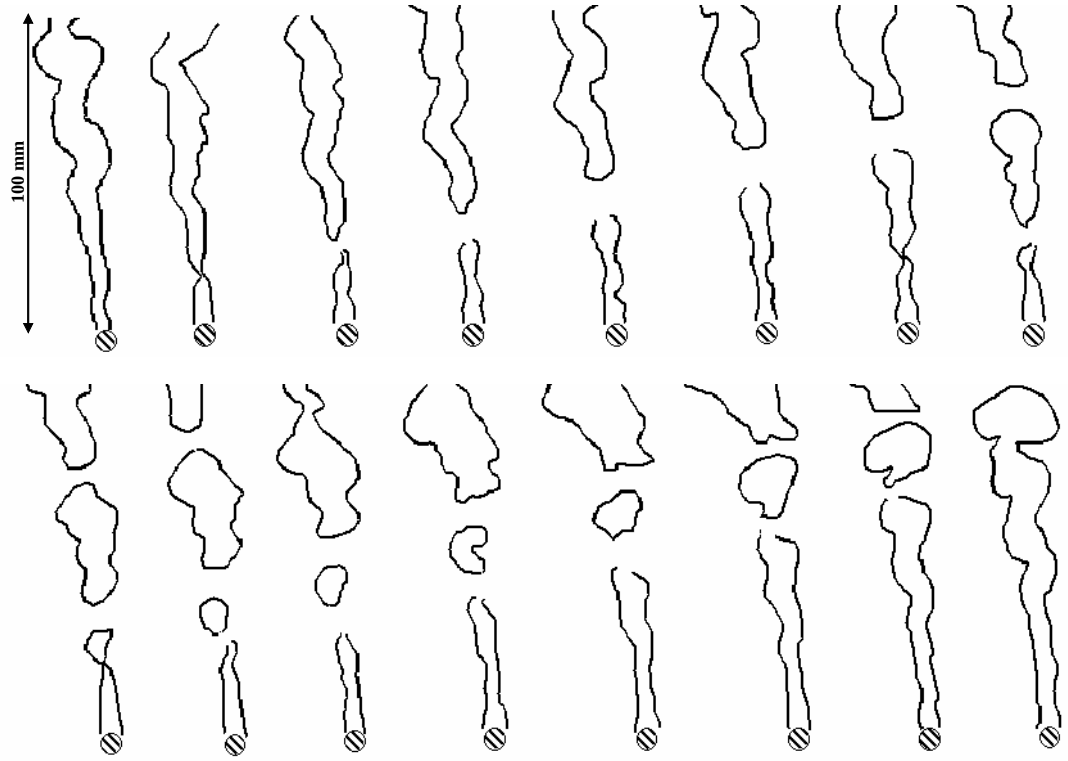

Figure 52: Sequence of flame images, 10ms apart, taken during the first pre-blowoff stage at ϕ=0.65. Note presence of flame holes in the images (Flow direction is from bottom to top).

These local flame extinction events, followed by flame recovery, are manifestations of the first of two stages in the unsteadiness experienced by near blowoff flames. It should be emphasized that under such conditions the flame can apparently persist indefinitely and is simply unsteady. Moreover, the overall position and qualitative dynamics of the flame, in the instances where it is continuous, appear essentially the same as that of the flame under stable conditions.

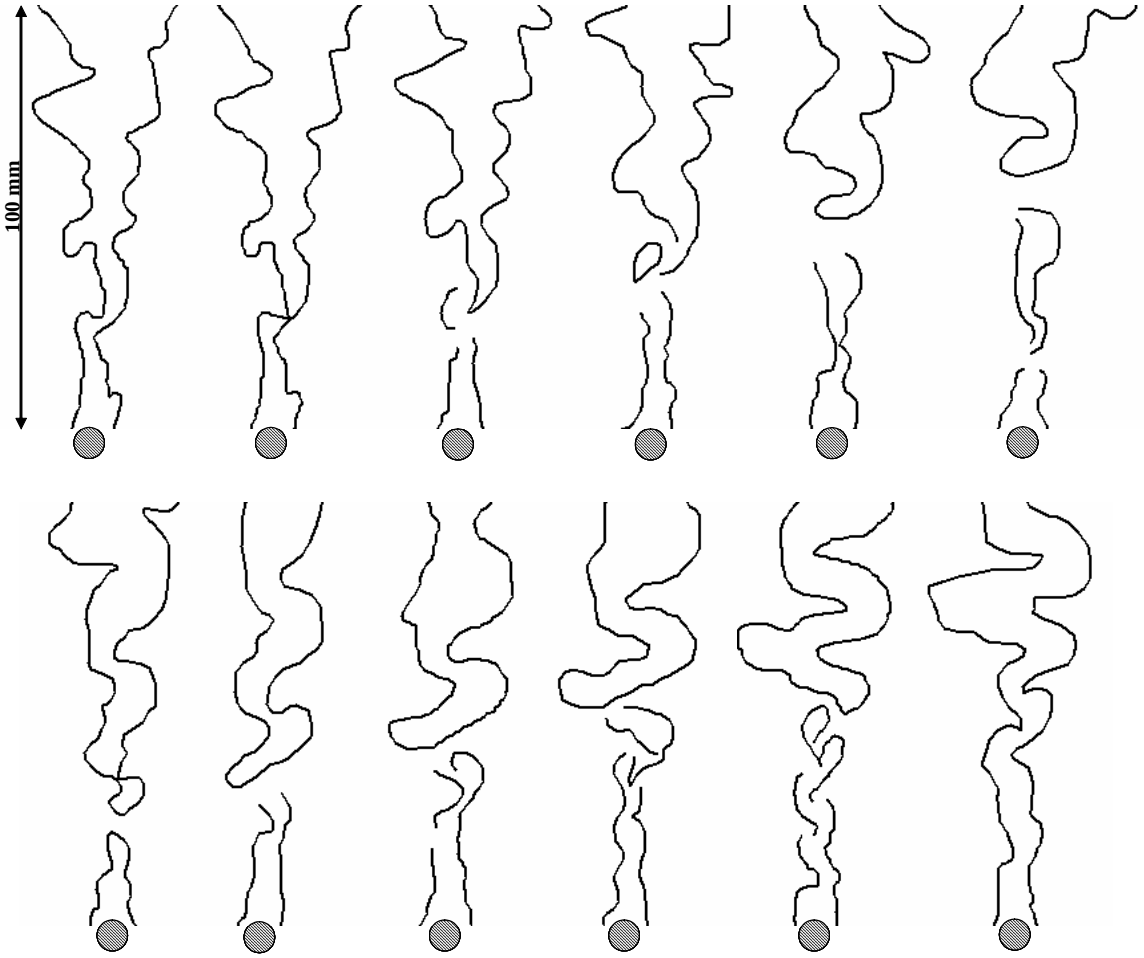

Figure 53: Sequence of flame images, 6 ms apart, taken during the second pre-blowoff stage at ϕ=0.6 (Flow direction is from bottom to top).

As the equivalence ratio is further decreased, the duration for recovery of the flame from each local flame extinction event is observed to increase monotonically. For example, the fraction of images with localized extinction events present increases from 0% at ϕ=0.66, to 8% at ϕ=0.64, to 40% at ϕ=0.6. It should be emphasized that the composition and temperature of the wake is locally altered with each occurrence of local flame extinction, as some portions of the wake may no longer consist of simply hot re-circulating products, but also cold reactants.

Eventually, around an equivalence ratio of 0.62, these extinction events result in large-scale alterations of the wake dynamics, such as shown in Figure 53. This is the second stage of the flame unsteadiness experienced prior to blowoff. As illustrated in the figures, the overall dynamics of the flow field is clearly altered; in many cases the flow very near the bluff body bears striking resemblance to the asymmetric Von-Karman type flow field[ii] (as manifested in the flame sheet). In fact, the flame quenching inside what appears to be a series of large scale structures is clearly evident in several of these images. However, it should be emphasized that the flow field and flame position is much more disorganized than that of cold-flow Von Karman vortex shedding. It reverts back and forth between synchronized, symmetric wrinkles on opposite sides of the bluff body, to asymmetric wrinkles, and to what appears to be independent, asynchronous flame front distortions. Estimates from our data suggest that the time scales of these observed coherent structures are of the order of 13-20 ms, corresponding to Strouhal number, St= 0.26-0.39 (using centerline velocity of 1.8m/s). These estimates were obtained by calculating the distance between subsequent "structures" in the flame images, shown in Figure 53. The proximity of this range to the St~0.21 value observed in the non-reacting case suggests that there may be some similarities to the flow dynamics in these two instances, but further analysis is needed to make a more confident assertion.

The initiation of this second stage has two consequences – first it increases the overall unsteadiness of the flow field. This is quantified in Figure 51, which plots the large strain rate fluctuations at these low equivalence ratios. In addition, it is visually very obvious from the images, as the flame flaps back and forth much more violently. This second

[ii] This asymmetric flapping of the flame, reminiscent of the Von-Karman vortex shedding pattern is also observed in flames under stable conditions, but only very far downstream; e.g., see Figure 52.

stage apparently coincides with the observations of Nicholson and Field[36] and the coherent structures observed just prior to blowoff by Hertzberg et al.[25].

The second consequence of the initiation of this stage is that it increases the magnitude of the curvature contribution to the stretch term, κ_c, see Eq. (7). In the first stage, the average value of $|\kappa_c|$ was usually comparable to the average hydrodynamic stretch term, $|\kappa_s|$, in the region near the bluff body, as shown in Figure 54. The figure plots the dependence of the flame stretch rates due to strain and curvature upon equivalence ratio, and the vertical bars signify the range of instantaneous values. In the second stage, this curvature term is often dominant due to the sharp kinks developed by the flame in the bluff body near field, due to its large-scale distortions. This is seen in Figure 54 as the large instantaneous value of stretch rates due to curvature. An example of this fact is shown in Figure 55, where the right half of a flame close to blowout at ϕ=0.6 is plotted. The co-ordinate '*s*' is along the arc length of the flame. Also plotted is the dependence of the measured flame strain rate due to curvature, κ_c along the arc length of the flame. Four points are numbered along the flame and the value of κ_c at those corresponding points can be compared. Sharp spikes in the value of κ_c are clearly seen at location of sharp kinks. In fact, extinction of the flame is plainly visible in these sharp kinks in some images. Additional representative cases similar to Figure 52 and Figure 53 are shown in Appendix C. Note that the average hydrodynamic stretch term, $|\kappa_s|$ increases monotonically as blowout is approached. This term may be responsible for the inception of the flame hole during the first stage, when the flame appears to be devoid of any large scale distortions or kinks and seems to persist indefinitely without blowing out.

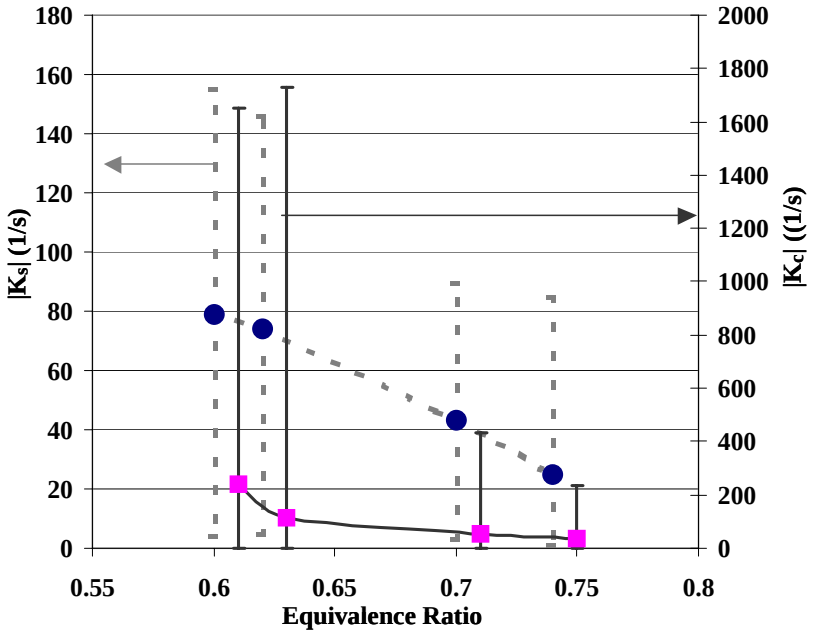

Figure 54: Dependence of flame stretch rate due to strain, κ_s, (dashed grey line) and curvature (solid black line, shifted to the right for clarity) upon equivalence ratio. Bars denote fluctuations in the flame stretch rates observed from twenty images.

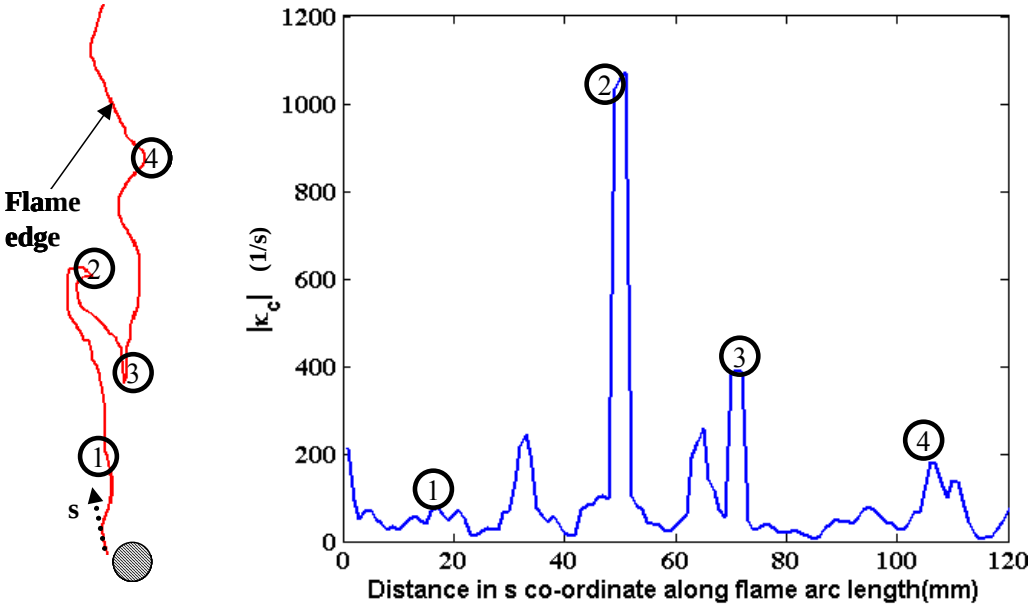

Figure 55: Extracted image (only right half shown) of a flame at ϕ=0.6 (flow direction is from bottom to top); and the dependence of the measured flame strain rate due to curvature, κ_c along the flame arc length.

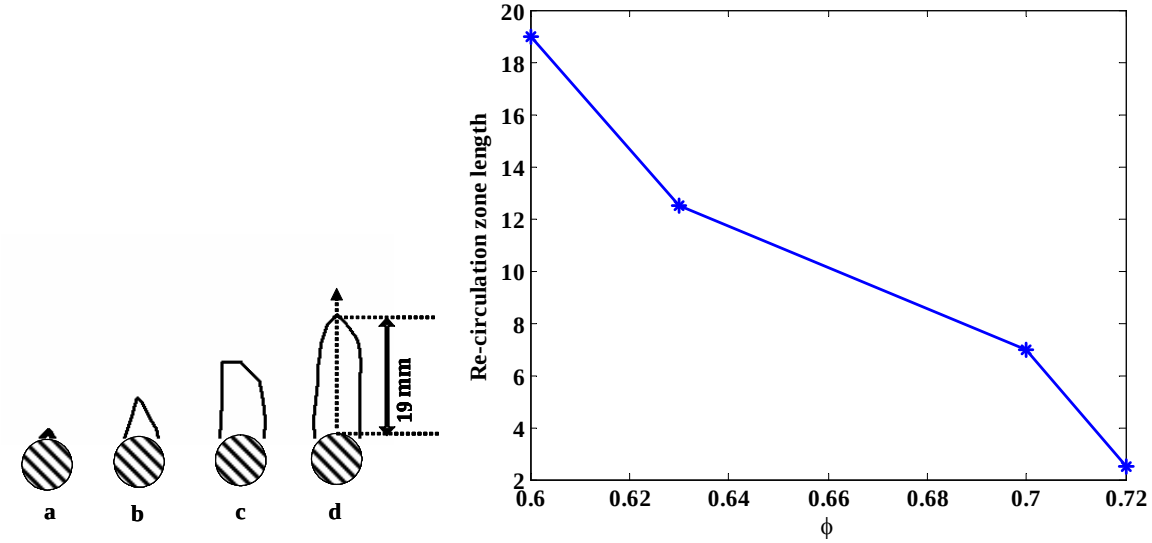

Figure 56: Average zero velocity contours (left) plotted for flames at ϕ= a) 0.72, b) 0.7, c) 0.63 and d) 0.6; and the dependence of the length of the re-circulation zone upon equivalence ratio.

A final word on the actual blowoff event. Figure 51 suggests that blowoff does not coincide with the point where the average flow strain rate equals the extinction strain rate, as the flame blows off much earlier. As such, blo*woff must be precipitated by a time-localized extinction event*, which is of large enough scale to cause irrecoverable blowoff. It is likely that initiation of this second stage is ultimately responsible for blowoff, as blowoff occurs at just a slightly lower equivalence ratio (ϕ=0.59) than where this second stage initiates (ϕ~0.62). Perhaps one of the flame extinction events occurring in this second stage introduces a slug of unreacted mixture into the re-circulation zone, which fails to ignite the incoming mixture, resulting in blowoff. This explanation can be seen to have many corollaries to the interpretation of Zukoski[35](explained in Section 2.3), according to which, flame extinction occurs when the fresh mixture does not spend

enough time in the shear layer to be ignited by the hot re-circulation zone. He defined a critical blowout time (see Equation 4), $t_{BO.} = D_r / V_{BO}$. To get a measure of this time scale, the length of the re-circulation zone must be ascertained. The length of the re-circulation zone can be ascertained to be the distance from the bluff body to the point of zero velocity (obtained from PIV) along the vertical line through the centerline of the bluff body, as shown in Figure 56. From Figure 56, the length of re-circulation zone of the stable flame and the flame close to blowout can be observed to be 2 and 19 mm respectively. Therefore, as equivalence ratio is reduced, the length of the re-circulation zone increases, thus delaying the feedback of heat and radicals to the fresh mixture. For the calculation of t_{BO}, the length of the re-circulation zone close to blowout must be used. The maximum velocity the flow field of a lean bluff body flame sees is typically around 2.5 m/s (obtained from PIV) within 20 mm from the bluff body. Therefore, t_{BO} can be calculated to be ~ 8 ms. According to Zukoski[35], as long as the feedback time in the re-circulation zone is less than 8 ms, the flame can be recovered after a local flame loss.

The present study has improved on the above analysis, with the key addition coming from an emphasis of the role of unsteady strain and fluid dynamics on the flame.

6.2 Flame front statistics

High-speed flame visualizations in the previous section have shown the erratic presence of symmetric and asymmetric wrinkling of the flame front. These “wrinkled” flow structures are continuously being generated and propagated in the mean flow direction. The amplitude of these fluctuations vary with height, due to the growth and decay of the underlying flow structures, and due to the competing vorticity sources as well as the propagation of the flame, which tends to smooth out the wrinkles. The focus

of this section is to study these flame front fluctuations in detail and relate it to the flame acoustics explained in the next section. Figure 57 (left) shows an extracted image of a bluff body flame at ϕ=0.7 (ϕ/ϕ_{LBO} = 1.19). These images are post-processed to determine the temporal location of the left and right flame branches as a function of height using the flame edge-tracking algorithm, explained in Section 3.2.4. The coordinate system is shown in Figure 57 (left), where the (x,y)=(0,0) point is chosen as the top of the bluff body centerline. Thus we obtain the flame location, $L(y,t)$ at each time instant, t, and each spatial location, y from the bluff body. The mean value of L at each y location is subtracted to get a flame front perturbation value, $L'(y,t)=L(y,t) - \langle L(y) \rangle$. The time traces of the instantaneous location, $L(y,t)$, of the left and right branches of the flame front at a distance 94mm from the bluff body are also shown in Figure 57 (right).

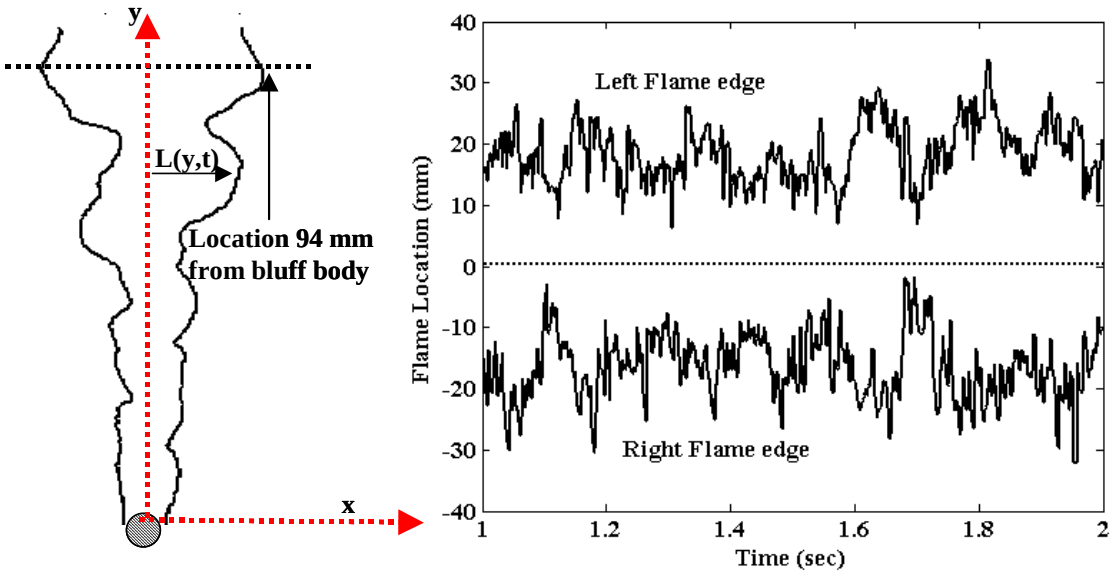

Figure 57: High-speed video image of a bluff body flame at ϕ/ϕ_{LBO} = 1.19 (left) and the time series of the flame edge at a location 94mm from the bluff body (right).

This time series signal is first analyzed to determine the spectral content of the flame front position using the Fourier transform to yield $L'(y, f)$. A typical flame front position spectrum of a bluff body flame at ϕ=0.7 (ϕ/ϕ_{LBO} = 1.19) is shown in Figure 58 for four different flame locations of 64, 74, 84 and 94 mm from the bluff body. There is not much spectral activity beyond 100 Hz and the spectra decreases monotonically with decreasing height with a broad peak at ~45 Hz, corresponding to Strouhal number, St= 0.24 (using centerline velocity of 1.8m/s). This Strouhal number is what we would expect from the Von Karman type vortex-shedding phenomenon. The trends do not vary much for other equivalence ratios, but the values are slightly higher for the case close to blowout. As will be shown in the next section, the flame front fluctuations play a great role in the measured acoustic noise, which also show similar increased spectral activity below 100Hz.

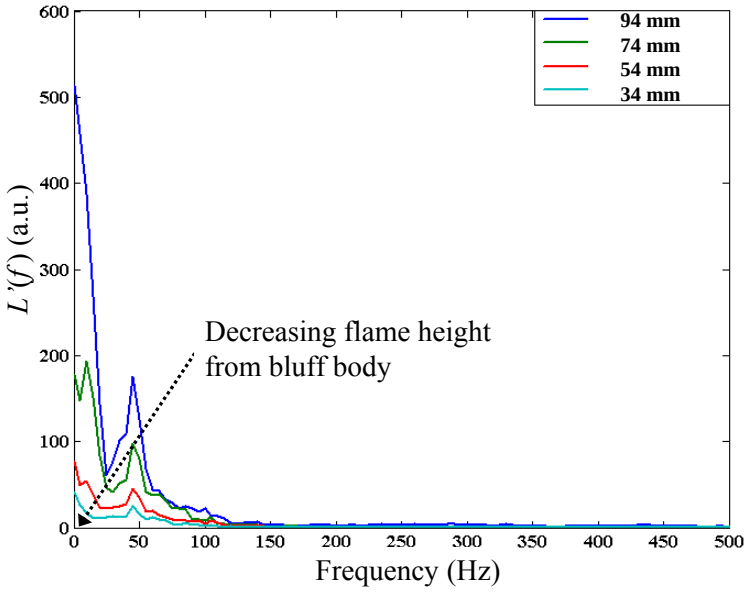

Figure 58: Typical spectra of flame front fluctuations at a location of 64, 74, 84 and 94 mm from the bluff body at ϕ/ϕ_{LBO} = 1.19.

The time traces of the instantaneous location, $L(y,t)$, is further analyzed to determine the relationship between the dynamics of both branches of the flame at various spatial locations, 'y', from the bluff body. For example, by analyzing the correlation between the positions of the two flame branches at a given height, their degree of interaction can be inferred; e.g., correlations approaching +1 and -1 will imply symmetric and asymmetric flame sheet dynamics, while correlations approaching 0 will imply that the two flame sheets have independent dynamics. This is shown in Figure 59, where the cross correlation coefficient between the left and the right flame edges upon distance from bluff body, y, at various equivalence ratios are plotted. The figure shows that the correlation between the left and right flame branches drops as equivalence ratio is reduced for y below 60 mm.

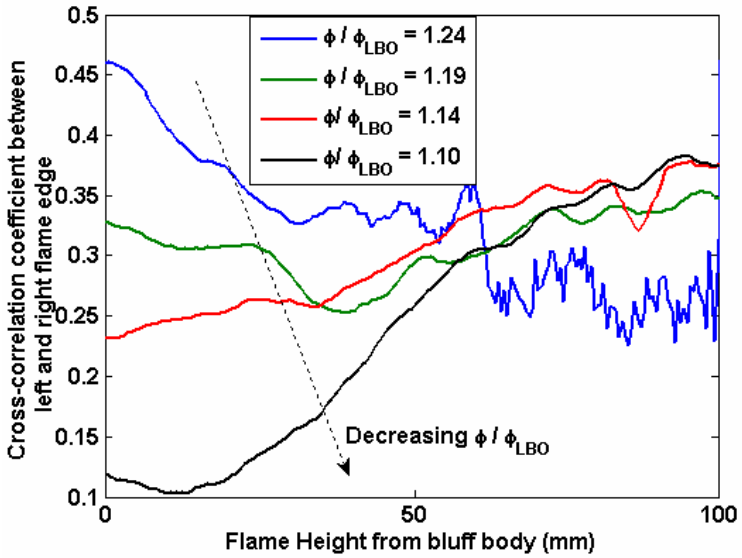

Figure 59: Cross correlation coefficient calculated between the right and left flame edge location, $L'(y,t)$, for ϕ/ϕ_{LBO} = 1.24, 1.19, 1.14 and 1.1 versus spatial location from bluff body.

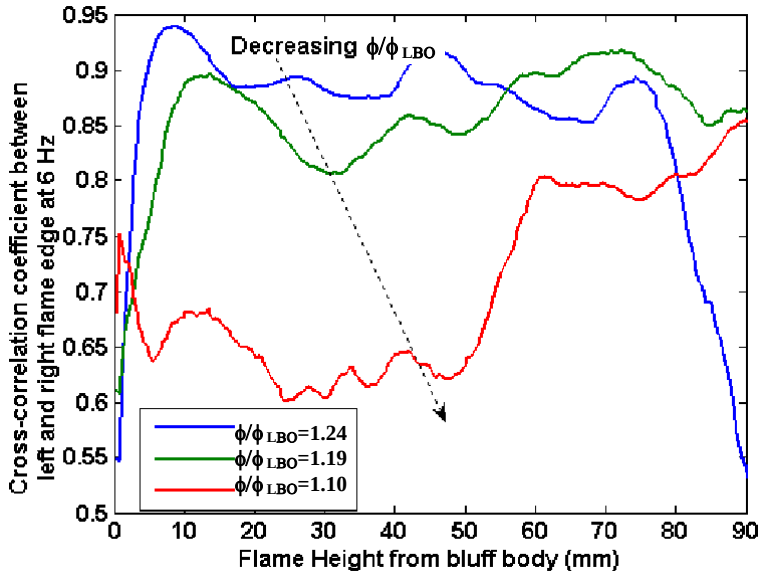

Figure 60: Cross correlation coefficient calculated between the right and left flame edge location, $L'(y,t)$, at 6 Hz for ϕ/ϕ_{LBO} = 1.24, 1.19 and 1.1 versus spatial location from bluff body.

The correlation between the flame branches at different frequencies can be quantified via the coherence. An example is shown in Figure 60 for a frequency of 6 Hz at different equivalence ratios. The figure shows high correlation between left and right flame edges at 6 Hz. The values decrease as blowout is approached. These trends vary with frequency but the best correlations are seen for frequencies below 15 Hz.

6.3 Acoustic Studies

Next, we look at flame acoustics near blowout. As blowout is approached, the phenomenon of flame hole initiation and recovery (seen in Figure 52) introduces some degree of unsteadiness in the flame and its total heat release. This is manifested in the acoustic signature by a short duration reduction in R.M.S. pressure. An example is shown in Figure 61, which illustrates the case of a flame near blowout (ϕ=0.62). Simultaneous

flame images and measured acoustic pressures are plotted. The temporal dependence of a 10 ms moving average estimate of the pressure variance is also plotted. There is a drop in the pressure variance during the large extinction event, followed by a sharp rise, as the flame reappears.

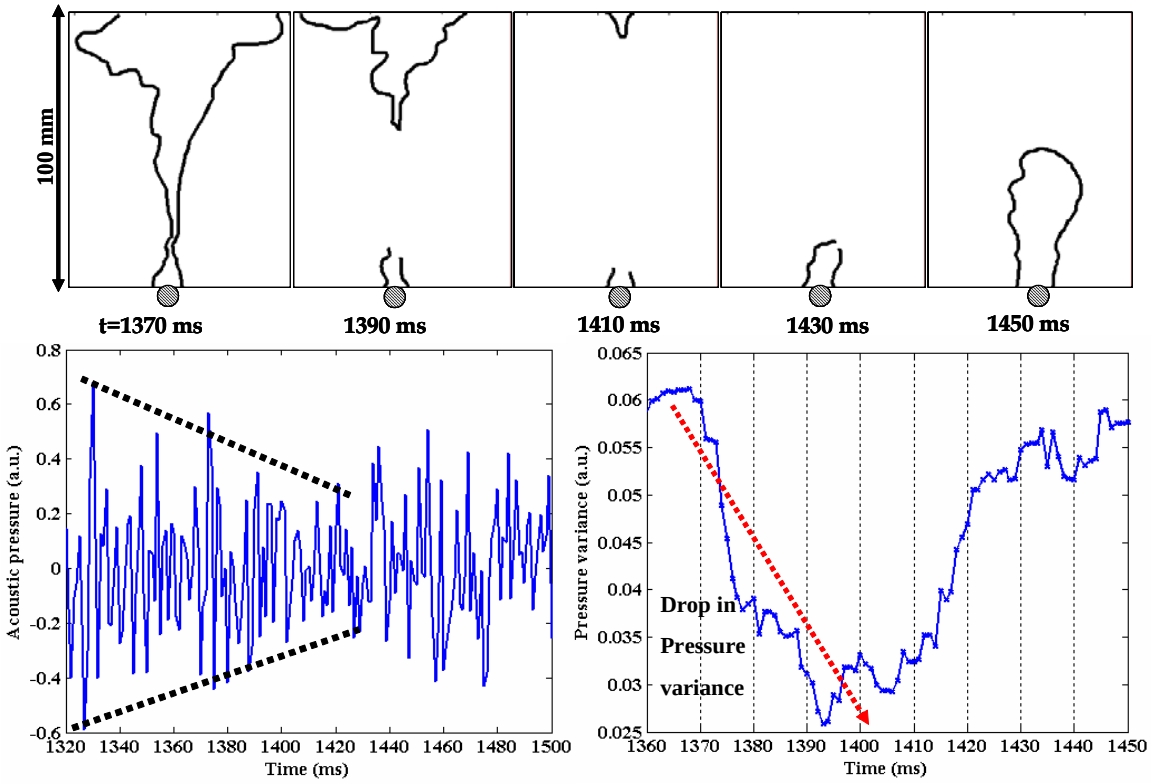

Figure 61: High-speed video images (top) of a "near blowout" flame and its corresponding acoustic pressure and its variance (calculated over a time of 10ms) plotted versus time (bottom) at ϕ=0.62.

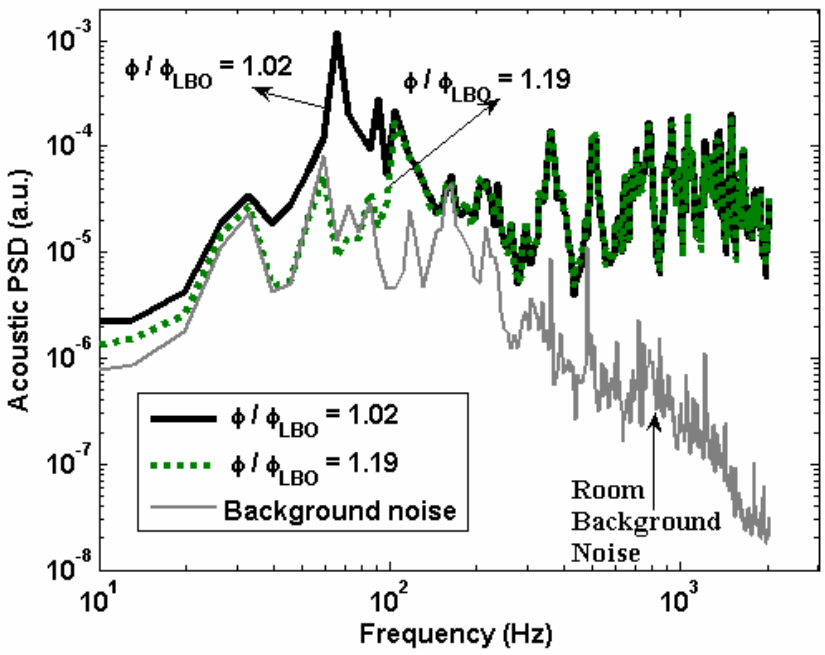

Figure 62: Acoustic spectra from the bluff body burner for ϕ/ϕ_{LBO} = 1.19 and 1.02, along with background noise.

Next, the acoustic spectrum of the flame is plotted in Figure 62. The equivalence ratio is normalized by its value at blowout (ϕ=0.59) to enable comparison across other burners. The combustion noise spectra of the burner at two different normalized equivalence ratios, ϕ/ϕ_{LBO} = 1.19 and 1.02 are plotted along with background noise. As the equivalence ratio is reduced, the spectral component in the 40–100 Hz range increases slightly until ϕ/ϕ_{LBO} = 1.02, where there is an abrupt increase. The spectra has a broad peak at ~65 Hz, corresponding to Strouhal number, St= 0.34 (using centerline velocity of 1.8m/s). The signal to background noise ratio for this burner is poor below 40 Hz at these operating conditions. This can be improved by operating the combustor at much higher flow velocities, which is currently out of scope for the present work.

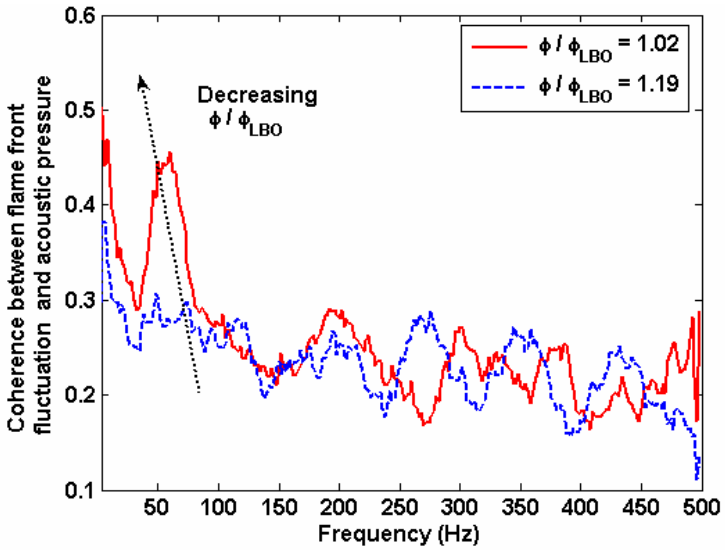

Figure 63: Coherence between flame front fluctuations and corresponding acoustic emissions at $\phi/\phi_{LBO} = 1.19$ and 1.02.

The acoustic spectra can be compared to the spectra of the flame front fluctuations at a distance of 94 mm from the bluff body, seen in Figure 58. Both spectra show increased spectral activity in the 40-100 Hz regime. The coherence between the flame branch fluctuation and its corresponding acoustic emission for two different normalized equivalence ratios, $\phi/\phi_{LBO} = 1.19$ and 1.02 is shown in Figure 63. There is a marked increase in the correlation between the flame front fluctuations and acoustic emissions below 100 Hz. The increase in the low frequency regime for the combustion noise very close to blowout can, therefore, be related to the large-scale flame front fluctuations. The abrupt increase in flame acoustics at 40-100 Hz very close to blowout (ϕ=0.6) clearly relates to the inception of the second stage and the presence of coherent structures seen in Figure 53. Estimates of the time scales of the observed coherent structures during stage two (discussed in Section 6.1) were found to correspond to St= 0.26-0.39. The proximity

of this range to the St~0.34 value observed in the acoustics suggests that the violent flapping of the flame front seen in the second stage is responsible for the increased low frequency acoustic oscillations of the time scales of the von Karman vortex shedding. Note that the flame front fluctuations which were multi-valued and had flame holes were avoided in this correlation.

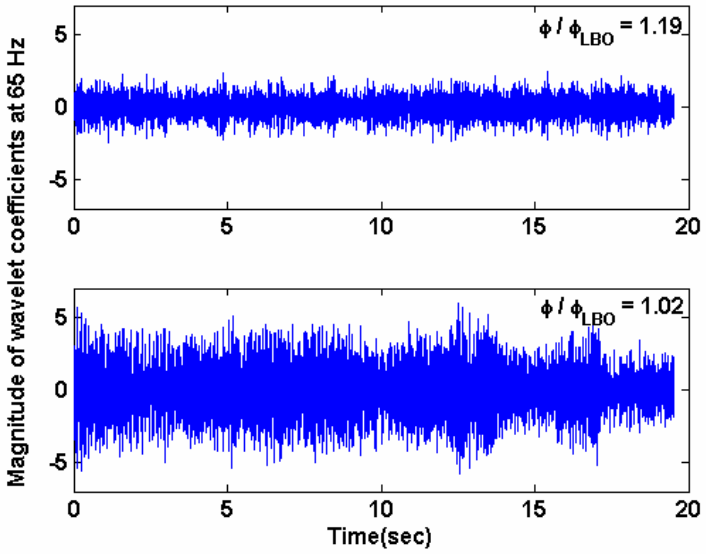

Figure 64: Time dependence of acoustic $W_2(t)$ wavelet coefficients at ψ = 1/65 seconds for ϕ/ϕ_{LBO} = 1.19 and 1.02.

Figure 64 plots the computed $W_2(t)$ wavelet coefficients at a scale of 65 Hz for different normalized equivalence ratios, ϕ/ϕ_{LBO} = 1.12 and 1.03. As the combustor approaches blowout, the wavelet-filtered variance increases very little until ϕ/ϕ_{LBO} = 1.02, where there is a considerable increase. This is similar to the abovementioned abrupt increase in the combustion noise spectra, seen in Figure 62. There is no evidence of

prominent large amplitude bursts in the wavelet-filtered signal as observed in the case of the swirl burners.

To conclude, bluff body stabilized flames pass through two distinct stages responsible for their unsteady behavior prior to blowoff. The first is associated with momentary strain levels that exceed the flame's extinction strain rate, leading to flame "holes". The second is due to large scale alteration of the fluid dynamics in the bluff body wake, leading to violent flapping of the flame front and even larger straining of the flame. This leads to low frequency acoustic oscillations of the time scales of the von Karman vortex shedding. This is manifested as an abrupt change in combustion noise spectra at 40-100 Hz very close to blowout. This behavior is captured in the wavelet-filtered data as well. The proximity of the bluff body burner to blowout can, therefore, be detected by monitoring the R.M.S pressure and the low frequency acoustic spectral power.

CHAPTER 7

CONCLUSIONS AND RECOMMENDATIONS

7.1 Conclusions of present work

The overall objective of this work was to characterize the blowout phenomenon and to develop a sensing methodology that can detect and assess the proximity of a combustor to blowout by monitoring its acoustic signature. This study employed burners with the three fundamentally different flame holding mechanisms: pilot flame, swirl and bluff body. Care was taken to avoid dynamic instabilities in these burners. The focus was primarily on the detection of the onset of loss of static stability. In general, the results show that the flames exhibited large-scale unsteadiness and/or increased presence of extinction and re-ignition events as blowout was approached. This generally resulted in an increase in the low frequency spectral activity in the combustion noise. A variety of spectral, wavelet and thresholding based approaches were used to detect precursors to blowout.

The first part of the work concentrated on understanding blowout phenomenon in a simple, atmospheric premixed piloted burner. As blowout was approached, the flame detached from one side of the burner and showed increased flame tip fluctuations close to

blowout. Combustion noise was found to be dominant in the 10-150 Hz frequency regime of the acoustic spectra, which was associated with the amplified flame tip undulations.

The next part of the study was focused on swirling combustion systems in non-anechoic environments. A fundamental, atmospheric swirl-dump combustor was studied first. The combustor was brought to blowout by decreasing the overall fuel flow rate, while keeping the air flow rate fixed. As blowout was approached, short, often spatially localized extinction/re-ignition events were observed in the high-speed video images. These events, manifested as bursts in the acoustic signal, increased in number and duration as the combustor approached blowout. An increase in 10-100 Hz frequency regime was observed in the combustion noise spectra, apparently controlled by the time interval between events and the duration of the events. These results were corroborated with OH* chemiluminescence measurements, which dropped to "near" zero values, indicating the occurrence of short duration, extinction events. This analysis was then applied to a high-pressure swirl combustor rig and, finally, to a non-premixed, swirl aircraft combustor simulator. The blowout phenomenology was found to be very similar for the three swirl combustors.

The third part of the study focused on the bluff body burner. It characterized the underlying flame dynamics near blowout in greater detail and related it to the observed acoustic emissions. It was decided to focus this detailed analysis on the bluff body burner, because changes in the flame dynamics could be easily visualized by 2-D imaging techniques. Laser sheet imaging and PIV was used to better understand the temporal dynamics of the flame sheet. Vorticity was found to play a significant role in the flame dynamics. The bluff body wall generated vorticity was observed to be concentrated near

the base and it decreased in magnitude with downstream distance. Its magnitude decreased due to the flame generated baroclinic vorticity, which was of the opposite sign. As blowout was approached, the magnitude of the flame generated vorticity decreased, due to the decreasing density jump across the flame.

The flame passed through two distinct stages prior to blowoff. The first was associated with momentary strain levels that exceed the flame's extinction strain rate, leading to flame "holes". The second was due to large scale alteration of the fluid dynamics in the bluff body wake, leading to violent flapping of the flame front and even larger straining of the flame. This led to low frequency acoustic oscillations of the time scales of the von Karman vortex shedding. This manifested as an abrupt increase in combustion noise spectra at 40-100 Hz very close to blowout. This present study has improved on the classic analysis by Zukoski[35], with the key addition coming from an emphasis of the role of unsteady strain and fluid dynamics on the flame.

The blowout characteristics of the confined burners like the swirl burners and the unconfined burners like the piloted and bluff body burners were observed to be different. Large scale, violent flame unsteadiness was clearly visible in the unconfined burners, which lead to low frequency acoustic oscillations. For the case of the confined swirl burners, the presence of extinction and re-ignition precursor events were universally observed. These events were found to increase in number and duration close to blowout. Wavelet and statistical techniques were found to be most useful for these burners, where the time-localized events in the signatures were more pronounced. In contrast, spectral approaches were sufficient for the piloted burner, where the overall "average" characteristics of the signal changed, to detect the onset of blowout.

7.2 Recommendations for future studies

The following recommendations discuss the various improvements to this study that will help gain more confidence in understanding the blowout phenomenon. There is a clear absence of models or theoretical analysis in this study. Unfortunately, this is beyond the scope of the present work. Computational efforts by Soteriou[68] at United Technologies have provided some validation to the role of vorticity in the flame dynamics. However, additional numerical work to study flame behavior close to blowout in greater detail is required.

The blowout phenomenology was determined for combustors with three different flame holding mechanisms. However, a complete parametric study of the phenomenology is warranted. For example, will the blowoff be different for a wedge flame holder? In this case, the approach flow cleanly divides around it and separates *at a well defined point*. With circular bodies, the separation point is Reynolds number dependent and subject to oscillation. It is likely, therefore, that the blowout flame dynamics are different for a wedge or conical flame holder. Similar studies must be examined for piloted burners of various diameters, swirl burners of varying swirl numbers etc. Also, tests should be performed over a range of axial flow velocities, air preheat temperatures, pressures, fuel compositions etc.

PIV was effectively used to calculate the flow and flame properties for the case of the bluff body burner. However, the spatial resolution of these measurements was limited to ~1 mm, which is of the order of flame thickness at stoichiometric equivalence ratios for a methane-air flame. In order to get better spatial resolution, micro-PIV can be employed. This will increase the accuracy of the flow measurements.

The blowout sensing methodologies developed in this study have been tested in a variety of fundamental premixed combustors with great success. They were also tested in high-pressure combustors and in a non-premixed aircraft combustor simulator. Some success was also achieved in integrating acoustic and optical sensing methodologies to increase robustness in detecting blowout. However, these approaches still warrant testing in realistic industrial or aircraft combustors.

APPENDIX A

PIV UNCERTAINTY ANALYSIS

PIV was used in measuring flow strain rates in the bluff body burner. This appendix is devoted to analyzing the contributing factors to uncertainty in the processing of PIV data[90]. The overall measurement accuracy in PIV is a combination of a variety of aspects extending from the recording process to the methods of evaluation. They can be classified as the following:

1. PIV system errors: These are related to the hardware of the PIV system, e.g. calibration errors, image aberrations, and tracking errors (particles not following the flow).

2. Truncation error: This is the error due to approximating the velocity with finite differences. This error is similar to the truncation error of a numerical analysis.

3. Detection error: This is the error due to not identifying the correct correlation peak in the correlation plane.

4. Precision error: This is due to inefficiencies of the sub-pixel interpolation.

The system errors are not considered in this appendix. The relative truncation error was shown by Boillot and Prasad[98] to be proportional to the time separation between the images, or equivalently to the particle displacement. An optimum time separation was chosen (100 μs) such that the truncation error is minimized, in addition to reducing out-

of-plane velocity components. The precision and detection errors are the main sources of error that are evaluated here.

The measurement uncertainty can be assessed in a variety of ways. One approach is to use actual PIV recordings for which the velocity data is known reliably. But this approach is often not feasible. An alternative and commonly used approach is based on Monte Carlo numerical simulations.[90,99] In these simulations, the seeding is assumed uniform and the particle images are assumed Gaussian.

The probability of a valid displacement detection increases when more particle image pairs enter the interrogation window. Measurement uncertainty decreases with the increase of the particle image density as more particle image pairs increase the signal strength of the correlation peak. The seeded particles may not follow the flow field due to sedimentation or Brownian motion, if the flow is not seeded adequately. If the flow is densely seeded, then both a high validation rate as well as a low measurement uncertainty can be achieved using small interrogation windows, which in turn allows for a high spatial resolution. As such, it is generally good to seed the flow with high particle image density. Care was taken to ensure that the seeding particle distribution was homogeneous and dense (10-15 particles per interrogation window). Increase in the background noise can also affect the measurement uncertainty. However, its effects on accuracy are minimal, since the noise is mostly uncorrelated.

The inefficiency of the sub-pixel interpolation in finding the correct peak position with sub-pixel accuracy is affected by many factors, such as noise in the images, non-uniform seeding, the size and shape of the particle images, velocity gradients and the interrogation algorithm. Using Monte Carlo simulations,[90] the uncertainty due to image

processing procedures is estimated to be a maximum of 4 pixels, which corresponds to 0.3 mm in the bluff body flow field. Thus, the error caused by image processing is a maximum of 1%. The interpolation error is determined by the grid size, the fluctuation of the velocity in the grid, and the velocity spatial gradient. The maximum possible error is the maximum fluctuation within the grid or the velocity gradient multiplied by grid size. According to the studies of Zhang,[100] this error can also be estimated within 1%. The correlation software employing the Gaussian sub-pixel interpolation has 0.1 pixel accuracy, which corresponds to a maximum uncertainty of 8% in measuring the velocity component. The uncertainty in flame normal varies from 4% for the case of a stable flame to 10% for the case close to blowout. The minimum radius of flame curvature that can be measured from PIV image is limited by resolution to 0.125mm. The maximum uncertainty in the evaluation of the flame stretch is found to vary from 30% for the case of a stable flame to 38% for the case close to blowout.

Very close to blowout, the bluff body flame does have some three dimensional features, as shown in Figure 50, during which the out-of-plane loss of image pairs diminishes the correlation signal peak strength. This can be compensated by thickening the light sheet or reducing the time delay between pulses. However, since the average flow and flame field was strongly two-dimensional, especially at the bluff body centerline, these uncertainties were not accounted for.

APPENDIX B

ACOUSTIC–OPTICAL DATA INTEGRATION

Work was done on improving robustness of detecting lean blowout by developing integration techniques that combine data from both acoustic and optical sensors. By relating information from multiple sensors, improved accuracy and more specific inferences could be made than that by the use of a single sensor alone. Towards this end, effort was made to develop probability density distributions of the number and duration of threshold crossings of precursor events or alarms. This is a continuation of the studies in the atmospheric swirl combustor discussed in Section 5.1. For example, Figure 65 plots the probability of detecting an optical alarm, conditional on detection of an acoustic alarm, P(O/A), versus magnitude of acoustic threshold level. The reference acoustic threshold level was selected to be 22σ (Figure 31). The probability of detecting both acoustic and optical based precursors increases to around 80% when the value of the acoustic signal is twice its reference threshold level. This plot indicates that the probability of detecting a simultaneous acoustic and optical alarm is greater when large acoustic precursors are present in the signal. This indicates that there are fewer false alarms detected during such large precursor events. However, there is a corresponding

decrease in the number of alarms detected as the thresholding level is increased, as shown in Figure 66 (right). Similar results were also obtained for large optical precursors. The occurrence of such acoustic and optical precursors increases in magnitude and duration as blowout is approached.

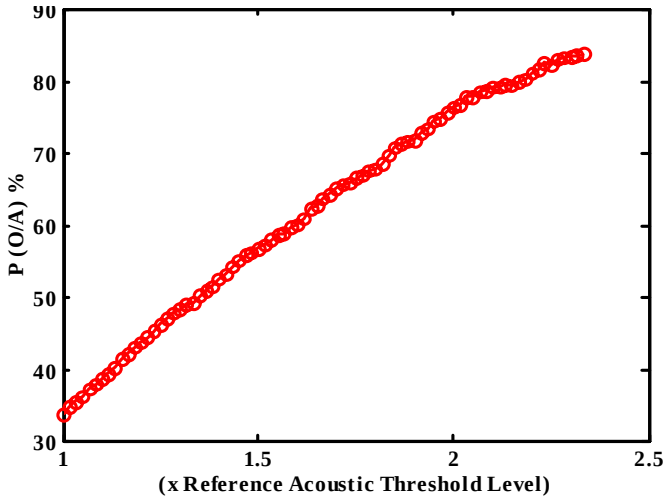

Figure 65: Conditional probability of detecting an optical alarm conditional on detecting an acoustic alarm upon thresholding level.

The combined alarm counter has advantages over the individual acoustic and optical sensor in lean blowout detection. To demonstrate this, random Gaussian noise was added to acoustic noise and then wavelet filtered at a frequency of 80 Hz. Figure 66 plots the wavelet-filtered acoustic signal and noise added signal, as well as the optical signal. Using the thresholding technique, the total number of alarms per second was computed and was plotted as a function of increasing acoustic threshold level. As expected, there were more false alarms detected for the noise-added acoustic data compared to the

original acoustic data. The optical alarms remain unchanged as only the acoustic threshold level is being varied in the x-axis.

Figure 67 plots the number of simultaneous acoustic and optical ("fused") alarms detected versus ϕ/ϕ_{LBO} for noise-added acoustic data. Also plotted are the "unfused" total acoustic alarms. Even though the number of alarms per second increases as blowout is approached, there is significant number of alarms at ϕ values where the flame is still stable. This shows the clear advantage of using an integrated acoustic–optical alarm counter, which does not detect any alarms until very close to blowout.

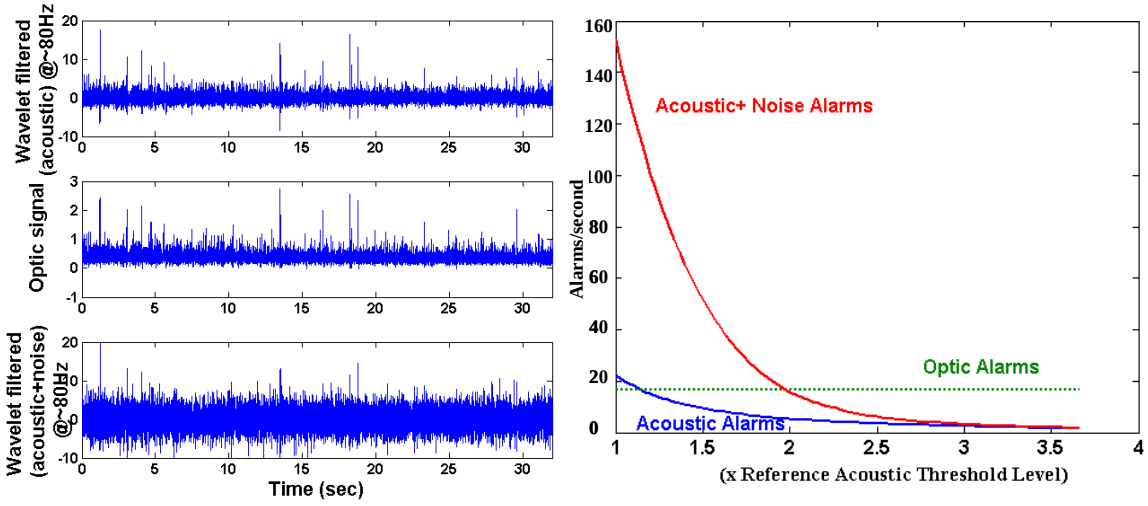

Figure 66: Time series (left) and dependence of total alarms per second (right) of wavelet filtered acoustic data at 80 Hz, optical data and wavelet filtered acoustic at 80 Hz +random Gaussian noise.

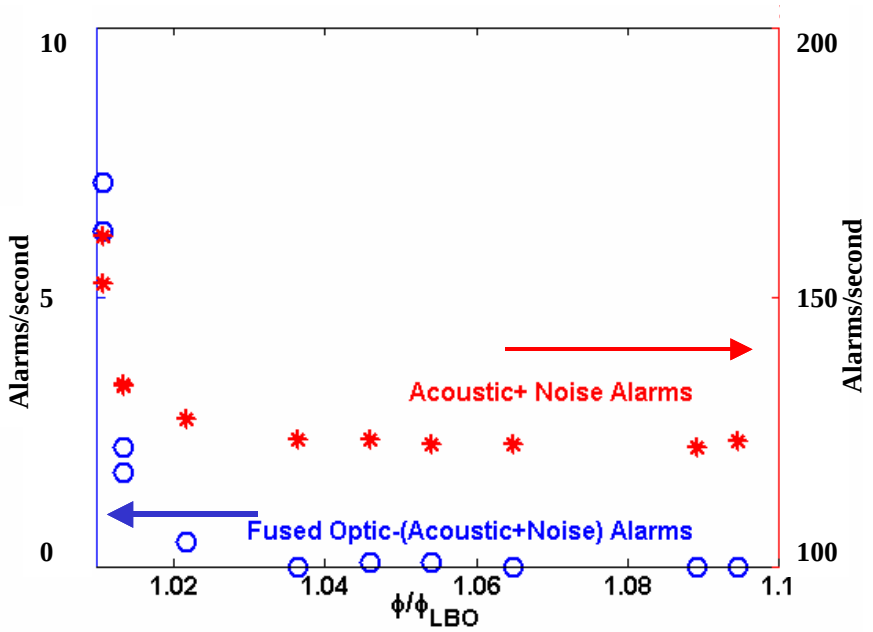

Figure 67: Dependence of acoustic alarms per second and fused acoustic-optical alarms per second versus ϕ/ϕ_{LBO}.

APPENDIX C

ADDITIONAL BLUFF BODY IMAGES

This section serves as an appendix to Chapter 6. Additional representative cases of flow vorticity plots (obtained from PIV) in conjunction with high-speed laser sheet images of the bluff body flame are presented here.

First, addenda of Figure 45 and Figure 46, with instantaneous vorticity plots of the bluff body flame at different equivalence ratios are shown below.

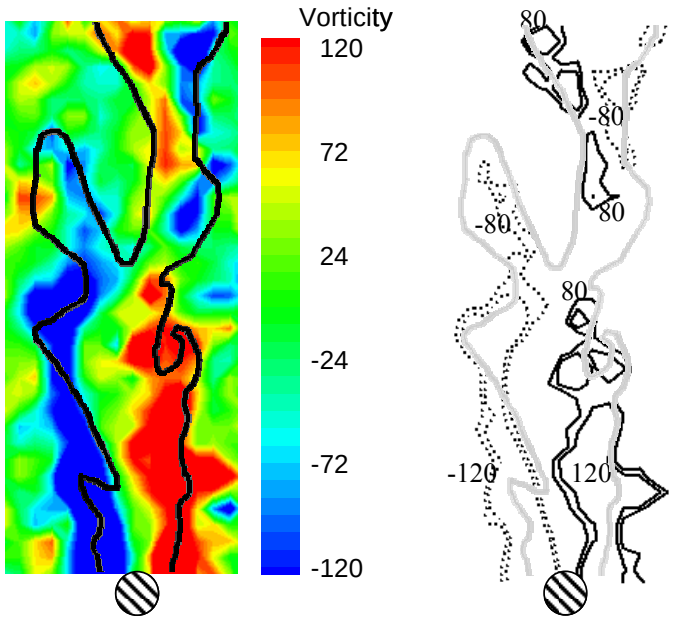

Figure 68: Instantaneous vorticity contour along with color map (left) and flame front edge at ϕ=0.63.

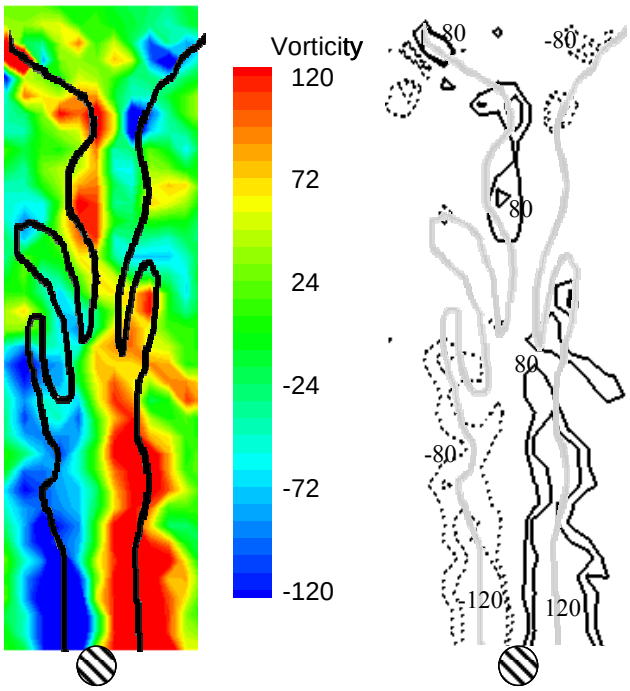

Figure 69: Instantaneous vorticity contour along with color map and flame front edge at ϕ=0.63.

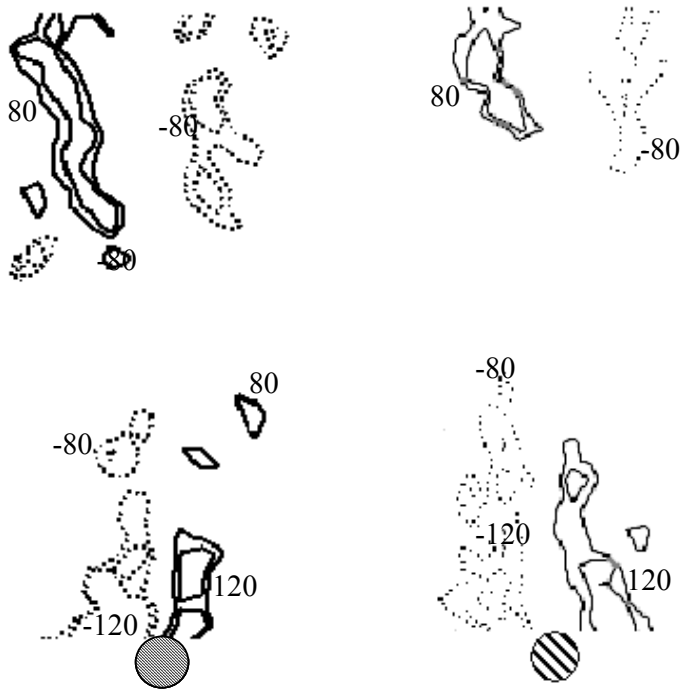

Figure 70: Instantaneous vorticity contours at 2 different instances at ϕ=0.7.

Figure 71: Instantaneous vorticity contours at 2 different instances at ϕ=0.72.

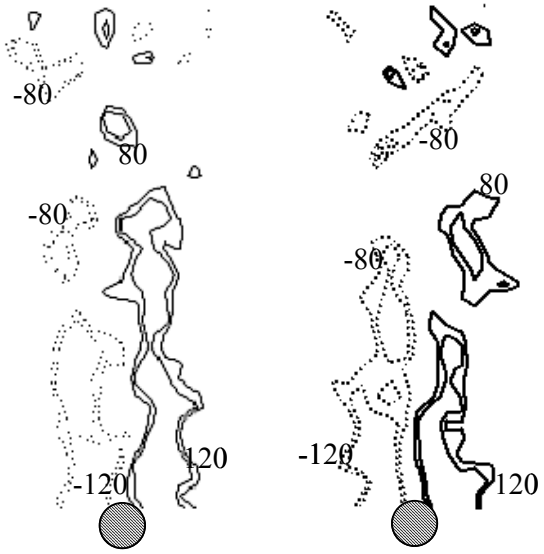

Figure 72: Instantaneous vorticity contours at 2 different instances at ϕ=0.6.

Next, addenda of Figure 52 and Figure 53, with sequences of bluff body flame images at different equivalence ratios are shown below.

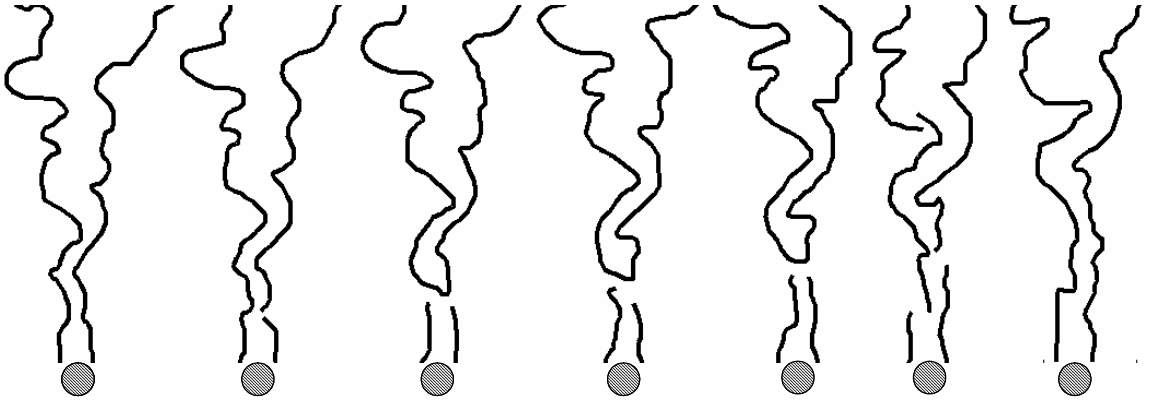

Figure 73: Sequence of flame images, 4 ms apart, taken during the first pre-blowoff stage at ϕ=0.63 (Flow direction is from bottom to top).

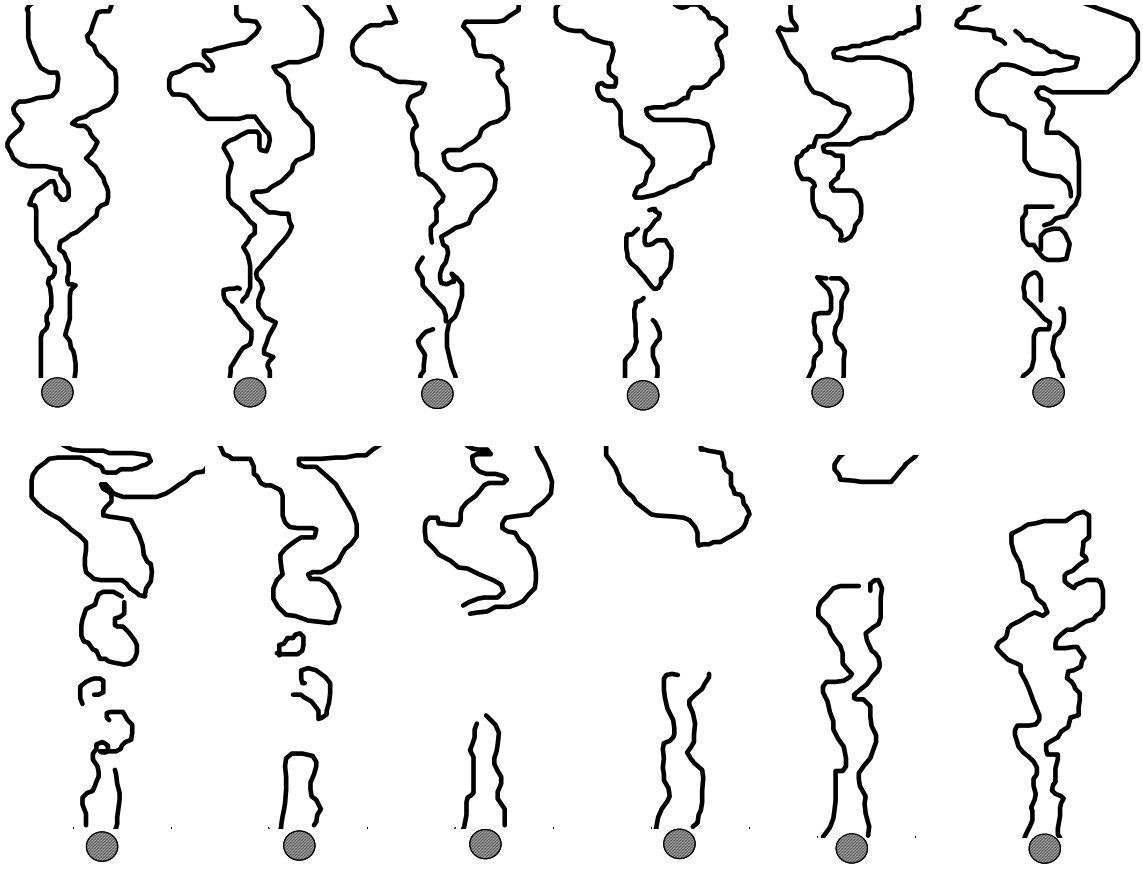

Figure 74: Sequence of flame images, 10 ms apart, taken during the second pre-blowoff stage at ϕ=0.6 (Flow direction is from bottom to top).

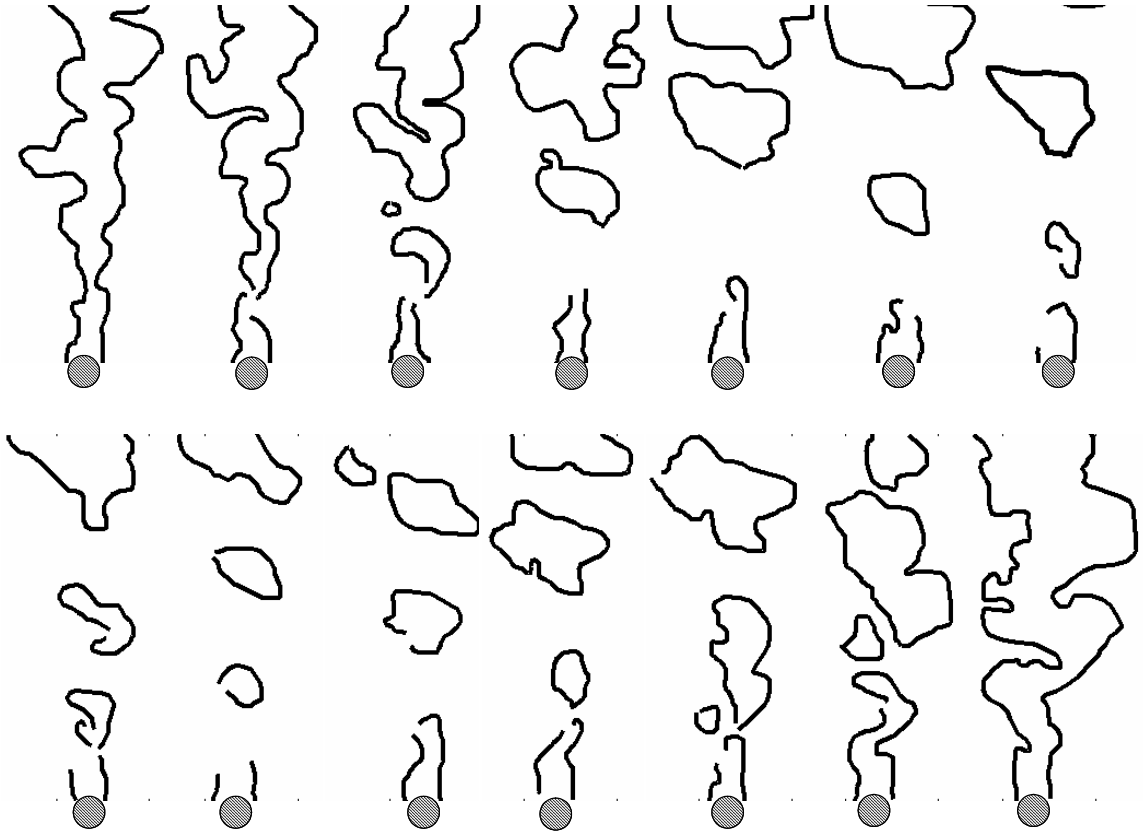

Figure 75: Sequence of flame images, 10 ms apart, taken during the second pre-blowoff stage at ϕ=0.6 (Flow direction is from bottom to top).

REFERENCES

[1] DuBell, T. L. and Cifone, A. J., "Combustor Influence on Fighter Engine Operability," *AGARD Meeting on Mechanisms of Combustion Instability in Liquid Fueled Combustors*, 1988.

[2] Cohen, J., Wake, B. E., and Choi, D., "Investigation of instabilities in a lean, premixed step combustor," *Journal of Propulsion and Power*, Vol. 19 (1), 2003, pp. 81-88.

[3] Rosfjord, T. J. and Cohen, J. M., "Evaluation of the Transient Operation of Advanced Gas Turbine Combustors," *Journal of Propulsion and Power*, Vol. 11 (3), 1995, pp. 497-504.

[4] Schefer, R. W., Wicksall, D. W., and Agrawal, A. K., "Combustion of Hydrogen-Enriched Methane in a Lean Premixed Swirl-Stabilized Burner," *Proc. Comb. Inst.*, Vol. 29, 2002, pp. 843-850.

[5] Shih, W. P., Lee, J., and Santavicca, D., "Stability and Emissions Characteristics of a Lean Premixed Gas Turbine Combustor," *Proc. Comb. Inst*., Vol. 26, 1996, pp. 2771-2778.

[6] Turns, S., *An Introduction to Combustion*, McGraw-Hill, New York, 2000.

[7] Correa, S. M., "A Review of NOx Formation under Gas-Turbine Combustion Conditions," *Combustion Science and Technology,* Vol. 87, 1993, pp. 329-362.

[8] Miller, J. A. and Bowman, C. T., "Mechanism and Modeling of Nitrogen Chemistry in Combustion," *Progress in Energy and Combustion Sciences*, Vol. 15, 1989, pp. 287-338.

[9] Zeldovich, J., "The Oxidation of Nitrogen in Combustion and Explosions," *Acta Physicochimica USSR*, Vol. 21 (4), 1946, pp. 577-628.

[10] Lewis, G. D., "Prediction of NOx Emissions," *ASME Paper 81-GT-119*, 1981.

[11] Hung, W. S. Y., "The Reduction of NOx Emissions from Industrial Gas Turbines," *The Eleventh International Congress on Combustion Engines*, Vol. 3, 1975, pp. 161-181.

[12] Hilt, M. B. and Waslo, J., "Evolution of NOx Abatement Techniques through Combustor Design for Heavy-Duty Gas Turbines," *Journal of Engineering for Gas Turbines and Power*, Vol. 106, 1984, pp. 825-832.

[13] Lefebvre, A. H., *Gas Turbine Combustion*, Taylor & Francis, Philadelphia, 1998.

[14] Glassman, I., *Combustion*, 3rd Edition, Academic Press, San Diego, 1996.

[15] Ducruix, S., Schuller, T., Durox, D., and Candel, S. M., "Combustion Dynamics and Instabilities: Elementary Coupling and Driving Mechanisms," *Journal of Propulsion and Power*, Vol. 19 (5), 2003, pp. 772-734.

[16] Straub, D. L. and Richards, G. A., "Effect of Fuel Nozzle Configuration on Premixed Combustion Dynamics," *ASME Paper 98-GT-492,* 1998.

[17] Sankaran, R. and Im, H. G., "Dynamic Flammability Limits of Methane-Air Premixed Flames with Mixture Composition Fluctuations," *Proc. Comb. Inst.*, Vol. 29, 2002, pp. 77-84.

[18] Barnes, J. C. and Mellor, A. M., "Effects of unmixedness in piloted-lean premixed gas turbine combustors," *Journal of Propulsion and Power*, Vol. 14, pp. 967-973.

[19] Wohl, K., Kapp, N. M., and Gazley, C., "Flame Stabilization and Quenching," *Proc. Comb. Inst.*, Vol. 3, 1951, pp. 3-21.

[20] Longwell, J. P., Chenevey, J., Clark, W., and Frost, E., "Flame Stabilization by Baffles in a High Velocity Gas Stream," *Proc. Comb. Inst*., Vol. 3, 1951, pp. 40-44.

[21] Williams, G., Hottel, H., and Scurlock, A., "Flame Stabilization and Propagation in High Velocity Gas Streams," *Proc. Comb. Inst*., Vol. 3, 1951, pp. 21-40.

[22] Jensen, W. P. and Shipman, C. W., "Stabilization of Flames in High Speed Flows By Pilot Flames," *Proc. Comb. Inst*., Vol. 7, 1958, pp. 674-680.

[23] Williams, G. C. and Shipman, C. W., "Some Properties of Rod Stabilized Flames of Homogeneous Gas Mixtures," *Proc. Comb. Inst*., Vol. 4, 1953, pp. 733-742.

[24] Cheng, S. I. and Kovitz, A. A., "Theory of Flame stabilization by a Bluff body," *Proc. Comb. Inst*., Vol. 7, 1958, pp. 681-691.

[25] Hertzberg, J. R., Shepherd, I. G., and Talbot, L., "Vortex Shedding Behind Rod Stabilized Flames," *Combustion and Flame*, Vol. 86, 1991, pp. 1-11.

[26] Ateshkadi, A., McDonnell, V. G., and Samuelson, G. S., "Lean Blowout for a Spray Fired Swirl Stabilized Combustor," *Proc. Comb. Inst*., Vol. 28, 2000, pp. 1281-1288.

[27] Feikema, D., Chen, R. H., and Driscoll, J. F., "Enhancement of flame blowout limits by the use of swirl," *Combustion and Flame*, Vol. 80, 1990, pp. 183-195.

[28] Syred, N. and Beer, J. M., "Combustion in Swirling Flows: A Review," *Combustion and Flame*, Vol. 23, 1974, pp. 143-201.

[29] Beer, J. M. and Chigier, N. A., *Combustion Aerodynamics*, Applied Science Publishers, London, 1972.

[30] Gupta, A. K., Lilley, D. G., and Syred, N., *Swirl Flows*, Abacus Press, Kent, USA, 1984.

[31] Schadow, K. C. and Gutmark, E., "Combustion instability related to vortex shedding in dump combustors and their passive control," *Progress in Energy and Combustion Sciences*, Vol. 8, 1992, pp. 117-132.

[32] Huellmantel L. W., Ziemer R. W., and Campbell A. B., "Stabilization of Premixed Propane-Air Flames in Recessed Ducts," *Journal of Jet Propulsion*, 1957, pp. 31-43.

[33] Hasan, M. A. Z., "The Flow Over a Backward Facing Step under Controlled Perturbation: Laminar Separation," *Journal of Fluid Mechanics*, Vol. 238, 1992, pp. 73-96.

[34] Mihalik, T. A., Lee, J. H. S., Continillo, G., and Di Mare, L., "Flammability Limits of Gaseous Mixtures in Porous Media," *17th ICDERS Meeting*, Heidelberg, Germany, 1999.

[35] Zukoski, E. E. and Marble, F. E., "The Role of Wake Transition in the Process of Flame Stabilization in the Bluff Bodies," *AGARD Combustion Researches and Reviews*, Butterworth Scientific Publishers, London, 1954, pp. 167-180.

[36] Nicholson, H. and Field, J., "Some Experimental Techniques for the Investigation of the Mechanism of Flame Stabilization in the Wake of Bluff Bodies," *Proc. Comb. Inst*., Vol. 3, 1951, pp. 44-68.

[37] Chao, Y. C., Chang, Y. L., Wu, C. Y., and Cheng, T. S., "An Experimental Investigation of the Blowout Process of a Jet Flame," *Proc. Comb. Inst*., Vol. 28, 2000, pp. 335-342.

[38] Peters N. and Williams F. A., "Lift-off Characteristics of Turbulent Jet Diffusion Flames," *AIAA Journal*, Vol.21 (3), 1983, pp. 423-429.

[39] Strahle, W., "On Combustion Generated Noise," *Journal of Fluid Mechanics*, Vol. 49 (2), 1971, pp. 399-414.

[40] Hurle, I. R., Price, R. B., Sugden, T. M., and Thomas, A., "Sound Emission from Open Turbulent Premixed Flames," *Proc. Roy. Soc. A*, Vol. 303, 1968, pp. 409-427.

[41] Katsuki, M., Mizutani, Y., Chikami, M., and Kittaka, T., "Sound emission from a turbulent flame," *Proc. Comb. Inst.*, Vol. 21, 1986, pp. 1543-1550.

[42] Kotake, S. and Takamoto, K., "Combustion Noise: Effects of the Velocity Turbulence of Unburned Mixture," *Journal of Sound and Vibration*, Vol. 139**,** 1990, pp. 9-20.

[43] Putnam, A. A., "Combustion Roar of Seven Industrial Burners," *J. Inst. Fuel*, Vol. 49, 1976, pp. 135-138.

[44] Petela, G. and Petela, R., "Diagnostic Possibilities on the Basis of Premixed Flame Noise Levels," *Combustion and Flame*, Vol. 52, 1983, pp. 137-147.

[45] Lewis, B. and von Elbe, G., *Combustion, flames and explosions of gases*, 3rd edition, New York, Academic Press, 1987.

[46] Ballal, D. R. and Lefebvre, A. J., "Weak Extinction Limits of Turbulent Flowing Mixtures," *ASME Journal of Engineering*, Vol. 101, 1979, pp. 343-348.

[47] Chung, S. H. and Lee, B. J., "On the Characteristics of Laminar Lifted Flames in a Non-premixed Jet," *Combustion and Flame*, Vol. 86, 1991, pp. 62-72.

[48] Pitts, W. M., "Assessment of theories for the behavior and blowout of lifted turbulent jet diffusion flame," *Proc. Comb. Inst.*, Vol. 22, 1988, pp. 809-816.

[49] Lee, B. J. and Chung, S. H., "Stabilization of Lifted Tribrachial Flames in a Laminar Non-premixed Jet," *Combustion and Flame*, Vol. 109, 1997, pp. 163–172.

[50] Vanquickenborne, L. and Van Tiggelen, A., "The stabilization mechanism of lifted diffusion flames," *Combustion and Flame*, Vol. 10, 1966, pp. 59-69.

[51] Kalghati, G. T., "Blowout Stability of Gaseous Jet Diffusion Flames. Part I: In Still Air," *Combustion and Flame*, Vol. 26, 1981, pp. 233-239.

[52] Ghosal, S. and Vervisch, L., "Stability Diagram for Lift-Off and Blowout of a Round Jet Laminar Diffusion Flame," *Combustion and Flame*, Vol. 123, 2001, pp. 646–655.

[53] Phillips, H., "Flame in a buoyant methane layer," *Proc. Comb. Inst.*, Vol. 10, 1965, pp. 1277-1287.

[54] Broadwell, J. E., Dahm, W. J. A., and Mungal, M. G., "Blowout of Turbulent Flames," *Proc. Comb. Inst.*, Vol. 20, 1984, pp. 303-310.

[55] Muniz L. and Mungal M. G., "Instantaneous Flame Stabilization Velocity in Lifted Jet Diffusion Flames," *Combustion and Flame*, Vol. 111, 1997, pp. 16-31.

[56] Kim, J. S., Williams, F. A., and Ronney, P. D., "Diffusional-thermal instability of diffusion flames," *Journal of Fluid Mechanics*, Vol. 327, 1996, pp. 273-301.

[57]Chen, T. H., Goss, L. P., Talley, D., and Mikolaitis, D., "Stabilization zone structure in jet diffusion flames from liftoff to blowout," *AIAA Paper 89-0153*, 1989.

[58] Knaus, D. A. and Gouldin, F. C., "Measurements of flamelet orientations in premixed flames with positive and negative Markstein numbers," *Proc. Comb. Inst.,* Vol. 28, 2000, pp. 367-373.

[59] Chakravarthy, V. K. and Menon, S., "Large Eddy Simulations of Confined Bluff Body Stabilized Highly Turbulent Premixed Flames," *FEDSM Paper 99-7798*, 1999.

[60] Rhee, C., Talbot, L., and Sethian, J., "Dynamic Behavior of Premixed Turbulent V-Flame," *J. Fluid Mech*., Vol. 300, 1995, pp. 87-115.

[61] Gouldin, F. and Cheng, R. K., "International Workshop on Premixed Turbulent Flames," *http://eetd.lbl.gov/aet/combustion/workshop/workshop.html*, accessed on January 16, 2006.

[62] Ravichandran, M. and Ganesan, V., "Isothermal Flow Field Modeling of Gas Turbine Afterburners," *Journal of The Institution of Engineers (India)*, Vol. 77, 1996, pp. 67-75.

[63] Williams, F. A., *Applied Mechanics Surveys*, Spartan Books, Washington D.C., 1966.

[64] Khitrin, L. N. and Goldenberg, S. A., "The Influence of Initial Temperature of a Combustible Mixture and of Ambient Pressure on the Stabilization Limits," *Proc. Comb. Inst.*, Vol. 6, 1955, pp. 448-451.

[65] Bovina, T. A., "Studies of Exchange between Re-circulation Zone behind the Flameholder and Outer Flow," *Proc. Comb. Inst.*, Vol. 7, 1958, pp. 692-696.

[66] Ahlborn, B., Lefrancois, M., and King, D., "The Clockwork of Vortex Shedding," *Physics Essays*, Vol. 11 (1), 1998, pp. 144-154.

[67] Sjunnesson, A., Henrikson, P., and Lofstrom, C., "CARS Measurements and Visualization of Reacting Flows in a Bluff Body Stabilized Flame," *AIAA Paper 92-650*, 1992.

[68] Soteriou, M. C. and Mehta, P. G., "Combustion Heat Release Effects on the Dynamics of Bluff Body Stabilized Premixed Reacting Flows," *AIAA Paper 2003-0835*, 2003.

[69] Coats, C. M., "Coherent Structure in Combustion," *Progress in Energy and Combustion Sciences*, Vol. 22 (5), 1996, pp. 427-509.

[70] Liendhard, J. H., *Synopsis of Lift, Drag, and Vortex Frequency Data for Rigid, Circular Cylinders*, Washington State University, Research Division Bulletin 300, 1966.

[71] Govardhan, R. N. and Ramesh, O. N., "A Stroll down Kármán Street," *Resonance Journal of Science Education*, Vol. 10 (8), 2005, pp. 25-37.

[72] Emmons, H. W., *High Speed Aerodynamics and Jet Propulsion*, Vol. 3, Princeton University Press, Princeton, 1958.

[73] Leonard, A. D., Smith, C. E., and van Erp, C., "Large eddy simulation of blowout of a bluff-body stabilized flame in a duct," *AIAA Paper 91-1862*, 1991.

[74] Tarabanis, K. and Bill, R. G., "Interaction of Turbulence and Premixed Combustion in the Recirculation Zone of Two-Dimensional Bluff Bodies," *Combustion Science and Technology*, Vol. 47, 1986, pp. 39-53.

[75]Roquemore, W. M., Reddy, V. K., Hedman, P. O., Post, M. E., Chen, T. H., Goss, L. P. Trump, D., Vilimpoc, V., and Sturgess, G. J., "Experimental and Theoretical studies in a Gas-fueled research combustor," *AIAA Paper 91-0639*, 1991.

[76] Venkataraman, K. K., Preston, L. H., Simons, D. W., Lee, B. J., Lee, J. G., and Santavicca, "Mechanism of combustion instability in a lean premixed dump combustor," *Journal of Propulsion and Power*, Vol.15 (6), 1999, pp. 909-918.

[77]De Zilwa, S. R. N., Uhm, J. H., and Whitelaw, J. H., "Combustion oscillations close to the lean flammability limit," *Combustion Science and Technology*, Vol. 160, 2000, pp. 231-258.

[78]Hedman, P. O., Fletcher, T. H., Graham, S. G., Timothy, G. W., Flores, D. V., and Haslam, J. K., "Observations of Flame Behavior in a Laboratory-Scale Premixed Natural Gas/Air Gas Turbine Combustor from PLIF measurements of OH," *ASME Paper GT-2002-30052*, 2002.

[79] Norton, D. G., "Combustion characteristics and flame stability at the microscale: A CFD study of premixed methane/air mixtures," *Chemical Engineering Science*, Vol. 58 (21), 2003, pp. 4871-4882.

[80] Chaos, M. and Chen, R., "An experimental study of pulsating instability in near-limit laminar non-premixed flames," *Combustion Science and Technology*, Vol. 176 (8), 2004, pp. 1191-1215.

[81] Gaydon, A. G. and Wolfhard, H. G., *Flames: Their Structure, Radiation, and Temperature,* 4th edition, Chapman and Hall, 1978.

[82] Keller, J. O. and Saito, K., "Measurements of the Combusting Flow in a Pulse Combustor," *Combustion Science and Technology*, Vol. 53, 1987, pp. 137-163.

[83] Lawn, C. J., "Distributions of Instantaneous Heat Release by the Cross-Correlation of Chemiluminescent Emissions," *Combustion and Flame*, Vol. 132, 2000, pp. 227-240.

[84] Roby, R. J., Hamer, A. J., Johnsson, E. L., Tilstra, S. A., and Burt, T. J., "Improved Method for Flame Detection in Combustion Turbines," *Transactions of the ASME*, Vol. 117, 1995, pp. 332-340.

[85] Mehta, G. K., Ramachandra, M. K., and Strahle, W. C., "Correlations between Light Emission, Acoustic Emission and Ion Density in Premixed Turbulent Flames," *Proc. Comb. Inst.*, Vol. 6, 1981, pp. 1051-1059.

[86] Khanna, V. K., Vandsburger, U., Saunders W. R., and Baumann, W. T., "Dynamic analysis of swirl stabilized turbulent gaseous flames," *ASME Paper GT-2002-30061*, 2002.

[87]Higgins, B., McQuay, M. Q., Lacas, F., Rolon, J. C., Darabiha, N., and Candel, S., "Systematic measurements of OH chemiluminescence for fuel-lean, high-pressure, premixed, laminar flames," *Fuel,* Vol. 80, 2001, pp. 67-74.

[88] Roby, R. J., Reaney, J. E., and Johnsson, E. L., "Detection of Temperature and Equivalence Ratio in Turbulent Premixed Flames Using Chemiluminescence," *Proceedings of the 1998 Int. Joint Power Generation Conference,* Vol. 1, 1998, pp. 593-602.

[89] Morrell, R., Seitzman, J., Wilensky, M., Lee, J., Lubarsky, E., and Zinn, B. T., "Interpretation of Optical Flame Emissions for Sensors in Liquid-Fueled Combustors," *AIAA Paper 2001-0787*, 2001.

[90] Raffel, M., Willert, C., and Kompenhans, J., *Particle Image Velocimetry: A Practical Guide*, Springer-Verlag, Berlin, 1998.

[91] Groechnig, K., *Foundations of Time-Frequency Analysis*, Birkhaeuser, Boston, 2000.

[92] Rajaram, R. and Lieuwen, T., "Parametric studies of Acoustic Radiation from Premixed Flames," *Combustion Science and Technology*, Vol. 75, 2003, pp. 2269-2298.

[93] Bradley, D., Gaskell, P. H., Gu, X. J., Lawes, M., and Scott M. J., "Premixed turbulent flame instability and NO formation in lean-burn swirl burner," *Combustion and Flame*, Vol.115, 1998, pp. 515-538.

[94] Rehm, J. E. and Clemens, N. T., "Relationship between vorticity/strain and reaction zone structure in turbulent non-premixed jet flames," *Proc. Comb. Inst*., Vol. 27, 1998, pp. 1113-1120.

[95] Poinsot, T. and Veynante, D., *Theoretical and Numerical Combustion*, R. T. Edwards, Flourtown, PA, 2001.

[96] Sung, C. J. and Law, C. K., "Extinction mechanisms of near-limit premixed flames and extended limits of flammability," *Proc. Comb. Inst.*, Vol. 26, 1996, pp. 865-873.

[97] Andrews, G. E. and Bradley, D., "Burning Velocity Of Methane-Air Mixtures," *Combustion and Flame,* Vol. 19, 1972, pp. 275-288.

[98] Boillot, A. and Prasad, A. K., "Optimization procedure for pulse separation in cross-correlation PIV," *Exp. Fluids*, Vol. 21**,** 1996, pp. 87-93.

[99] Westerweel, J., "Fundamentals of digital particle image velocimetry," *Measurement Science and Technology*, Vol. 8 (12), 1997, pp. 1379-1392.

[100] Zhang, J. S., *A fundamental study of two dimensional room ventilation flows under isothermal and non-isothermal conditions*, Ph.D. thesis, University of Illinois at Urbana-Champaign, 1991.